ELECTRICAL PROPERTIES OF NITROGEN
AND OXYGEN ION IMPLANTED SILICON

ELECTRICAL PROPERTIES OF NITROGEN
AND OXYGEN ION IMPLANTED SILICON

by

VINCE PETER TOVIZI, B. ENG.

A Project Report

Submitted in Partial Fulfillment

of the Requirements for the Degree

Master of Engineering

Department of Electrical Engineering
McMaster University
September, 1976

MASTER OF ENGINEERING   McMASTER UNIVERSITY
(Electrical Engineering)   Hamilton, Ontario

TITLE: Electrical Properties of Nitrogen
                and Oxygen Ion Implanted Silicon.

AUTHOR: Vince Peter Tovizi, B. Eng.
                (Technical University of Budapest)

SUPERVISOR: Dr. J. Shewchun

NUMBER OF PAGES: xvii , 179

ABSTRACT

The electrical properties of nitrogen and oxygen
ion implanted silicon samples have been investigated as
a function of various implantation and annealing conditions.

The temperature dependence of the electrical
characteristics of the implanted samples were analysed and
the results were compared with the ones obtained from
experiments performed on typical bulk silicon samples.
A unique computer controlled automatic system (J. Shewchun
et, al.) was used for the low temperature conductivity
and Hall effect measurements. Donor behaviour of the
implanted layers was observed in both the nitrogen and
oxygen implantation cases. It has been established that
very low conversion efficiency can be achieved in the
nitrogen and oxygen implants. Less than 1% of the
implanted ions became active after a high temperature
(825°C) anneal. The activation energies of donor like
impurities were determined by analysing the carrier
concentration versus reciprocal temperature graphs. It
has been concluded that the form of the above graphs
can only be described by a partially compensated

iii

semiconductor model which has more than one donor energy level. A model containing two monovalent kinds of donors with different energy levels and some assorted compensating acceptors was used to fit the carrier concentration vs. (1/T) curves. The activation energies of donor impurities were determined to be $E_{D1} = 0.016 \pm 0.001$ (eV), $E_{D2} = 0.034 \pm 0.003$ (eV) for the nitrogen implants and $E_{D1} = 0.021 \pm 0.001$ (eV), $E_{D2} = 0.037 \pm 0.001$ (eV) for the oxygen implanted silicon. We found the above ionization energies consistent and independent of the implantation and annealing conditions.

This study showed that the active impurity centers in the implanted layers could be well controlled by the implanted total dose, and were reproducible in the concentration range which is generally used in device fabrications.

ACKNOWLEDGEMENTS

TABLE OF CONTENTS

LIST OF FIGURES

ix

LIST OF TABLES

I

INTRODUCTION

I.1. Ion Implantation in Semiconductors

In recent years ion implantation has become a
widely used method of doping semicoductors because of its
considerable adventages over other doping techniques. The
ion implantation doping process involves the injection of
selected ions to a desired depth into the semiconductor
crystal.

This process is fundamentally different in several
respects from diffusion doping. Ion implantation is not a
process of thermal equilibrium; that is the motion of the
ion into the crystal is a result of its initial kinetic
energy, not a concentration gradient, as in diffusion.
Therefore, the usual solid solubility limits of dopant
atoms can be exceeded. Furthermore, the ions can be
injected into a relatively cold crystal; although subsequent
annealing is usually necessary to achieve a high percentage
of electrically active dopant atoms, the annealing tempera-
ture is usually below comparable diffusion temperatures.
This low temperature doping capability also means that low
melting temperature materials as well as very high diffu-
sion temperature materials can be doped in short times at
comparatively modest temperatures.

1

There are several other practical advantages offered by ion implantation such as the possibility of introducing any potential dopant into any semiconductor material, which in many cases could not be done by any other technique, better depth uniformity and control, better reproducibility and control of concentration because of the ability to measure accurately the quantity of ions introduced, the capability and flexibility of controlling the dopant profile by the variation of ion energy, and because ion implantation is a vacuum process it is less sensitive to surface contamination effects. However, there are some unfavourable side effects of the ion implantation process which can offset the advantages. Radiation damage of the implanted layer caused by the incident ions is the most important of these. Although a high temperature anneal following the implantation can substantially reduce the damage in the implanted layer, generally the free carrier mobility in the implanted layers is much less than in bulk semiconductor samples. It is also very difficult or impossible to achieve full electrical activity at low annealing temperature and to prevent channeling and its consequences completely.

In this project, the electrical behaviour of nitrogen and oxygen ion implanted silicon samples were investigated as a function of various implantation and anneal conditions.

1.2. The technique used to study the electrical properties
of ion implanted samples.

Hall effect and sheet resistivity measurements
over a wide temperature range is the commonly used method
to give information about the number of active impurity
centers in the implanted layer, the ionization energies of
the impurities, the temperature dependence of conductivity
and mobility, and the number of compensating impurities.

Rectangular shape Hall samples were used in these
experiments. The bulk silicon samples were cut by an ultra-
sonic dye from silicon wafers for the desired form. However,
the rectangular shape of the ion implanted Hall samples
were produced by opening a window in the approximately
1 micrometer thick silicon dioxide surface layer on the
silicon substrate.

The conductivity and Hall effect measurements as a
function of temperature were performed on an automatic
computer controlled system.

1.3. The Scope of this Report

The properties of bulk and ion implanted silicon
samples were investigated through the course of this pro-
ject and the results of the study are presented in this report.

The theoretical concepts behind the ion implantation

and the Hall effect experiments are described in Chapter
II. In Chapter III detailed descriptions of the apparatus,
the materials and the technological steps of sample pre-
paration used in this investigation are given. Chapter IV
is the summary of the experimental results and the methods
used to analyse them, while in the final chapter a compari-
son between the electrical behaviour of nitrogen and oxygen
ion implanted samples is presented.

THE THEORETICAL CONCEPTS OF ION IMPLANTATION AND HALL EFFECT MEASUREMENT

2.1. Introduction

This chapter contains the theoretical concepts of ion implantation for introducing impurities into semiconductors and the theory of conductivity and Hall effect measurements.

The first part of the chapter deals with the qualitative features of ion implantation.

In the second part, the equations of the Hall effect and conductivity measurements are derived. Also the list of the measured quantities and the methods used for measuring them on the automatic Hall effect system are presented. The program and the parameter definitions for the conductivity and Hall effect data are given in the Appendix.

2.2. Ion Implantation

In the process of ion implantation, atoms of the desired doping element are ionized and accelerated to high velocity and then caused to enter a substrate lattice by virtue of their kinetic energy. After the energetic ion comes to rest, the implanted atom can be in a position in which it serves to change the electrical properties of the substrate lattice, i.e. doping occurs. Crystal damage introduced by the implantation process will also effect the electrical behaviour of the implanted layer.

In order to characterize the ion implanted surface layer of a solid substrate the following major factors have to be determined: the energy-loss process controlling the range distribution of implanted atoms, the amount and nature of the lattice disorder created by the process, the location of the implanted atoms, the dopant profile, and the electrical characteristics that result from the implantation and subsequent annealing treatment. In the following sections of this chapter these factors will be discussed briefly.

2.2.1. Energy-Loss Processes

When a high energy ion beam strikes the surface of

a target material, the incident ions will gradually give up their initial energy by means of interactions with the substrate atoms, until they come to rest. The resulting energy-loss processes and the distribution of the implanted atoms could be determined from the interaction mechanism of the incident ions and the target atoms. The model used to treat these dynamic phenomena requires the definition of two types of interactions: electronic collisions and nuclear collisions. Electronic collisions occur when the moving ion excites or ejects atomic electrons. Nuclear collisions involve the stronger electrostatic force interaction between the nuclei of the incident and target atoms. In the nuclear collisions the energy of the incident ion is transmitted as translatory motion to a target atom as whole. Electronic collision involves smaller energy losses per collision, negligible deflection and negligible lattice damage. The nuclear collisions can involve large discrete energy losses, significant angular deflection of the trajectory and this process is responsible for producing displaced lattice atoms. The effects of these two collision phenomena are called electronic stopping and nuclear stopping.

The relative importance of the two energy-loss mechanism varies with the incident energy (E) and the atomic number (Z_1) of the incident ion. Electronic stopping

predominates for high energy low atomic number particles.

The theory, describing these two forms of energy-loss process of the introduced ions in solid amorphous targets was developed by Lindhard, Scharff and Shiott[33] and by Lindhard and Scharff[34]. This is known as the LSS theory, and assumes each of the above forms of energy-loss are independent and that the average rate of energy-loss of an ion as a function of distance may be expressed as a sum of the electronic and nuclear stopping in the following form:

$$- \frac{dE}{dx} = N \left[S_e(E) + S_n(E) \right] \qquad (2.1)$$

Where: E = the energy of the incident ion at the point x
along its path

N = the target density (atoms/unit volume)

$S_e(E)$ = the electronic stopping power

$S_n(E)$ = the nuclear stopping power

S_e is defined as the energy lost to electronic interactions when an ion with energy E traverses a thickness $\triangle x$ of a target of unit density.

S_n is defined as the energy lost to target atoms when an ion traverses a thickness $\triangle x$ of a target of unit density.

The average total range of an incident ion in an amorphous target is given by the integral of Equation (2.1).

$$R = \int_0^R \frac{dE}{dE/dx} = \frac{1}{N} \int_{E_o}^0 \frac{1}{S_e(E) + S_n(E)} \, dE \qquad (2.2)$$

Where E_o is the incident energy.

2.2.2. Range Distribution

The main parameters determining the distance that an ion travels are its energy (E), atomic number (Z_1) and mass (M_1); and the atomic number (Z_2) and mass (M_2) of the target. The definitions of the projected range (R_p) and the total range (R) of an ion are illustrated in Figure (2-1).

For single crystal substrates, the range distribution will depend on the factors mentioned above , and also on the temperature, dose rate, total dose and the orientation of the crystal respect to the incident beam. If a major crystallographic axis is aligned with the incident ion beam, the ions can travel much farther in the open channels of the crystal than otherwise. These particles have a much smaller rate of energy loss with distance and hence a much greater range than they would in an amorphous target.
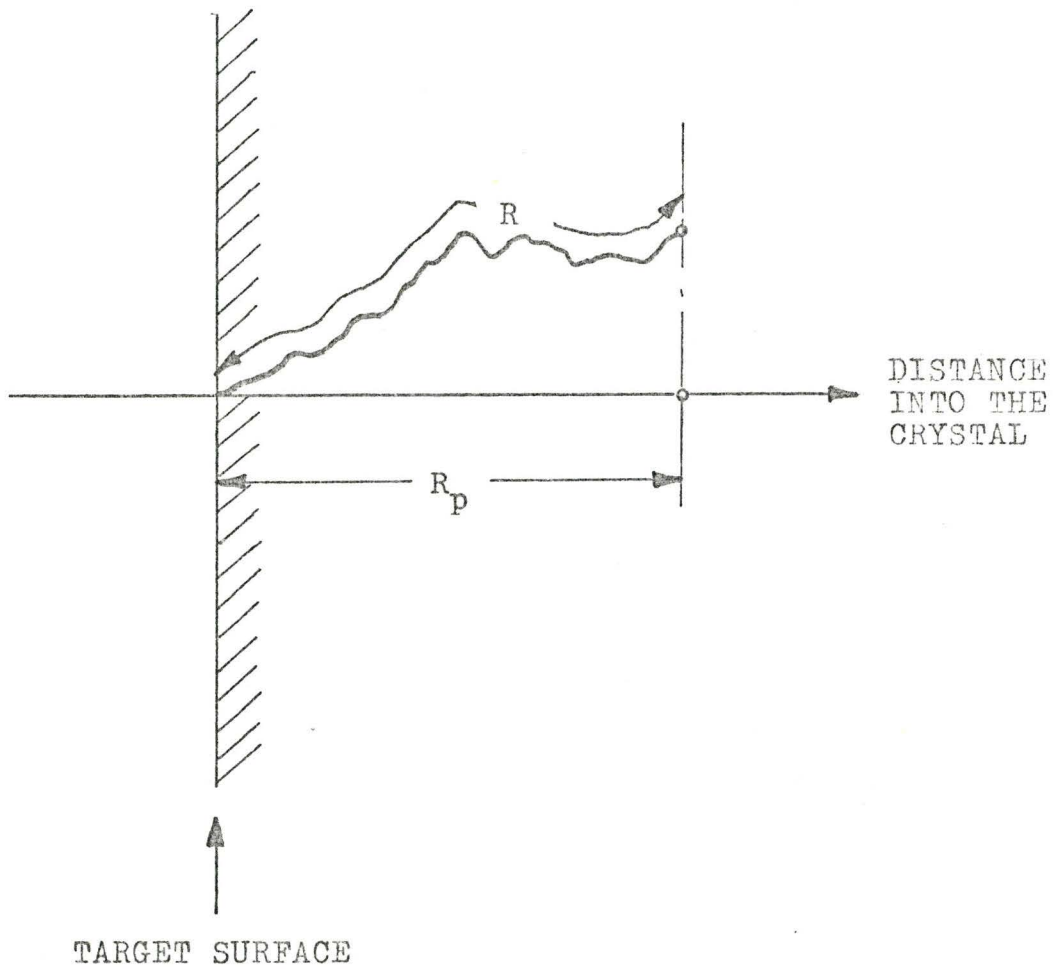
Figure (2 - 1). The definitions of the projected range
(R_p), and the total range (R).

The effect is called the channeling phenomenon.

In amorphous targets the distance travelled between collisions and the energy transferred per collision are both random variables; hence all ions of a given type and incident energy do not have the same range. In the absence of channeling, the range distribution is roughly Gaussian and can be characterized by a mean projected range (R_p) and a standard deviation σ as it is illustrated in Figure (2-6).

Several types of distribution profiles could be resulted from various implantation conditions as shown in Figure (2-2). When channeling is present the range distribution contains two distinct components. Region "A" illustrates the range distribution of the non-channeled fraction of the beam. This always involves at least 20% of the dopant atoms and it is characterized by essentially the same R_p and standard deviation as in an amorphous target. The more penetrating component (regions "B" and "C") is due to the channeled ions and in most cases it consists of a monotonically decreasing distribution which is terminated by a cut-off maximum value R_{max}. This maximum range (R_{max}) may be identified with those ions that remain channeled throughout their entire trajectory. The shape of the channeling peak (region "C") which is several times deeper than the amorphous peak except that
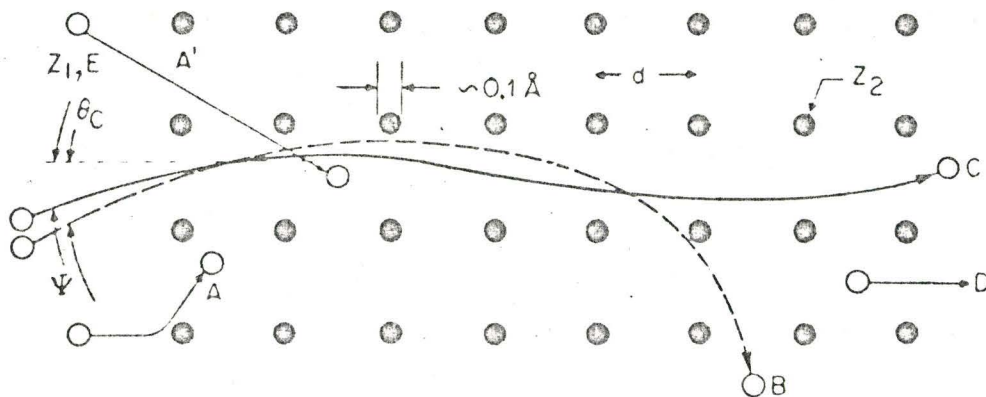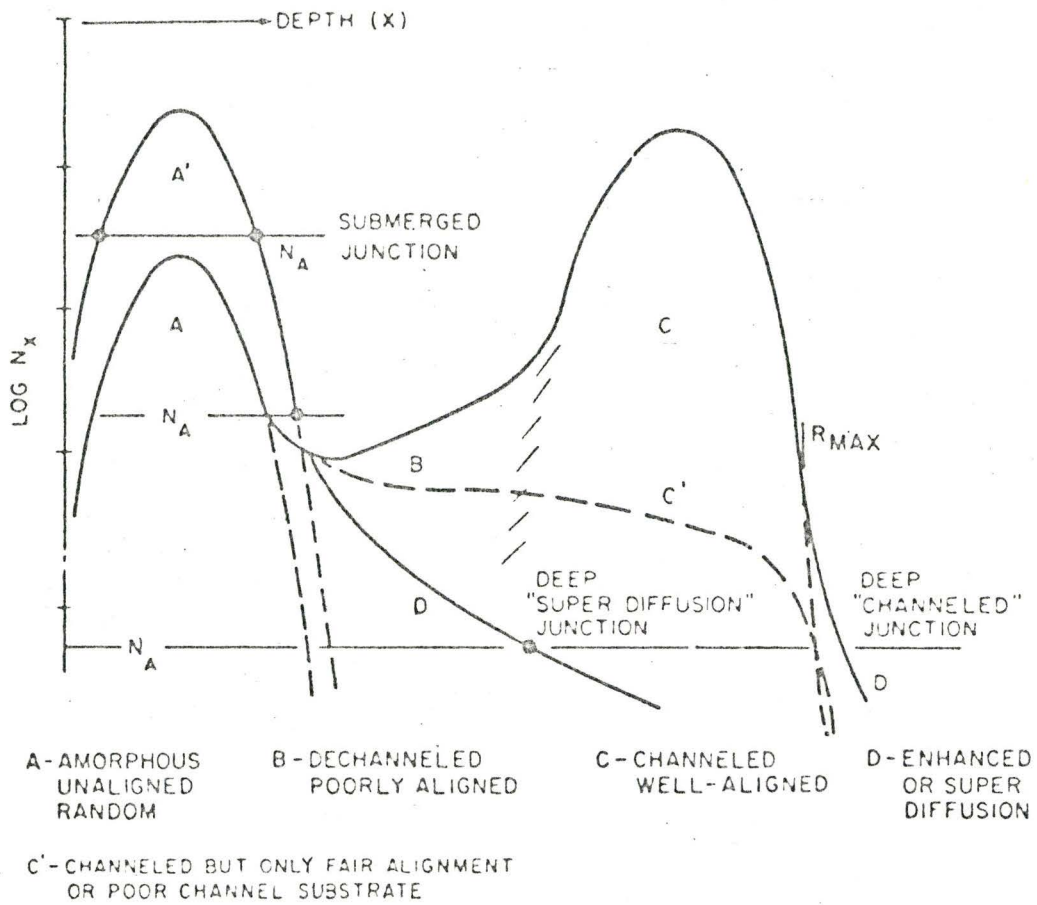
Figure (2-2) Top: Illustration of the several kinds of dopant
profile which can be created by implantation.
Bottom: Notation of the critical angle for channeling.

it falls more sharply on the high energy side.

The results of "non-channeled" ion implantations indicate that the range distributions are reproducible. In order to achieve reproducible range distributions channeling has to be prevented during implantation. Non-channeling conditions exist if the target is amorphous or the crystal is misaligned with the beam. Although there is no true random direction for most single crystal targets, implanting at an angle to the normal direction presents a a large density of randomly distributed lattice atoms to the cross section of the beam. The critical angle for misalignment of the crystal to prevent channeling is illustrated in Figure (2-2) and expressed by the following equation:

$$\Theta_c = c \, \psi_1 \qquad (2.3)$$

Where ψ_1 is the characteristic channeling angle ;

$$\psi_1 = \left(\frac{2 \, Z_1 \, Z_2 \, q^2}{E \, d} \right)^{1/2} \qquad (2.4)$$

where Z_1 is the atomic number of the target atoms; Z_2 , the atomic number of the dopant atoms; E, the energy of the incident ion; q, the electronic charge; and d, the lattice spacing parallel to the beam direction.

$$c = \left(\frac{a}{d}\right)^{1/2} \qquad (2.5)$$

Where "a" is the Thomas-Fermi screening distance which has a magnitude of 0.1-0.2 Å. It can be expressed as :

$$a = \frac{0.8853 \, a_0}{\left(z_1^{2/3} + z_2^{2/3}\right)^{1/2}} \qquad (2.6)$$

Where a_0 is the Bohr radius.

$$a_0 = 0.529 \times 10^{-8} \text{ cm} \qquad (2.7)$$

For energies less than a few hundred keV, θ_c is between 3° and 5° for standard dopants incident along either the $\langle 110 \rangle$ or the $\langle 111 \rangle$ axes.

An analytical approximation to both electronic and nuclear stopping processes has been suggested by Lindhard and Scharff[33] that allows the calculation of the implanted dopant distribution. The problem of ion penetration through an amorphous layer is treated analytically by Lindhard[35]. From his analysis, the total and projected ranges and the standard deviation for random incidence can be calculated. The results for several ion-substrate combinations are shown as a function of ion energy in Figure (2-3) and for most of the ions of interest in silicon in Figures (2-4) and (2-5).
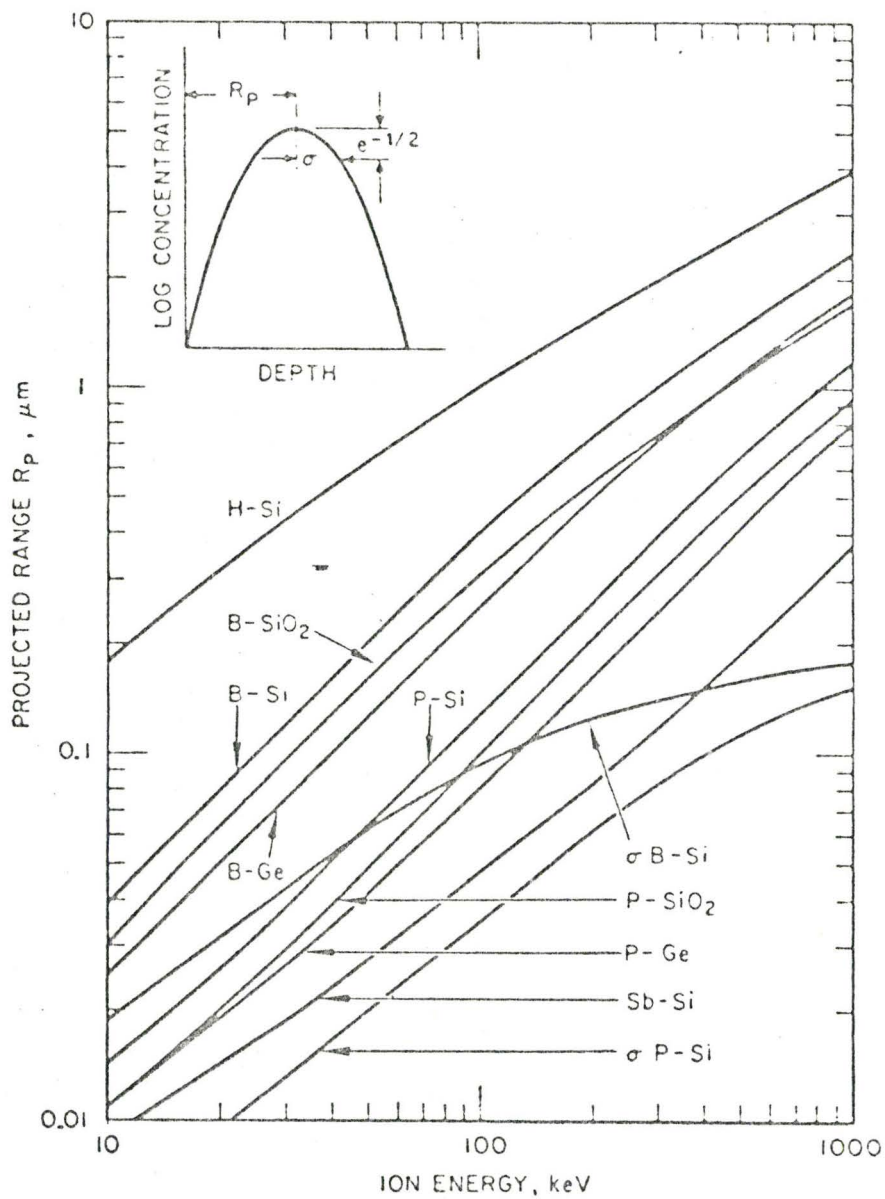
Figure (2-3) Projected range, calculated by the LSS model
of several ion - substrate combinations.[39]
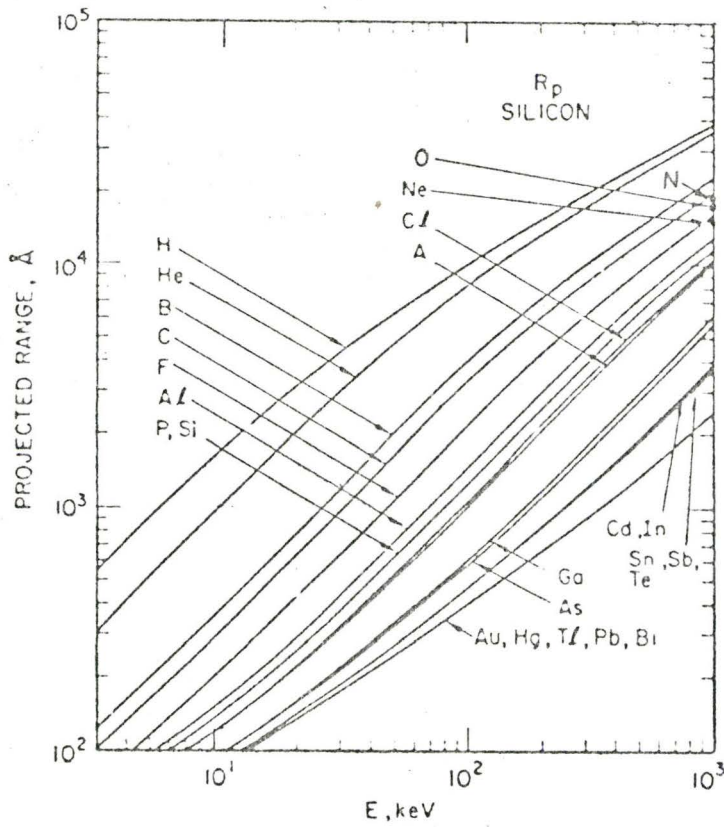
Figure (2-4) Calculated projected range (R_p) of ions in silicon. [39]
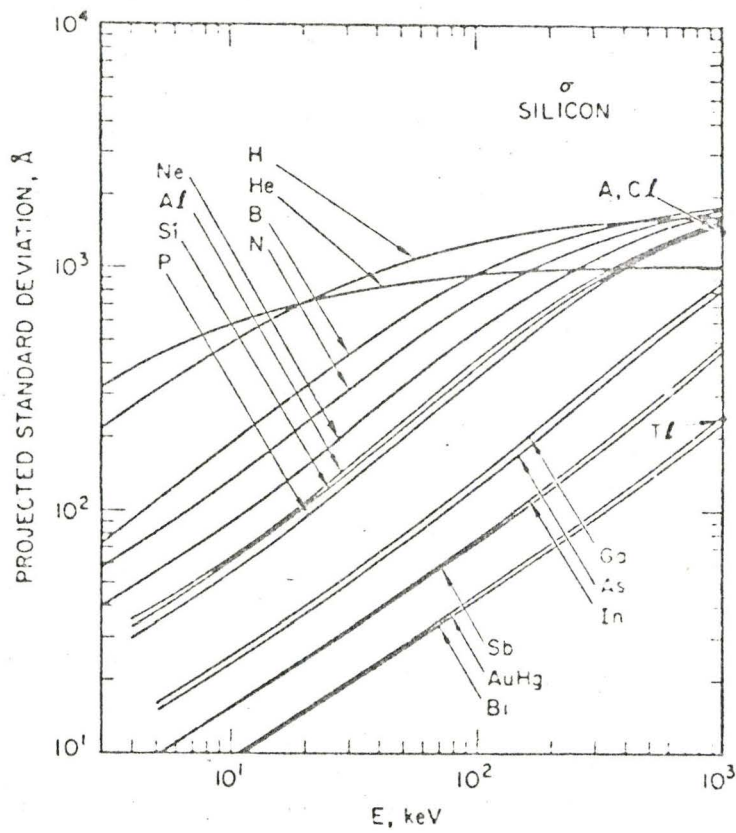
Figure (2-5)   Calculated standard deviation (σ')
of ions in silicon.[39]

2.2.3. Dopant Profile

It is very inportant in any semiconductor doping technique to achieve the desired dopant depth distribution. In the ion implantation process, there are three major effects which could significantly influence the dopant distribution. These are: the amorphous scattering, channeling and enhanced diffusion. Each effect yields in a different profile. The relative inportance of each of these effects must be controlled by the experimental technique to be able to achieve the desired dopant profile.

Just as it is difficult to achieve good channeling, it also requires care to limit channeling effects so that the profile will be determined only by amorphous scattering when desired. Channeling effects may be minimized, if not eliminated, by several techniques viz., (a) implanting through an oxide or metal layer that causes scattering of the beam, (b) misorienting the beam with respect to all major crystal axes or planes, and (c) predamaging the surface layer of the substrate crystal to be implanted to destroy the crystallinity (channels) there, e.g., with inert ions. The critical ion dose that is necessary to produce an amorphous layer increases rapidly with substrate temperature, or rather, a lower critical dose is sufficient to produce an amorphous layer at lower temperatures.

Assuming that one of these techniques is used to ensure that the implantation is effected thruogh an amorphous layer, then the LSS theory forms a useful approxi-

mation for predicting implantation depth. A wide variety of dopant distribution profiles can be designed by using the available simple expressions that relate the experimentally controlable values of implantation dose and energy to the resulting impurity concentration and depth. The depth to which the ions penetrate varies with several quantities, and can be determined from the LSS range-energy calculations. This analysis yields a Gaussian distribution. While not exact, especially far from the peak, this distribution is a useful approximation for design purposes. With reference to Figures (2-3) and (2-6), the maximum concentration can be related to the dose through a simple equation resulting from the Gaussian nature of the distribution.

$$\frac{dP_x}{dx} = \frac{1}{\sqrt{2\pi}\,\sigma} \exp\left[-\frac{1}{2}\left(\frac{\Delta x}{\sigma}\right)^2\right] \qquad (2.8)$$

$$n_{max} = \frac{D}{\sqrt{2\pi}\,\sigma} = \frac{0.399\,D}{\sigma} \qquad (2.9)$$

where P_x is the probability of finding an implanted particle at the location Δx away from the peak;

σ is the standard deviation;

x is the depth variable measured from the surface;

n is the volume concentration of implanted atoms;

n_{max} is the peak of the distribution; and

D is the number of ions implanted per unit surface area.
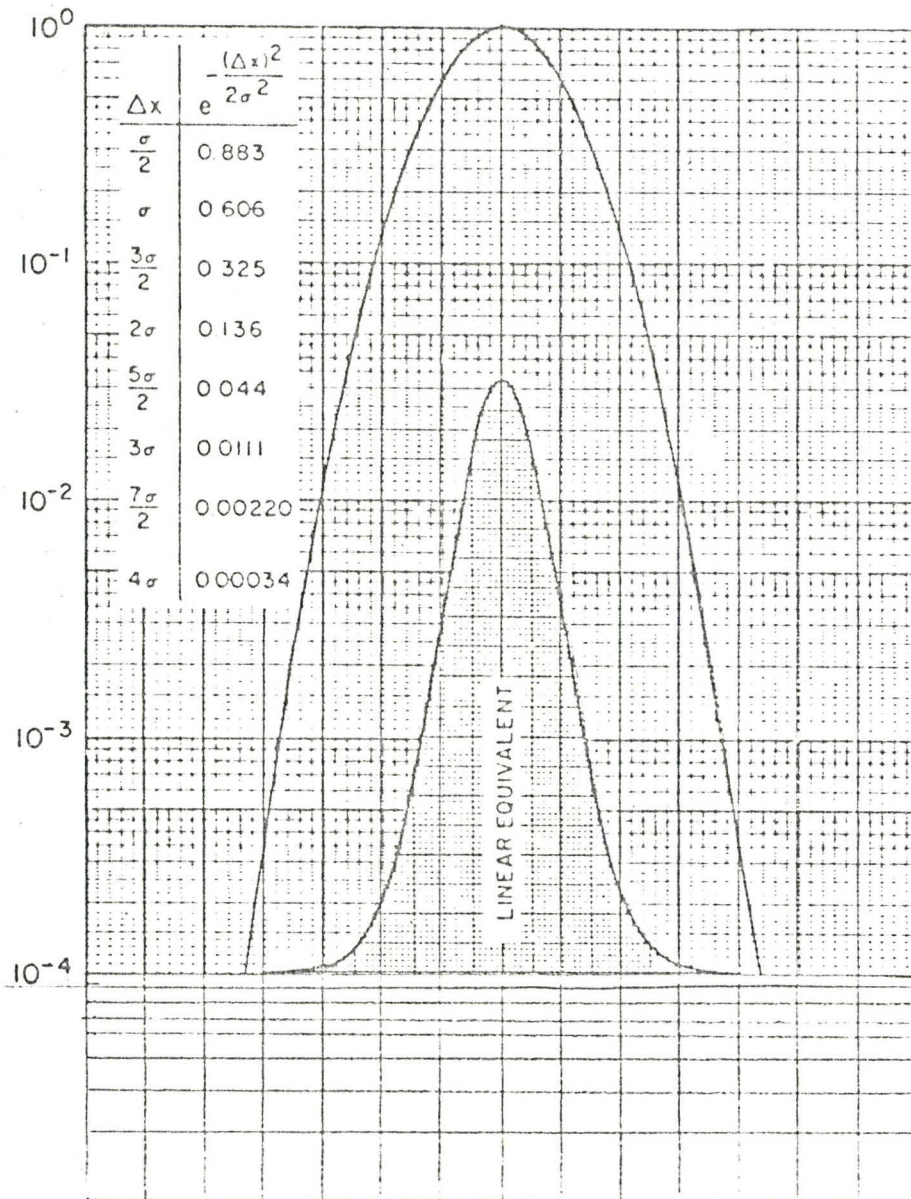
Figure (2-6)   Plot (to log and linear scales) of a
Gaussian distribution.

The term $1/\sqrt{2\pi}\sigma$ is a normalization factor to make $\int dP/dx = 1$.

An equation for the distribution of implanted atoms $n(x)$ as a function of depth below the surface can be written by using Eqs. (2.8) and the factors D, R_p, and σ.

$$n(x) = \frac{D}{\sqrt{2\pi}\sigma} \exp \left[- \frac{1}{2} \left(\frac{x - R_p}{\sigma} \right)^2 \right] \qquad (2.10)$$

The dopant profile can be made relatively flat out to the surface or constant with depth (x) by properly controlling the ion energy and dose. An approximation to a flat distribution can be achieved by judicious choice of a few fixed energies, the distributions of which can be added to determine the total distribution.

In the experiments of this study, the samples had $\langle 11\bar{1}\rangle$ crystal orientations and were misaligned about several degrees to the direction of the implantation axis to avoid channeling effects. 80 keV and 40 keV ion beams with dose ratio of 3 : 1 were used to develop flat, step-like distribution profile. The theoretical depth distributions obtained for the ion implanted samples are shown in Figures (4-6) and (4-7).

2.2.4. Lattice Disorder

When the incident ions slow down and come to rest in a crystal, they make a number of collisions with the lattice atoms. In these collisions, the ions transfer energy to both the electrons and the atoms of the crystal. The energy transferred from an ion to an atom could be sufficient enough for the displacement of the atom from its lattice site. The displaced atom can in turn displace other atoms and so on. This leads to a distribution of vacancies, interstitial atoms and other types of lattice disorder in the region around the ion track. At sufficiently high doses, the individual disordered regions may overlap forming an amorphous layer. The total amount of lattice disorder and its distribution in depth depend on the ion species, implantation temperature, energy, dose rate and total dose.

Although it is generally recognized that an ion implanted sample must be annealed to remove the damage associated with the process, very little is known about the fundamental processes involved in such an anneal. It has been shown in earlier studies that the anneal behaviour of the amorphous layer is significantly different from that of the isolated disordered regions around the track of each incident ion. The isolated disordered regions anneal at

considerably lower temperatures than the temperature
necessary for the epitaxial reordering of the amorphous
layer. If the implantations are made in substrates at
elevated temperatures, then the individual disordered
regions can anneal before the next ion strikes in their
vicinity, thus preventing the formation of amorphous
layers.

2.2.5. Electrical Characteristics of Implanted Layers

In order to determine the electrical properties of the
implanted layers, various electrical measurements can be
made. Current - voltage and capacitance - voltage measure-
ments are used generally to obtain information about the
junction characteristics. Hall effect and sheet resistivity
measurements are used to determine the number of electri-
cally active centers and carrier mobility. Layer removal
technique combined with the Hall effect and sheet resisti-
vity measurements is a useful method to obtain the depth
distribution of the dopant atoms.

The fact that the implanted layers are very thin
and the dopant concentration could be a strong function of
depth requires special techniques for reliable Hall effect
and sheet resistivity measurements. The measurement
technique requires that the implanted layer be isolated

from the substrate. This can be done by forming a junction
between the layer and substrate or using very high resis-
tivity substrate material. If a good junction exists, there
is no problem in making reliable measurements providing
that the sample is properly cleaned and surface currents
are low.

Low temperature Hall effect and conductivity measure-
ments were performed in this study to obtain information
about the ionization energies of the impurities and the
amount of compensating centers in the ion implanted layers.

In the following section the theoretical concepts
of the Hall effect and conductivity measurements are
discussed.

2.3. The Hall Effect and Conductivity Measurements

The Hall effect combined with conductivity mea-
surements is one of the most important tools for studying
the transport properties of semiconductor materials.

A rectangular semiconductor Hall bar is shown in
Figure (2-6), to illustrate the practical definitions of
the Hall effect and conductivity measurements. The bar,
which considered to be n-type in this example, has an

electric field strength E_x applied in the x direction, and a magnetic field of strength B_z applied in the z direction.

The elementary definition of electrical conductivity σ is the ratio of current density j_x to the electric field E_x in the direction of current flow.

$$\sigma = \frac{j_x}{E_x} \qquad (2.11)$$

The Hall coefficient R is defined by the following equation :

$$E_y = R \, B_z \, j_x \qquad (2.12)$$

where :

$$R = \frac{1}{q\,n} \qquad (2.13)$$

q = the electronic charge,

n = the free electron density, and

E_y = the electric field developed in the y direction.
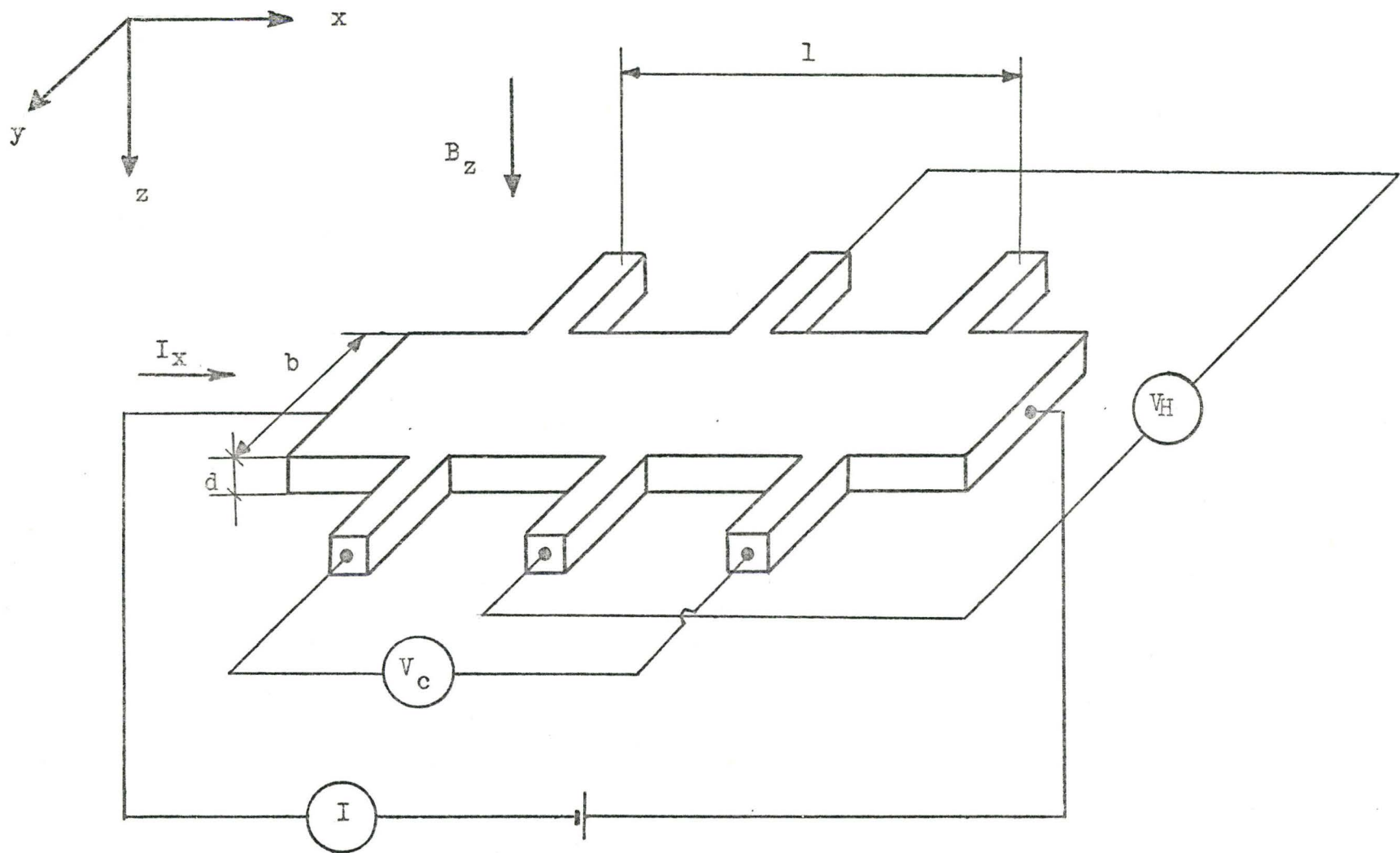
Figure (2-7) The practical definitions of the Hall effect
and conductivity measurements

The sign of R depends upon the sign of free
current carriers, i.e. electrons or holes. Both σ and R
are defined in terms of electric fields, magnetic fields,
and current densities. It is convenient to use rectangular
form specimen to determine σ and R from the measurements.

If a current I is passed through the sample in
in the direction of x , and the size of the sample is
determined by the width b and the thickness d , then
the conductivity can be determined by measuring the volt-
age drop V_c between two contacts a distance l apart.
Equation (2.11) will become :

$$\sigma = \frac{I\ l}{V_c\ b\ d} \tag{2.14}$$

If the voltage between the Hall probes is V_H ,
when a magnetic induction B is applied in the z direc-
tion, then Equation (2.12) becomes :

$$R = \frac{V_H\ d}{B\ I} \tag{2.15}$$

By substituing Equation (2.13) into Equation (2.15),
then the free carrier concentration in the sample can be

expressed in the following form :

$$n = \frac{B \ I}{q \ V_H \ d} \qquad\qquad (2.16)$$

The combination of the Hall effect with the con-
ductivity measurement yields the quantity of mobility.

$$\mu = |R| \, \sigma \qquad\qquad (2.17)$$

The measurements of the above quantities as a
function of temperature gives very important information
about the transport properties of semiconductor materials.

In this project a computer controlled automatic
system was used for measuring the conductivity and Hall
effect in semiconductor samples as a function of tempera-
ture. Fifty temperature points could be programmed in any
desired distribution over the 4.2 ^{o}K - 400 ^{o}K tempera-
ture range. A small process control computer is used to
run the temperature programmable liquid helium dewar, to
execute measurement and control functions, and to feed
the data to the data aquisition system.

The following data measurements were made at a
given temperature in one sequence block of measurements:

- temperature measurements (T), three times (one at the beginning of the sequence, one at the middle, and one at the end.) Two readings were actually made: one on a germanium resistance thermometer, the other one on a thermocouple.;

- conductivity voltage measurements (V_c), in both polarities of the current : $V_c(I^+)$ and $V_c(I^-)$. Averaging the two readings eliminates any thermo-electric effects which might be introduced.;

- sample current measurement (I) ;

- magnetic field measurement (B) ;

- Hall voltage measurements in the four possible combinations of sample current and magnetic field directions: $V_H (I^+, B^+)$, $V_H (I^-, B^+)$, $V_H (I^+, B^-)$, $V_H (I^-, B^-)$. Any error which could be due to any misalignment of the Hall contacts can be eliminated by using the average of the four readings.

The process control computer provided read commands to the DVM (digital voltmeter), so that the **twelve** data measurements were read and sent to the data acquisition subsystem. The data was stored on a roll of punched paper tape and on a hard copy output. The punched paper tape was converted to cards, with each sequence block of measurements being divided into two punched cards. At the

end of the experimental run, the data was processed by a
CDC 6400 computer with machine plotting of the data.

The program flow chart and parameter definitions
for the computer analysis of the Hall effect and conducti-
vity data are given in the Appendix.

III

APPARATUS, MATERIALS, AND SAMPLE PREPARATIONS

3.1. Introduction

The Implantation Equipment and the Automatic Hall Effect and Conductivity Measuring Equipment are described in detail in this chapter. The properties of the semiconductor material employed are also presented with emphasis on the technology for good sample preparation.

3.2. Implantation Equipment

A Texas Nuclear Corporation model 9509 Cocroft-Walton Accelerator was used for ion implantations. The maximum available accelerating voltage was 150 kV . A magnetic beam-switching system was added to the basic accelerator for mass separation. 150 keV ion-beams up to mass 22 could be produced, and the complete system was able to provide proton beams up to 400 microAmps at 150 keV . Figure (3-1) shows the functional block diagram of the ion accelerator. Three basic parts may be distinguished : 1) the ion source, 2) the mass separation section, and 3) the target chamber.

The ion source was a basic RF gas discharge tube
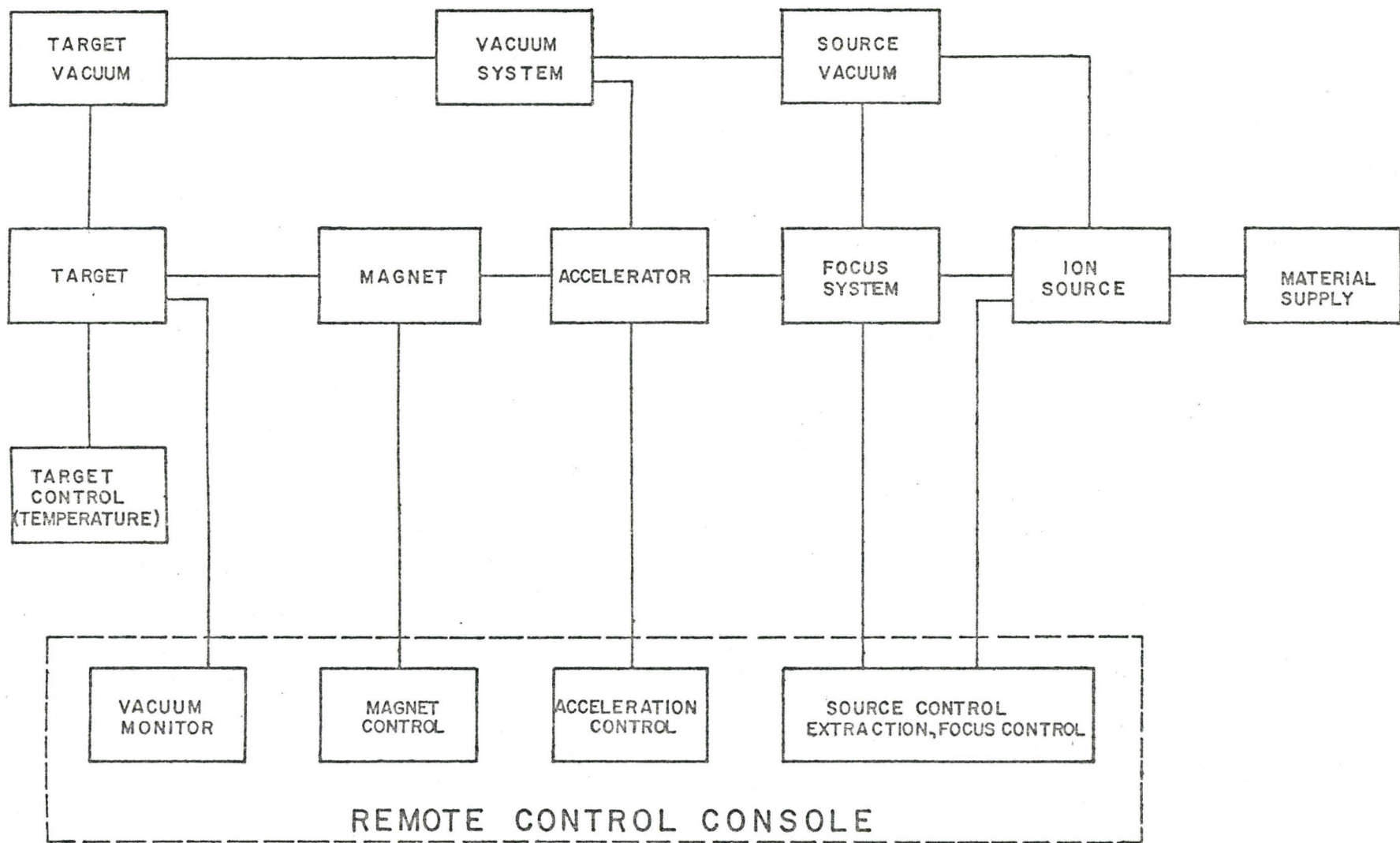
FIGURE (3—1) SCHEMATIC BLOCK DIAGRAM OF THE ION ACCELERATOR.

with the associated ion focusing and extracting systems.

The accelerator tube, whose purpose is to accelerate the ion beam without changing its focal properties was basically a vacuum section containing a series of electrodes such as beam deflection plates, electrostatic quadrapole focusing section and a beam detection section.

Different kinds of sample holder targets were available for implantations performed in various temperature ranges. The sample was mounted on a copper block target using Dow-Corning heat-sink compound. For low temperature implantations, the target chamber could be cooled down to approximately 30-50 ^{O}K, depending on the power dissipation of the target assembly, by a Malaker Corporation Mark VII-C Cryomite cryogenic cooler. The temperature of the sample was measured with a chromel-Au (0.02% Fe) thermocouple. The reference junction was immersed in a dewar of liquid nitrogen (77 ^{O}K). The detailed description of the target assembly is given by (Ref. 2). Another target assembly was used for high temperature implantations (up to 450 ^{O}K) . This target consisted of a sample holder block which could be heated by a heater attached to it, and the temperature was measured again with a gold-chromel thermocouple.

Two oil diffusion pumps with their associated cold traps and one mechanical pre-vacuum pump were connected to the vacuum system providing vacuum for the ion source, the target chamber and the accelerator tube.

Due to safety requirements, i.e. protection against high voltage, the Ion Implantation Equipment was powered, controlled and monitored from a remotely located control console.

Generally, 80 keV and 40 keV energy ion beams in a dose ratio of 3:1 were used to obtain relatively uniform step like layer profile. The beam currents varied from 5×10^{-9} Amps to 4×10^{-6} Amps depending on the implantation conditions. Doses ranged from 1×10^{14} ions/cm^2 to 1×10^{15} ions/cm^2 and were measured by means of a current integrator described in (Ref. 2). The beam was defocussed over an area of approximately 4.5-5.0 cm^2, resulting in an estimated reproducibility of 20% in the total dose. The substrate was tilted several degrees ($2.5^{\circ}- 4.5^{\circ}$) away from normal incidence in order to minimize possible channeling effects along a major axis.

3.3. Automatic Hall Effect Measuring System

A computer controlled automatic system (J. Shewchun et.al.) was used to measure conductivity and Hall effect as a function of temperature of the bulk silicon and the implanted silicon samples. The detailed description of the system was reported earlier by (Ref. 1). The outline of the operation of the equipment is given here.

The block schematic diagram of the apparatus is shown in Figure (3-2). The system includes a small process control computer to run a temperature programmable liquid helium dewar, a magnet, and a digital data acquisition system. Temperature controlled or temperature drift modes of operation could be selected in the temperature range of 4.2 ^{O}K to 400 ^{O}K with 50 programmable points in the temperature controlled mode.

The layout of the equipment may be divided into four major units :

- the dewar-magnet unit,
- the process control computer,
- the data acquisition unit,
- auxiliaries to provide vacuum for the dewar system, and auxiliaries of the helium gas return.

Dewar-Magnet Unit

The Dewar was obtained from the Andonian Associates. The cross-sectional diagram of the dewar is shown in Figure (3-4). It has two reservoirs, the inner one is for liquid helium and the outer one is for liquid nitrogen. Vacuum isolation can be provided between the two reservoirs, and the reservoirs and the dewar body outer shell, by pumping the vacuum isolation jacket. The capacity of the helium reservoir is three liters. The construction of the dewar
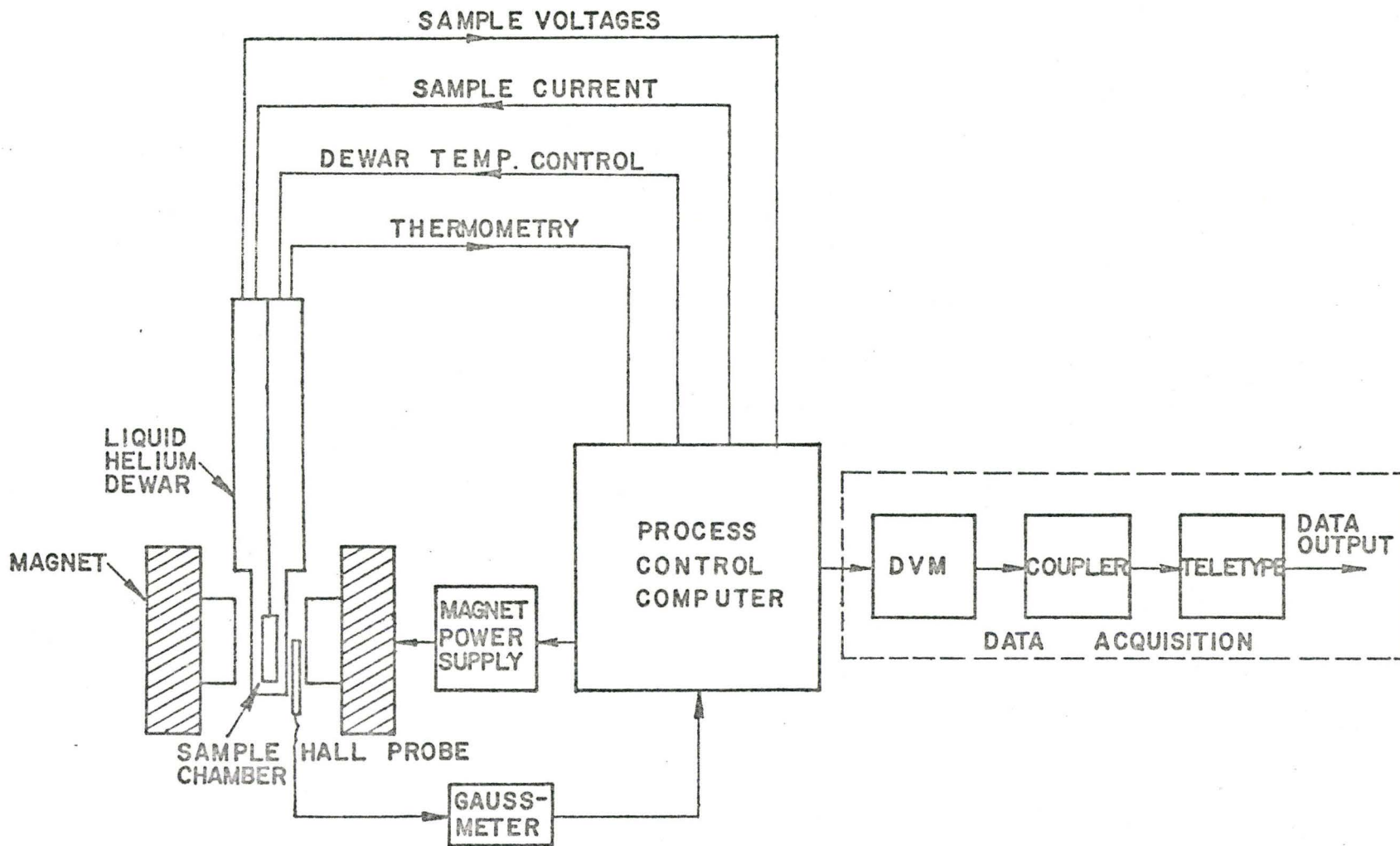
FIGURE (3-2) BLOCK SCHEMATIC DIAGRAM OF THE AUTOMATIC HALL EFFECT MEASURING SYSTEM.

is such that the sample compartment is sufficiently isolated
thermally from the helium well. Therefore, by applying
even a small amount of electric heat to the sample holder
copper block, rapid temperature change can be achieved
around the sample in the sample compartment. A small throttle
valve separates the bottom of the liquid helium from a capi-
lary tube which can conduct the liquid helium from the heli-
um well to the bottom of the sample compartment if the thrott-
le valve is open. A heat exchanger and a vaporization heater
are located at the bottom of the sample compartment. The
throttle valve can be controlled from outside the dewar via
a shaft. The amount of liquid flow in the capilary is cont-
rolled by the opening opening of the valve . Constant pres-
sure ($\sim 1/3$ atm.) was maintained on the liquid helium well
by a poppet relief valve at the top of the well. By ener-
gizing the vaporization heater (with power less than 1 W)
the liquid helium is converted into a cold gas which flows
upward in the sample compartment cooling the sample holder
and leaving the dewar at the top exhaust system. The tem-
perature of the sample holder is determined by the flow rate
of the gas and the amount of electric power applied to the
sample heater. The cold helium gas flows through a flow-
meter which indicates the amount of liquid helium to gas
conversion. The helium gas is finally conducted back to
to the main helium pipe system and can be liquified again
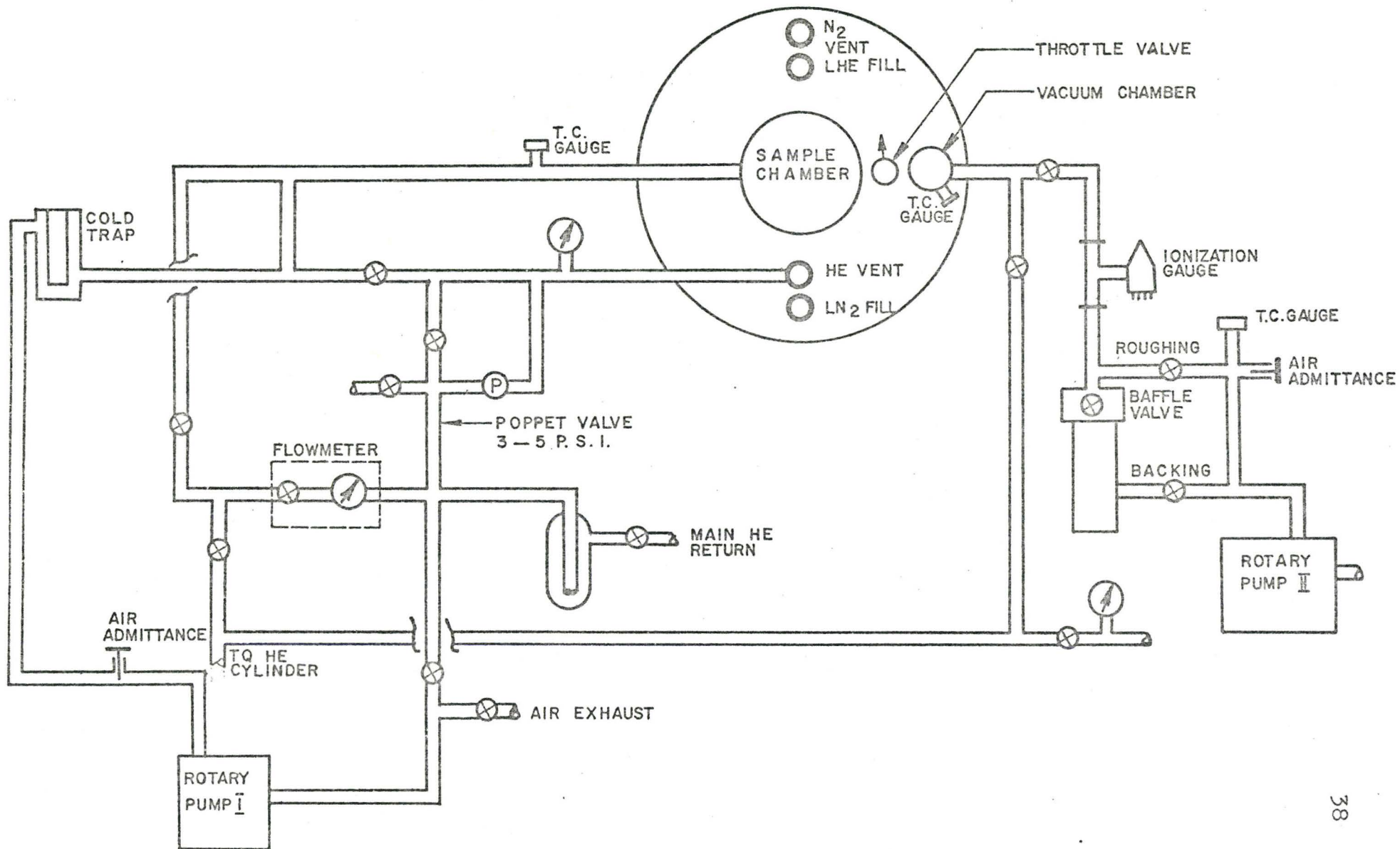
FIGURE (3-3) SCHEMATIC DIAGRAM OF THE VACUUM SYSTEM WITH THE DEWAR.

38

A ELECTRICAL FEEDTHROUGHS
B OFF—GAS PORT
C TOP WORKS
D HELIUM FILL AND VENT
E NITROGEN FILL
F NITROGEN VENT
G DEWAR BODY OUTER SHELL
H NITROGEN RESERVOIR
I HELIUM WELL
J VACUUM INSULATION
K NITROGEN—TEMPERATURE
  RADIATION SHIELD
L OUTER TAIL
M SAMPLE ZONE
N HEAT EXCHANGER
O VAPORIZATION HEATER
P CAPILLARY
Q THROTTLE VALVE
R THROTTLE—VALVE STEM
S THROTTLE—VALVE TOP WORKS
T THERMOCOUPLE FEEDTHROUGH
U THERMOCOUPLE
V SAMPLE HOLDER
W SAMPLE HEATER
X SAMPLE COMPARTMENT
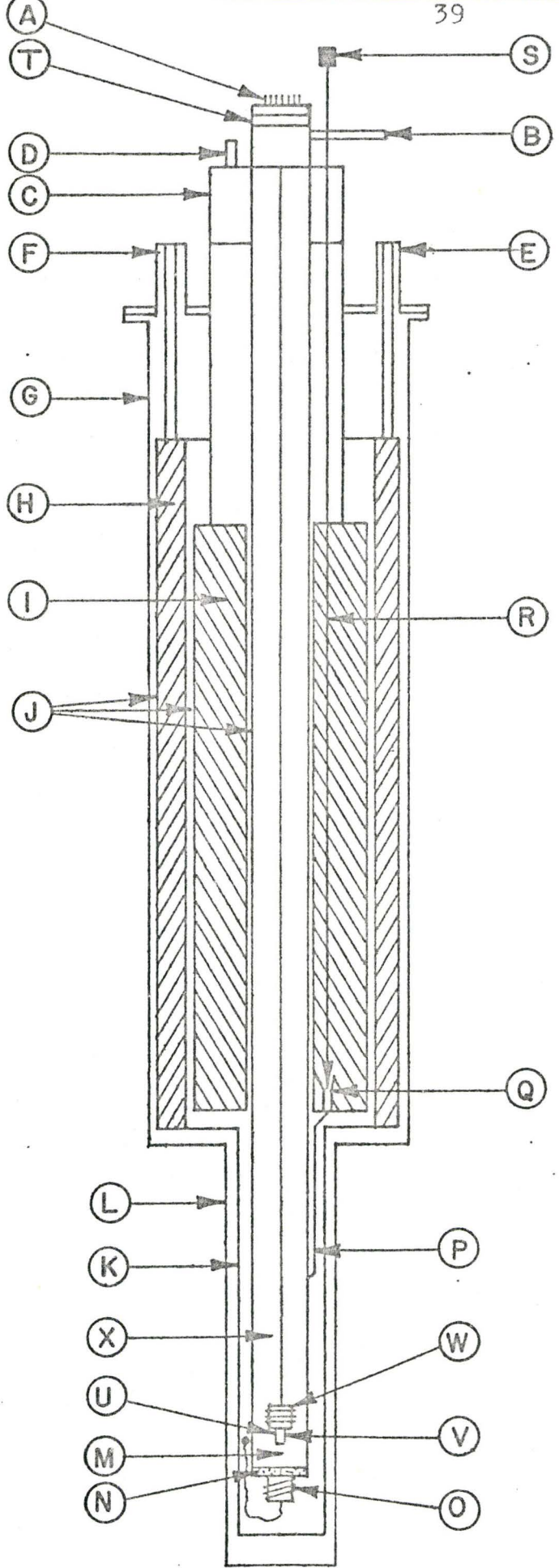
FIGURE (3—4) CROSS—SECTIONAL
DIAGRAM OF DEWAR.

39

with very little waste.

The starting temperature point of a given run can easily be set up by opening the throttle valve to a certain value and applying appropriate electric heat to the vaporization heater. The flowmeter monitors the flow rate of the helium gas and indicates the correct settings of the throttle valve and the vaporization heater power.

The sample holder is a copper block which is soldered to a hollow tube suspended from the top of the dewar. The sample holder is shown in Figure (3-5). The sample is mounted on the copper block, electrically insulated but thermally anchored to it by a thin sapphire sheet. To minimize second order effects and eliminate temperature gradient along the sample, a small amount of heat sink compound is applied between the sample and the sapphire sheet, and between the sapphire sheet and the sample holder. To avoid temperature fluctuations resulting from the helium gas turbulances a shield is provided around the sample. This shield is a cylindrical copper cup coated with teflon and surrounds the sample holder to provide a close environment for the sample. Teflon coated copper wires, 36 AWG were used to make the electrical connections to the sample holder, from the electrical feedthrough at the top of the dewar.

Temperature is adjusted from the starting temperature by applying electrical power to a second heater wound on the sample holder copper block. The electrical power was preprogrammed and supplied on command of the PCC. Less than 1% tem-

SAPPHIRE SHEET

HOLLOW TUBE

HEATED COPPER BLOCK

COPPER PIN

INSULATION

SAMPLE HOLDER COPPER BLOCK
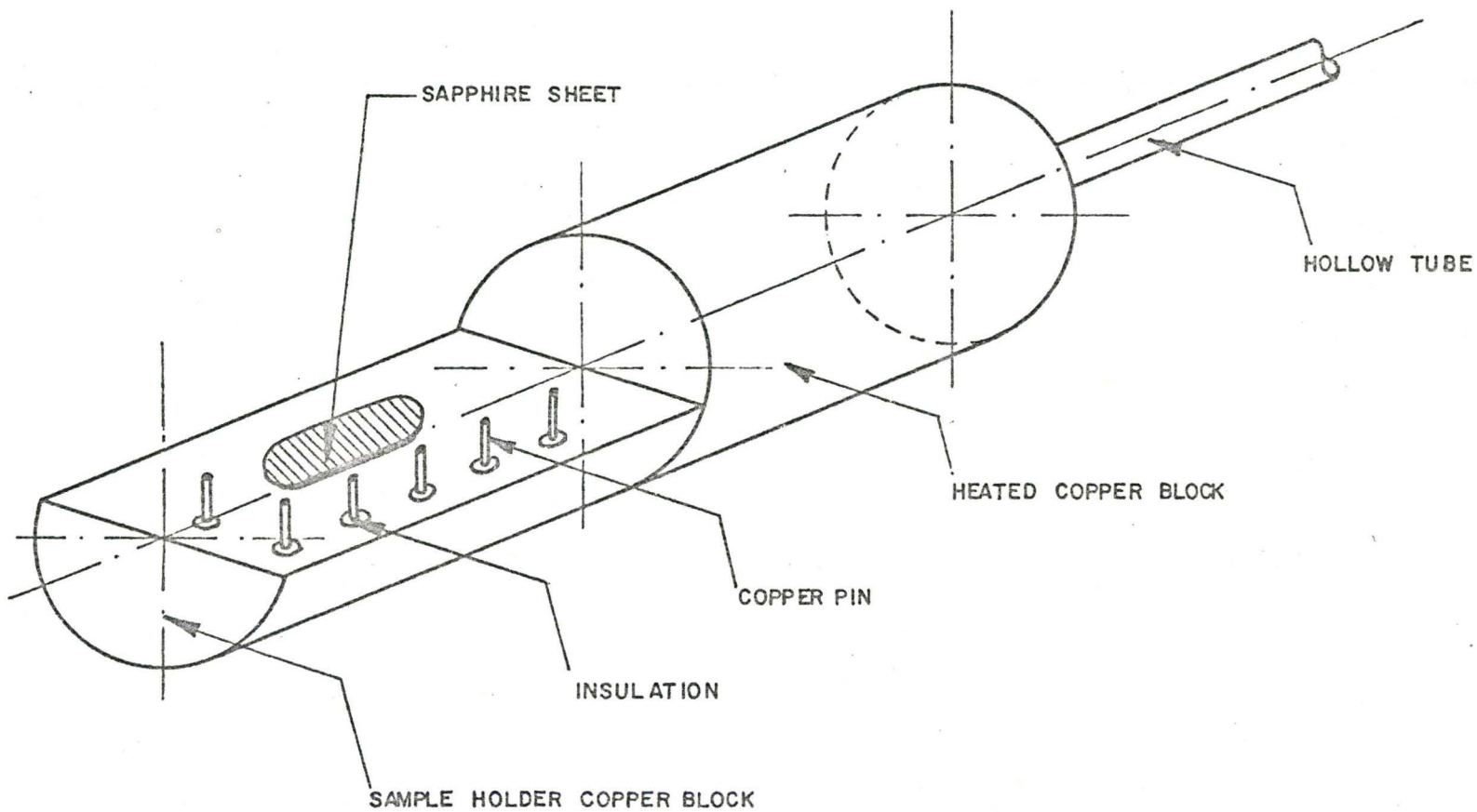
FIGURE (3 – 5) SCHEMATIC DIAGRAM OF THE SAMPLE HOLDER

41

perature change was maintained over the time period
required to excecute a block sequence (approx. 2.5 min.)
of measurements and control functions in the temperature
control mode. Linear distribution of reciprocal tempera-
ture steps (1/T) is programmed in the PCC using resistors
in a plug in card.

A gold (0.02% Fe) — Chromel thermocouple junction
mounted on the copper block in the vicinity of the sample
was used for temperature measurements. The reference
thermocouple junction was immersed in liquid nitrogen (77 ^{o}K).
In the very low temperature range, between 4.7 ^{o}K and 15 ^{o}K
the output of a germanium resistor thermometer mounted on
the sample holder block was checked against the readings of
the thermocouple for more accurate temperature measurements.

The magnetic field was supplied by a magnet obtained
from the Magnion Incorporated. The specifications of the
magnet are :

- maximum field intensity up to 14 kGauss
- field homogenity : 1 part in 10^{5}

The PCC controlled the magnet power supply to
execute : "turn on and off", and "reverse field" commands
at the appropriate time of the sequence block. A calibra-
ted Hall probe with a Bell Gaussmeter performed the magne-
tic field measurements in every block of sequence, and the

data was sent to the data acquisition unit.

Process Control Computer (PCC)

Manual, semiautomatic, and automatic features can be selected both in the temperature control and the temperature drift modes of operation by switches and timers placed on the front of the PCC. The following functions are executed by the PCC :

- sample temperature adjustment,
- sample current adjustment ,
- control of time sequence,
- control of time interval between sequence blocks,
- magnet control,
- execution of measurements : (B, I, V_c, V_H) and direction of the data to the data acquisition,
- monitoring for system malfunction and operator blunder.

Data Acquisition

For the read commands of the PCC a Digital Voltmeter measured the appropriate function in the sequence block. An interface coupled the signals to the Teletype which had paper tape and hard copy output.

The instrumentation of data acquisition is commer-
cially available Hewlett-Packard design, with the follow-
ing specifications :

DVM : integrating type

resolution : 1 μV

input impedance : 10^{12} ohms

Teletype : ASR 33 model

Coupler : universal type can drive magnetic

tape recording or punched card units

beside Teletype.

One sequence block of measurements consisted of
12 measurements, as follows :

- Germanium thermometer reading;
- three thermocouple readings, one at the be-
  ginning, one at the middle and one at the
  end of the sequence;
- current measurement;
- measurements of conductivity voltages with
  both +I and -I current directions;
- four Hall voltage measurements ,
  corresponding to the four possible

configurations of magnetic field

and current directions ;

- magnetic field intensity.

The punched paper tape was converted into punched cards. Two cards were required to store the information of one sequence block of measurements. A CDC6400 computer was used for the computer analysis of the data.

Auxiliaries

Two mechanical pumps and one oil diffusion pump with cold trap were used to produce the required vacuum in the isolation well of the dewar. Figure (3-3) shows the auxiliary system including the vacuum system with the pumps, the vacuum measuring devices, the gasflowmeter, poppet relief valve and other auxiliry devices.

3.4. Materials and Sample Preparations

3.4.1. Materials

Two kinds of samples were prepared for the low temperature Hall effect measurements :

- bulk silicon samples for calibration purposes ;

(Both p- and n-type silicon samples were obtained.)

- samples prepared for ion implantation.

3.4.2. Bulk Silicon Hall Sample Preparation

Phosphorus doped n-type and boron doped p-type
Czochralski grown Syton polished silicon wafers were ob-
tained from the Monsanto Company. The n-type silicon had
0.1 ohm·cm resistivity while the p-type silicon had 2 ohm·cm
resistivity. The crystal orientations of both types were
$\langle 111 \rangle$. The samples were ultrasonically cut to the size
and shape shown in Figure (3-6). After cutting, the samples
were chemically cleaned in quartz bakers in the following
manner:

1) Rinsed in deionized water

2) Boiled in the solvent of $2 H_2SO_4 + 1 H_2O_2$ at
   $60\ ^oC - 70\ ^oC$ for 10 minutes.

3) Rinsed in deionized water

4) Boiled in $5 H_2O + 1 HCl$ solvent at $60\ ^oC - 70\ ^oC$
   temperature for 10 minutes.

5) Rinsed in deionized water

6) Rinsed in dilute HF, $20 H_2O + 1 HF$ in a teflon
   beaker for 10 minutes.

7) Rinsed in deionized water

8) Blown dry with clean helium gas

In order to make electrical connections to the sample
metal pads are needed on the two ends and on each small arm
of the Hall bar. Therefore, the dried samples were placed
in a vacuum system and aluminium pads were deposited on them.

Sonoweld ultrasonic welding equipment was used to weld the approximately 0.001 inch diameter aluminium wires to each aluminium contact pad. The sample was then mounted on the sample holder copper block of the Hall effect measuring equipment.

A piece of sapphire sheet was placed on the copper block and fixed to it by means of some Dow-Corning heat sink compound. The sapphire ensured the required electrical isolation between the metal block and the silicon sample while maintaining effective heat conduction between them. The sample was positioned on the sapphire by using a small amount of heat sink compound underneath. The welded aluminium wires of the sample were connected to the copper pin electrodes of the sample holder and were bonded by means of silver paint solvent. Using proper procedure, good ohmic electrical connections could be made to the semiconductor samples. The quality of the connections was checked on a curve tracer. The voltage-current characteristic of ohmic electrical connections should be a straight line going through the origin and extending over the entire range of voltages and currents to which the contacts could be subjected during the Hall effect experiments. Generally, it means a current range between 10^{-8} Amps and 10^{-1} Amps. It was vitally important to produce low resistance ohmic contacts to the samples in order to maintain high accuracy in the conductivity and Hall effect measurements even at very low temperatures.
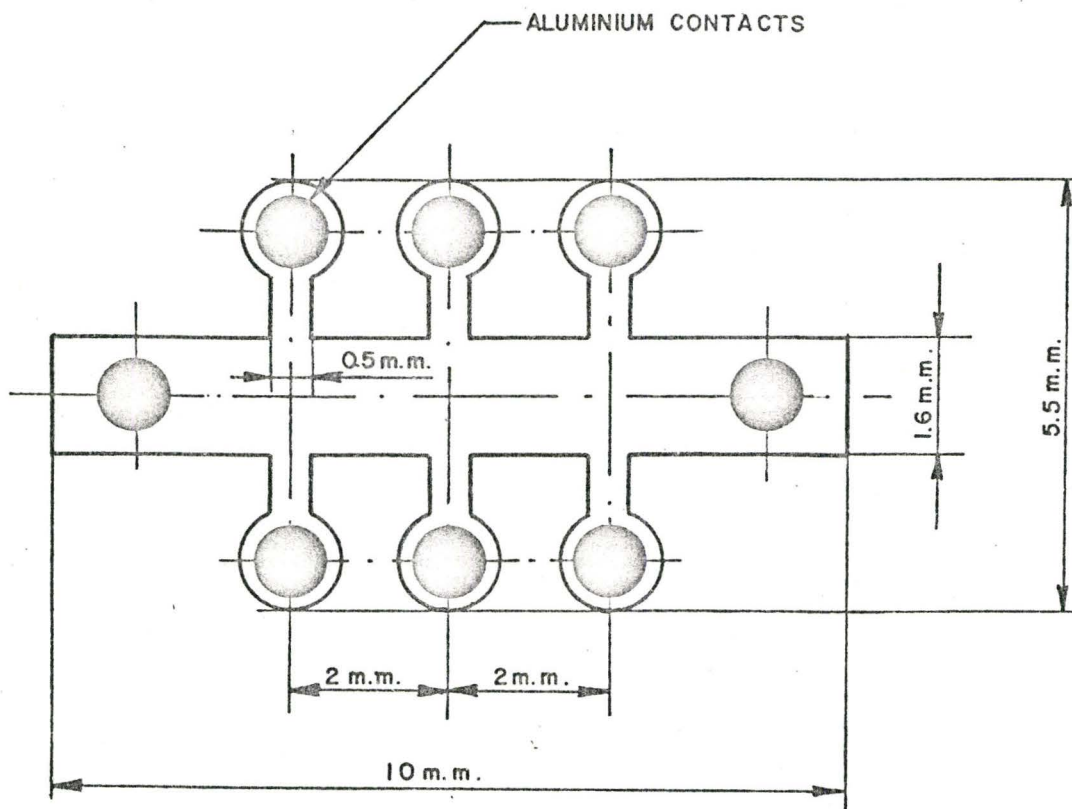
FIGURE (3—6) TYPICAL BULK SILICON HALL SAMPLE CUT BY
AN ULTRASONIC DIE.

3.4.3. Hall Sample Preparation for Ion Implantation

The silicon substrate used in these experiments were in high quality, high resistivity, boron doped, polished on one side. They were obtained from the Monsanto Company.

The resistivity of the substrate determines the minimum number of carriers which could be measured in the implanted layer by means of the Hall effect measurement. The application of high resistivity substrate materials is necessary to maintain good electrical isolation between the ion implanted layer and the substrate. If the net concentration of the active centers in the ion implanted layer is much higher than it is in the substrate, then the depletion region at the junction could be assumed to be extended entirely into the p-type substrate. Thus, the effective thickness of the implanted layer does not change considerably. It has been found that substrate resistance 10 ohm·cm or higher generally is adequate to measure 10^{11} carriers/cm^2 (3).

In our experiments p-type, boron doped silicon substrates were used. The resistivities of the substrates were between 7.66-13.33 ohm·cm . The crystal orientation of the material was $\langle 111 \rangle$. The silicon wafer was a disk 1 inch in diameter and 0.01 inch thick. The surface of the substrate had to be very clean and free from any damage.

The following technological steps were used for the

production of rectangular shape ion implanted Hall samples
in this study:

1) Etching and cleaning

2) Growing oxide on the surface

3) Photolithography to open windows in the oxide
   prior to diffusion

4) Diffusion

5) Photolithography to open a rectangular window
   in the oxide for implantation

6) Ion implantation

7) High temperature anneal

8) Vacuum deposition of aluminium contacts

9) Ultrasonic welding for wiring the sample

10) Mounting the sample into the automatic Hall
    effect measuring equipment

Etching and Cleaning

Each sample was etched in concentrated HF acid held
in a teflon beaker for about 30 seconds. The samples were
removed from the HF acid by means of teflon tweezers, rinsed
in methanol and dipped into chloroform or boiling methanol.
Then they were blown dry with clean helium gas.

Oxide Growing

The process was carried out in a quartz diffusion
tube of a Lyndberg furnace. The temperature of the slice

was maintained at 1100 ^{o}C and steam was applied for the oxide formation. An approximately 1.0-1.5 μm thick silicon dioxide layer was grown on the surface of the silicon during a 5-6 hour period of oxidation.

Photolithographic Technique

Photolithographic technique and diffusion were used to develop rectangular shape "Hall sample" pattern with diffused contacts.

Photolithography is the method for cutting windows in silicon dioxide surface layers. Figure (3-7) shows the flow chart for the steps encountered in the window formation process prior to diffusion. The schematic diagram of the masks used in the process are shown in Figure (3-8). The following steps were applied:

A. Coating

This process consisted of laying a film of photo-resist material on the surface of the oxide. Such a film should be thin, highly adherent, uniform and completely free from dust and pinholes. In the coating process, the silicon slices were placed on a spinner and a thin layer of photo-resist film was obtained on the surface of the slice by spinning it with a drop of photoresist emulsion on it. The spinning range extended from 1000 rpm to 5000 rpm and re-sulted in films about 0.5 μm thick.
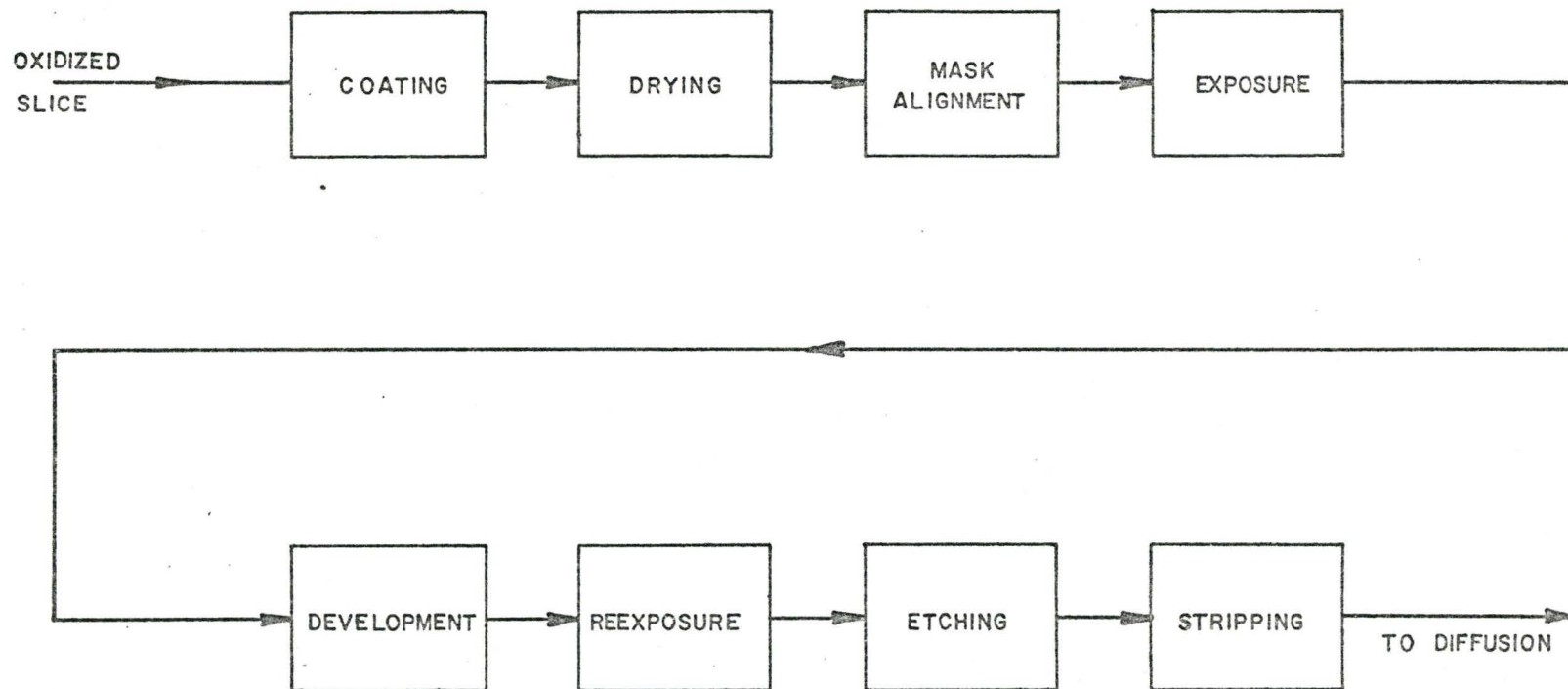
FIGURE (3—7)   FLOW CHART OF THE WINDOW CUTTING PROCESS IN THE OXIDE PRIOR TO DIFFUSION.
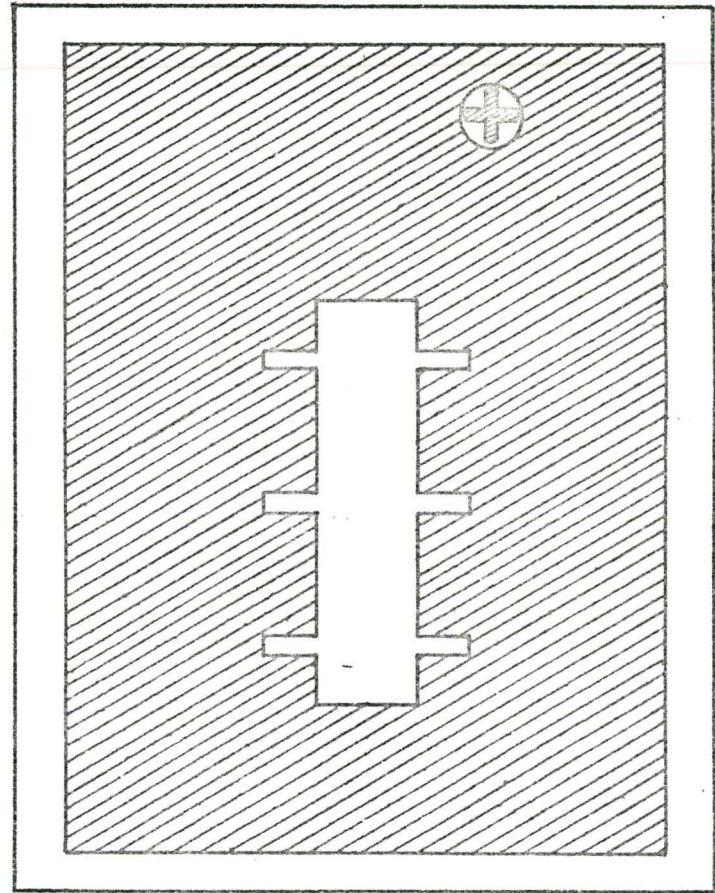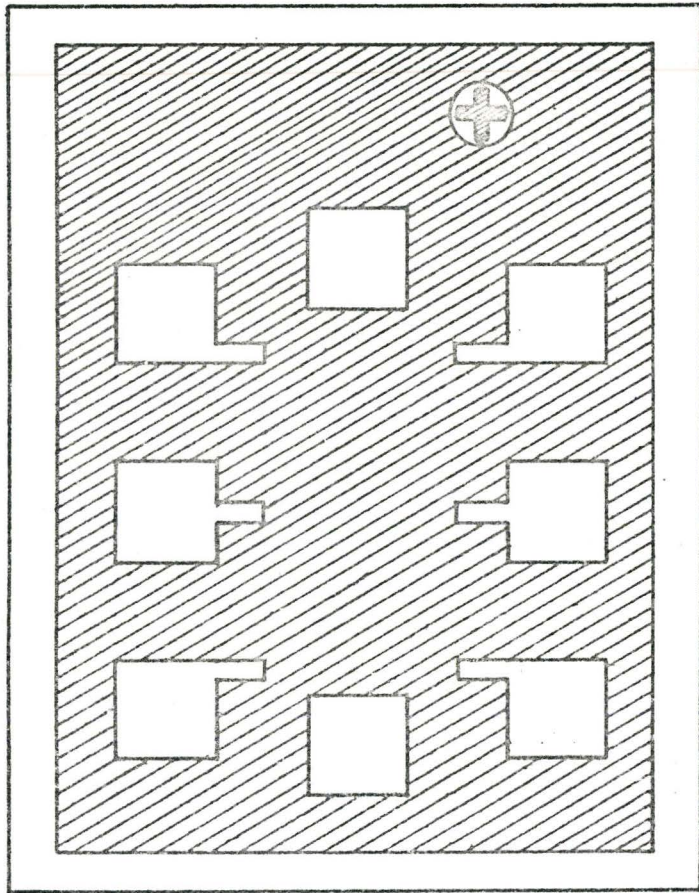
TRANSPARENT AREAS

OPAQUE AREAS

POSITIONING CROSS

FIGURE (3-8) MASKS USED IN THE PHOTOLITHOGRAPHIC PROCESS PRIOR TO DIFFUSION AND ION IMPLANTATIONS.

B. Drying

The slice was heated about 10 - 30 minutes at 100 ^{o}C to drive out all traces of solvent from the photoresist.

C. Mask Alignement

A mask was placed over the slice and manipulated into its desired position with the aid of a microscope.

D. Exposure

Photoresists are exposed by means of collimated ultraviolet light. On exposure, the negative acting photoresist becomes polymerized, and makes it impervious to developing agent . Positive acting photoresists provide a surface coating that is easily dissolved on exposure but insoluable when not exposed. Consequently, they must be used with negatives that are clear in areas in which a window is to be opened and opaque in the remaining areas. Both types of photoresists were used in the sample fabrications. K.P.R. negative acting photoresist with developer was obtained from the Kodak Company, while the positive acting PR.AZ-1350 type was manufactured by Shipley. KOH was a constituent in the developer used with the AZ-1350 photoresist.

E. Development

The slice was rinsed in the proper developer which dissolved the unexposed photoresist (negative PR), but did not effect the exposed region. In case of the positive PR the developer dissolved the exposed areas while the unexposed

ones remained uneffected. A 30-40 min. bake-out followed the development at temperatures between 150-250 ^{o}C as specified by the manufacturer.

F. Etching

The slice was rinsed in a buffered HF acid. This removed the oxide that was not masked by the polymerized PR resulting the desired window. The buffered HF was a dilute solution of HF, buffered with NH_4F to avoid depletion of the flouride ion. A common formulation which was used in this experiment consisted of 1 part by volume cocentrated HF (49%) to 10 parts by volume of NH_4F solution. The NH_4F solution consisted of 1 lb. of NH_4F in 0.68 liter of water. Typical etching rates for silicondioxide were about 7-9 $\overset{o}{A}$/second .

G. Stripping

The final step was to remove the exposed photoresist. This was done by boiling the slices in concentrated sulphuric acid for 20 minutes. Unexposed AZ-1350 PR could be removed by means of acetone.

Diffusion

An open-tube type diffusion system Figure (3-9) was used for the diffusion process. The objective was to produce highly n-type areas in the silicon substrate in order to provide good electrical connections to the ion implanted surface layer.

1000 — 1100°C

TO VENT

QUARTZ SAMPLE HOLDER BOAT

QUARTZ DIFFUSION TUBE

VALVES & FLOWMETERS

LYNDBERG FURNACE

N$_2$

O$_2$
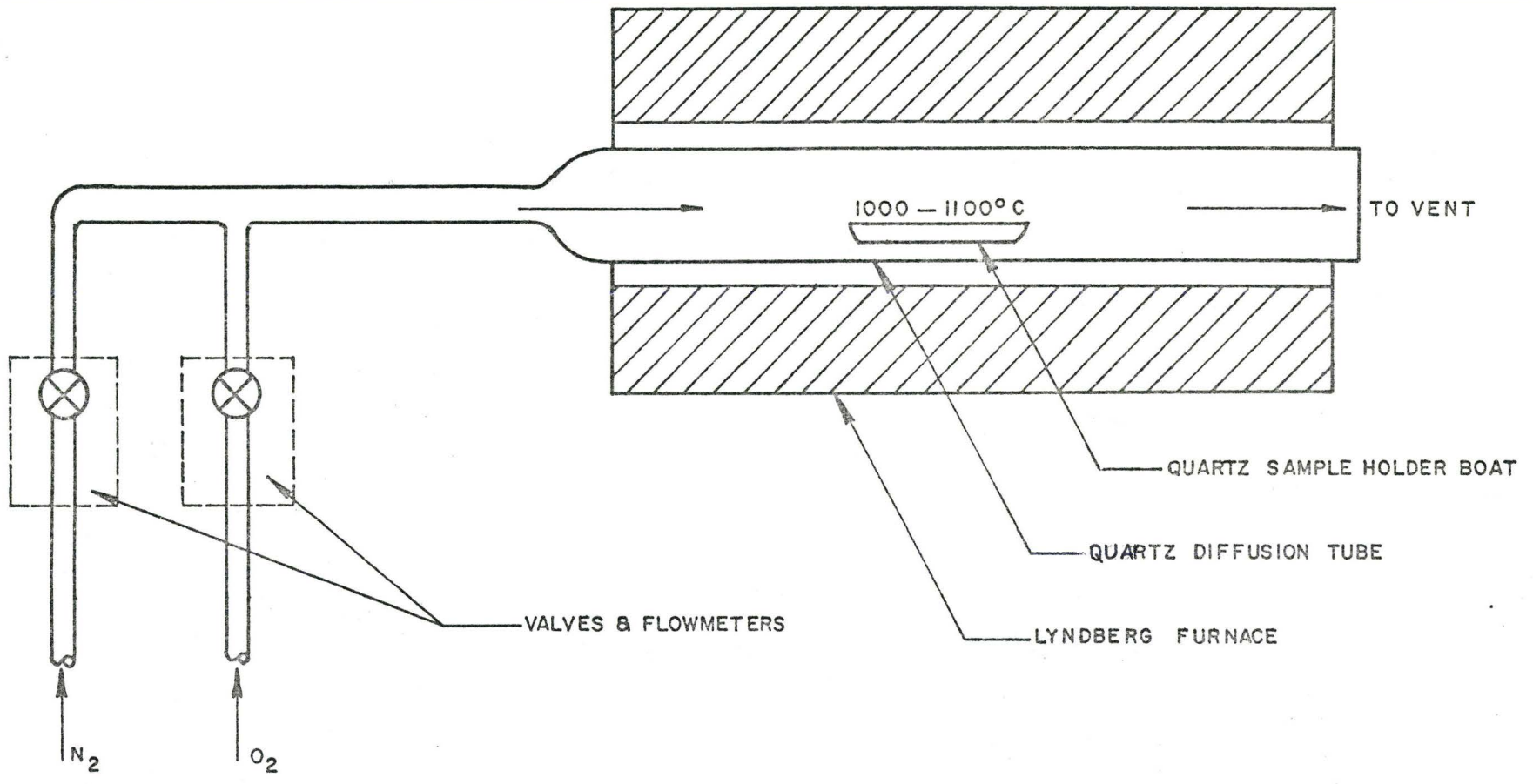
FIGURE (3—9) OPEN TUBE TYPE DIFFUSION.

Open windows were fabricated in the surface oxide layer of the silicon slice by photolithographic technique, prior to diffusion. Then the samples were cleaned again and coated with P_2O_5 emulsion with $C_s = 1 \times 10^{19}$ cm^{-3} surface concentration. The process consisted of spinning the silicon slice at high speed after a small quantity of liquid 'phosphor-silicate' had been placed on it. A thin (2-3 μm) coating layer of the doping material was obtained by the above method. Then the P_2O_5 layer was dried in a furnace at 100 ^{o}C for 20 minutes before placing the silicon substrate into a Lyndberg diffusion furnace. A 40-50 minute diffusion process at 1000 ^{o}C with the above dopant surface concentration produced approximately 1- 1.5 μm deep,highly doped n-type regions in the p-type substrate. Figure (2-10) shows the junction depth versus diffusion time and diffusion temperature for phosphorus doped silicon. After the diffusion, the P_2O_5 glass had to be removed from the surface of the sample. It was etched off by means of dilute HF (10% HF in water) in a very short time (few seconds). The etching process was kept short enough, to avoid removing the protective silicon dioxide surface layer from the substrate. Finally, an electrical test was done to check the result of the diffusion. Rectifying diode characteristics were measured between the highly doped n-type regions and the p-type substrate and displayed on a curve tracer.
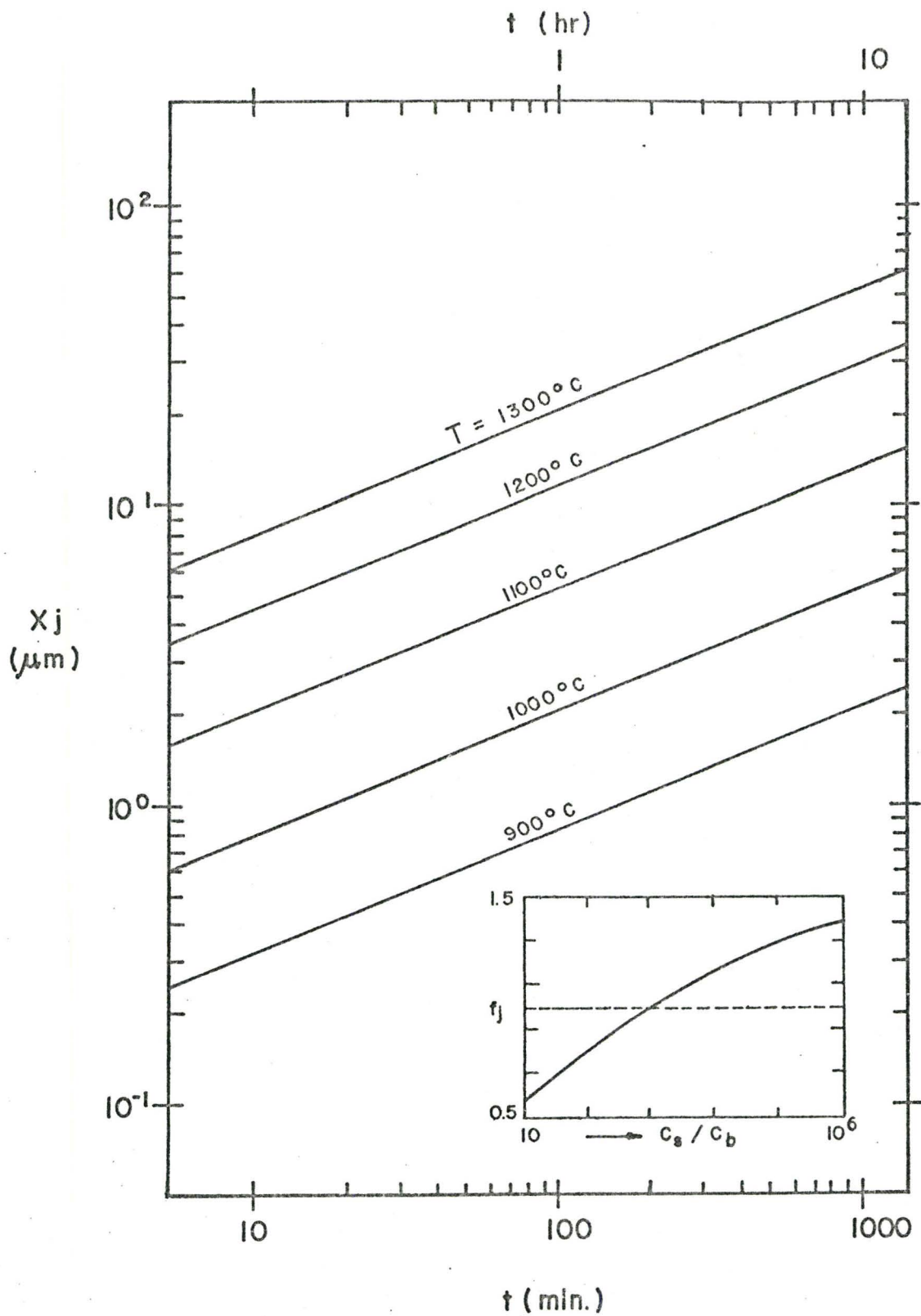
FIGURE (3-10) JUNCTION DEPTH Xj VS. DIFFUSION TIME (t) AND
DIFFUSION TEMPERATURE (T) FOR PHOSPHORUS DOPED SILICON.

After the diffusion process photolithography was used again to open the rectangular window in the oxide for implan-tation. The steps of the photolithographic technique were discussed earlier in detail. Here only the summary is given:

A. Coating with AZ - 1350 Shipley P.R.

B. Baking in oven at $100^{o}C$ for 10-20 minutes.

C. Positioning the 'Hall pattern' mask on the sample.

D. Exposing the P.R. with collimated UV light.

E. Developing the pattern with KOH constituent developer.

F. Rinsing in deionized water.

G. Postbaking the PR. at $125^{o}C$ for 30 minutes.

H. Etching off the SiO_2 where the P.R. was developed, using buffered HF until the clear silicon surface shows up.

I. Rinsing in DI water.

J. Removing the unexposed P.R. by means of acetone.

K. Dipping the sample in dilute HF for a very short time in order to clear the surface but to avoid removing the oxide where it is needed to protect the substrate from the ion bombardment during implantation.

The schematic diagram of the final product of the sample preparation is shown in Fig. (3-11).

Prior to implantation each sample was cleaned using the following cleaning procedure:

Step 1. 10 minutes in 2 H_2SO_4 + 1 H_2O_2 at $60-70^{o}C$ followed
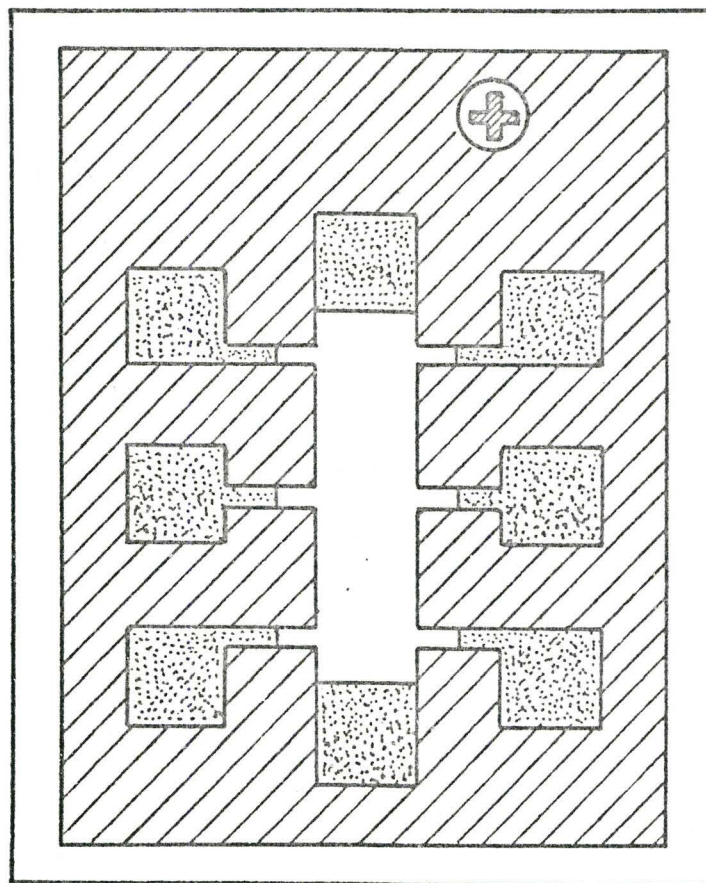
P—TYPE SI SUBSTRATE

N$^+$ HEAVILY DOPED DIFFUSED CONTACTS

SILICONDIOXIDE SURFACE LAYER

FIGURE (3—11) SCHEMATIC DIAGRAM OF A DIFFUSED CONTACT
HALL SAMPLE PRIOR TO IMPLANTATION.

by deionized water rinse.

Step 2.   10 minutes in 4 H_2O + 1 H_2O_2 + 1 HCl at 60-70°C

followed by DI water rinse.

Step 3.   30 seconds in dilute (8%) HF acid solution.

The deionized water employed in the above procedure had

a resistivity of 18 Mohmcm and was obtained from a Millipore

"Super Q" system.

Before each anneal, the samples were cleaned using

the same cleaning procedure as prior to implantation.

IV

EXPERIMENTAL RESULTS AND ANALYSIS

4.1.   Electrical Properties of the Bulk Silicon Samples.

4.1.1. Introduction

In order to determine the accuracy of the automatic Hall effect equipment, low temperature Hall effect experiments were performed on both p- and n-type bulk silicon samples. The experimental results were analysed with a generally accepted method to obtain the ionization energies of the impurities. Activation energy and mobility values were compared with values available in the literature. The preparations of the bulk silicon Hall samples for the Hall effect measurements were already discussed in Section 3.4.1 of the preceding chapter. The samples were mounted in the automatic Hall effect measuring system and measurements were made in the $15^{o}K - 300^{o}K$ temperature range.

4.1.2. Properties of the n-type phosphorus doped silicon.

The results obtained from the experiments are shown on the computer plots, where the carrier concentration (n), normalized carrier concentration ($nT^{-3/2}$), conductivity (σ), and the mobility (μ) are plotted as a function of reciprocal temperature (1/T) in the entire temperature range in Figures (4 - 1 a, b, c, d) respectively.
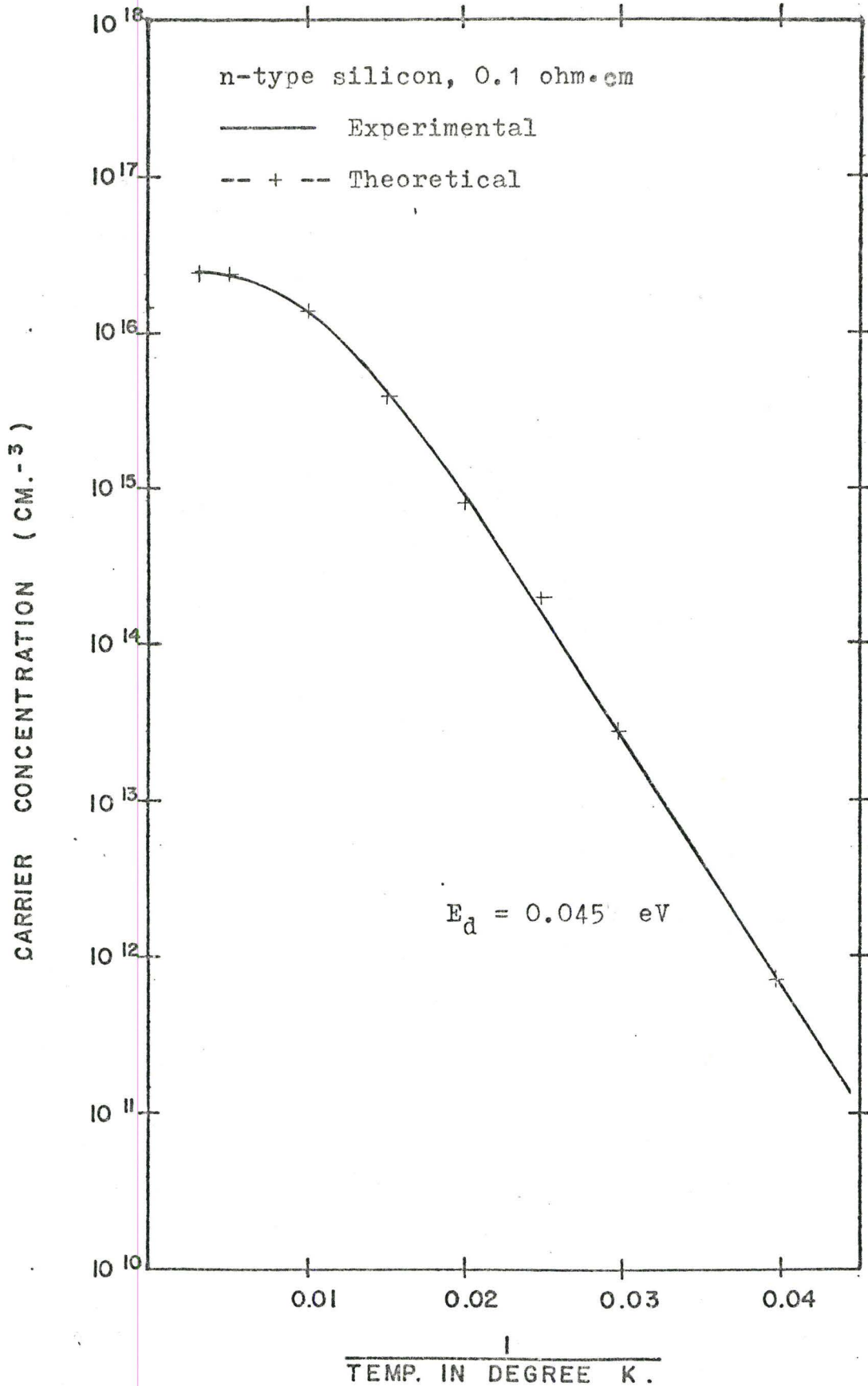
Figure (4-1 a). Carrier concentration (n) vs. reciprocal temperature obtained for a 0.1 ohm·cm resistivity n-type silicon sample.
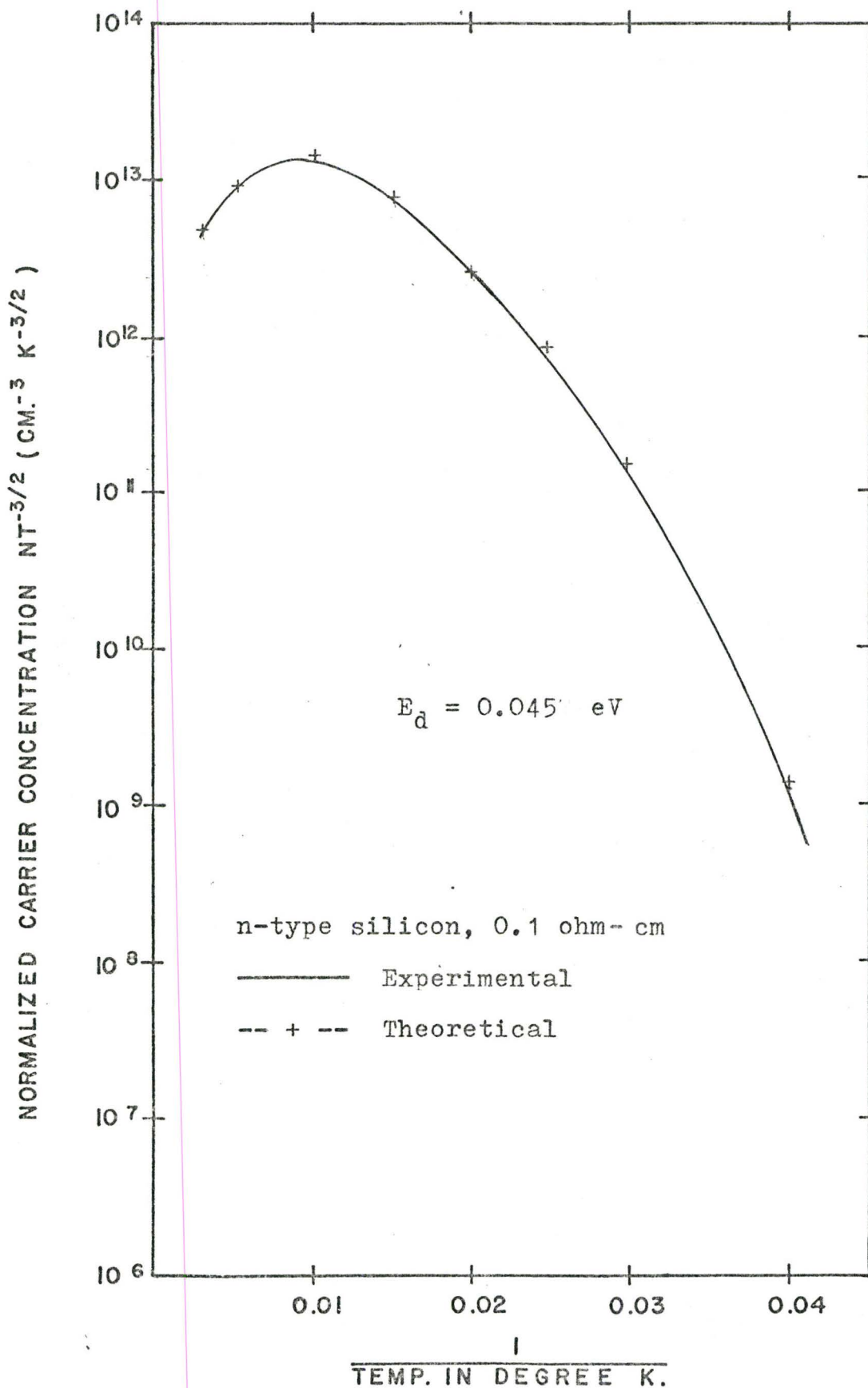
Figure (4-1 b). Normalized carrier concentration ($nT^{-3/2}$) vs. reciprocal temperature obtained for a 0.1 ohm-cm resistivity n-type silicon sample.
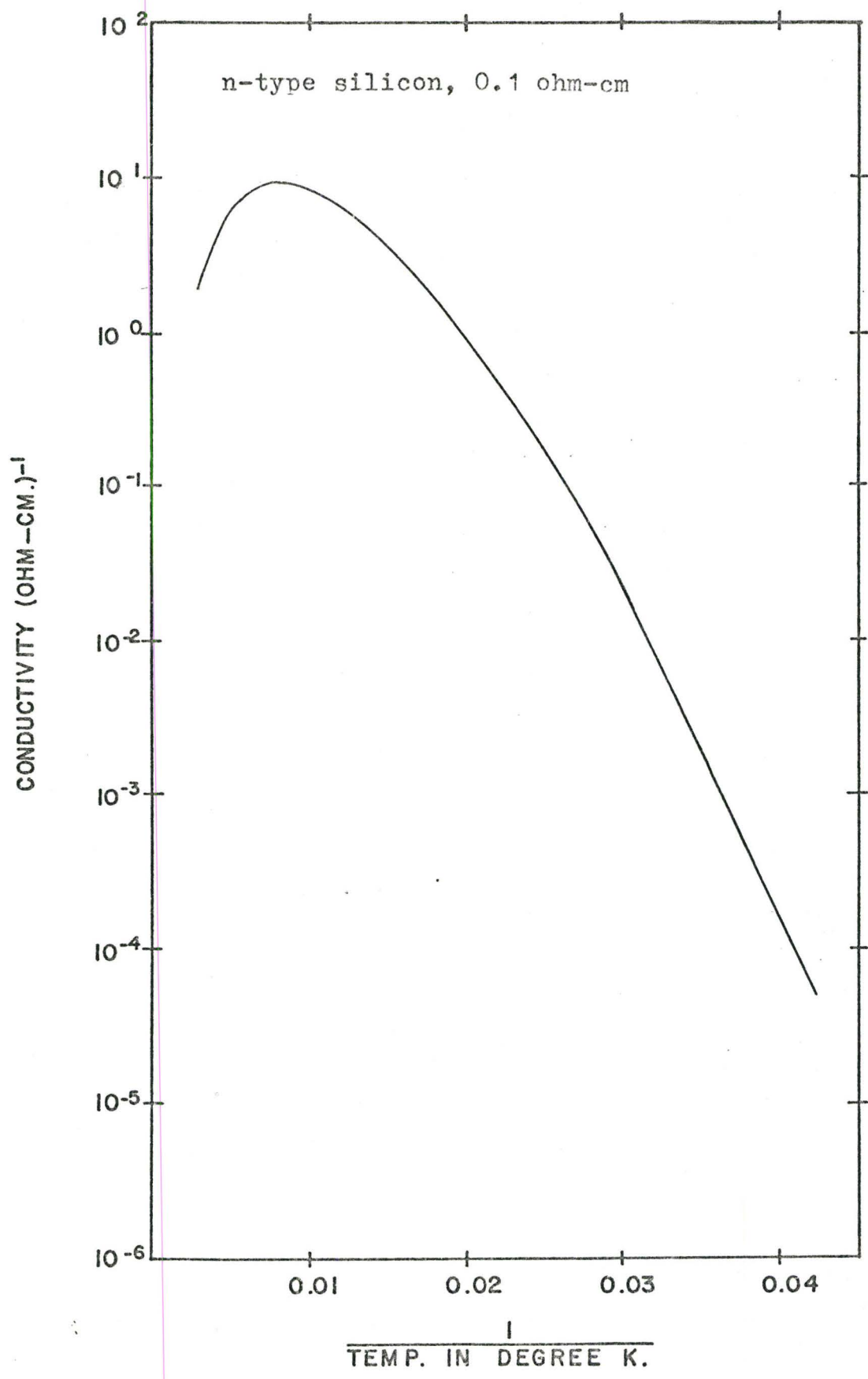
Figure (4-1 c). Conductivity (σ) vs. reciprocal temperature obtained for a 0.1 ohm-cm resistivity n-type silicon sample.
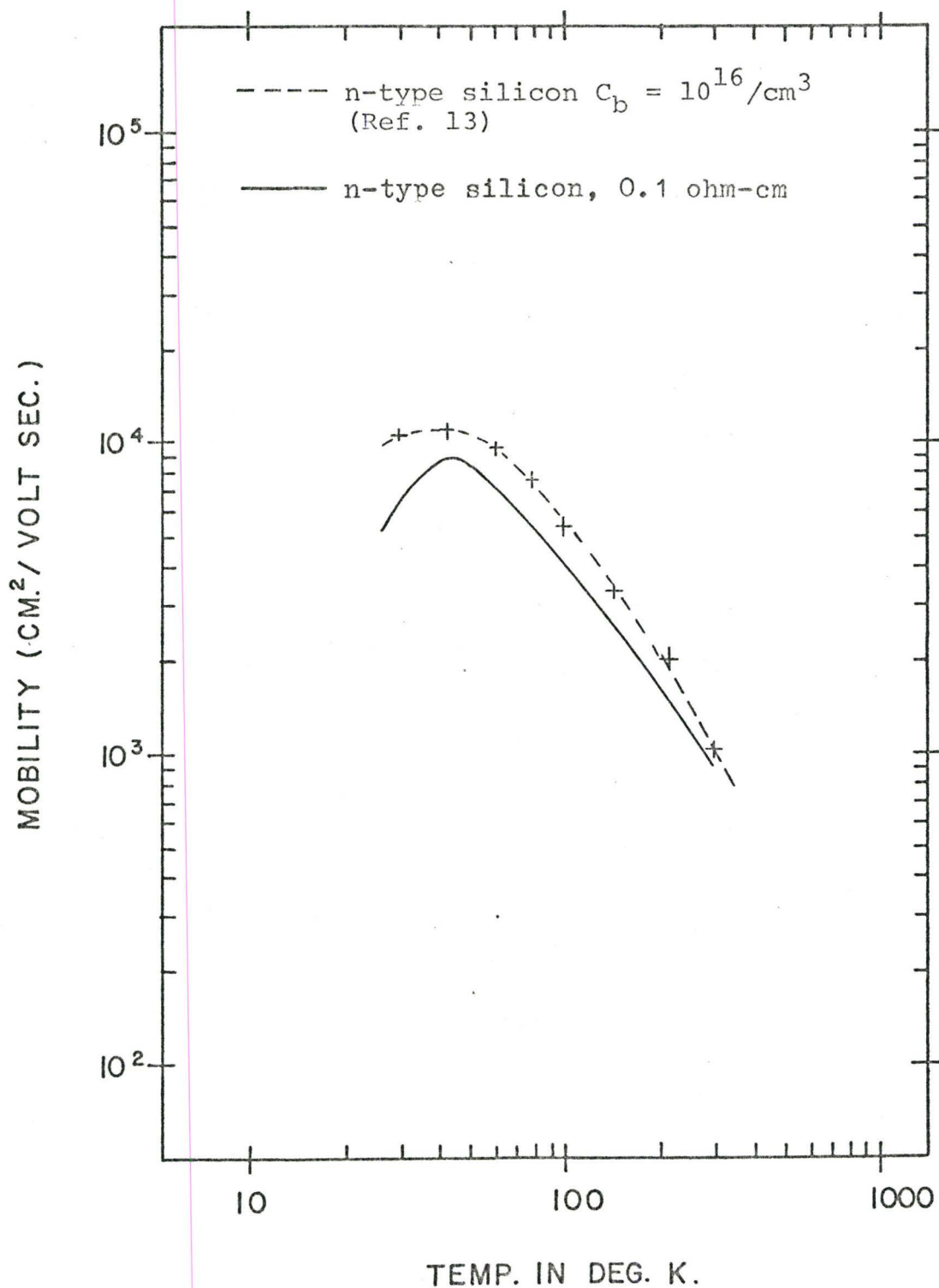
Figure (4-1 d). Mobility vs. reciprocal temperature obtained for a 0.1 ohm-cm resistivity n-type silicon sample.

Analysis.

A partially compensated n-type semiconductor
model (Figure (4-2) was used to determine the activation
energy of the donor and the number of compensating impurity
centers. (N_a).

Equation (4.1) describes the carrier concentration
as the function of temperature, ionization energy, and
the number of donor and compensating acceptor impurities
in the semiconductor.

$$n = \left(\frac{K_d + N_a}{2} \right) \left\{ \left[1 + \frac{4 \, K_d \, (\, N_d - N_a)}{(\, K_d + N_a \,)^2} \right]^{1/2} - 1 \right\} \qquad (4.1)$$

where:

n = number of electrons in the conduction band

N_a = number of acceptors

N_d = number of donors

g_d = donor degeneracy factor = 2

N_c = density of states in the conduction band

K_d = equilibrium constant

$$K_d = \frac{N_c}{g_d} = 2.7 \times 10^{15} \times T^{3/2} \exp \left(- \frac{E_d}{kT} \right) \qquad (4.2)$$

$$N_c = 4.82 \times 10^{15} \times T^{3/2} \left(\frac{m_n}{m_o} \right)^{3/2} \qquad (4.3)$$

$\frac{m_n}{m_o}$ = 1.08 effective mass of the electron
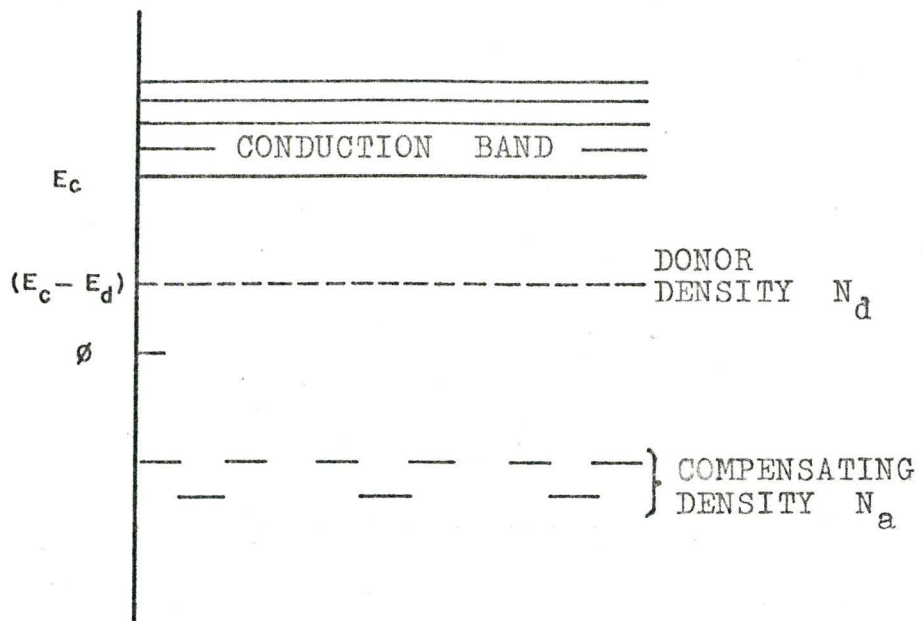
A. N—TYPE

Figure (4 - 2). Energy level diagram of a partially compensated n-type semiconductor model.

B. P—TYPE
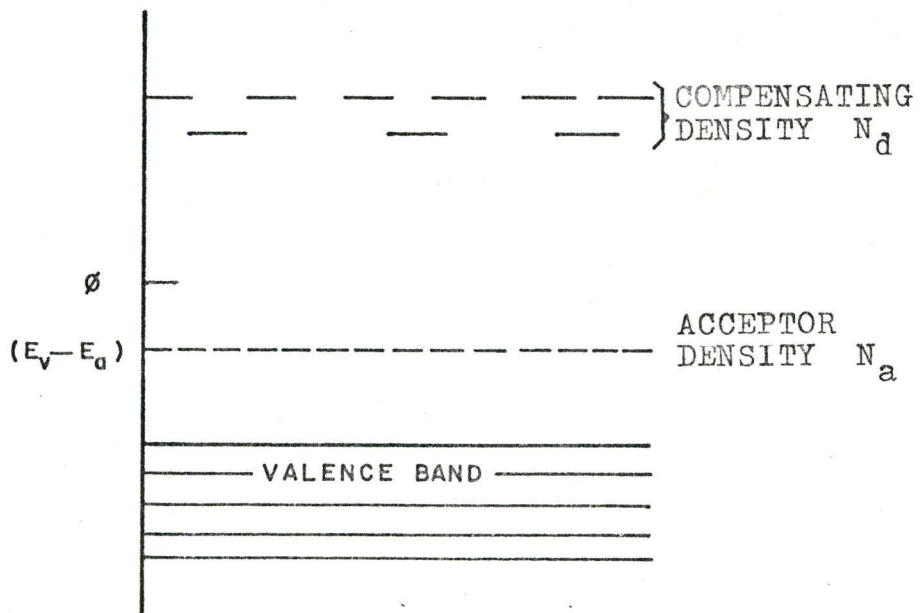
Figure (4 - 4). Energy level diagram of a partially compensated p-type semiconductor model.

The ionization energy of the donor impurities was determined from the gradient of the plot of normalized carrier concentration versus 1/T. It was possible to fit the experimental curve in the entire temperature range of interest, with a theoretical one by using Equation (4.1). The following parameters were obtained from the analysis:

$$E_d = 0.045 \ eV \pm 0.001 \ eV$$
$$N_d = 2.27 \times 10^{16} \ donors/cm^3$$
$$N_a = 2.91 \times 10^{13} \ acceptors/cm^3$$

The temperature dependence of mobility was compared with the mobility of an n-type (As-doped) silicon, measured by Morin and Maita [13]. The activation energy of phosphorus in silicon determined from this experiment is in good agreement with the generally accepted value of 0.045 eV. [14]

4.1.3. Properties of the p-type, boron doped silicon.

A 2 ohm-cm resistivity sample was prepared, mounted and measured in the same way as the n-type silicon sample. The carrier concentration, normalized carrier concentration, conductivity and mobility versus reciprocal temperature curves are presented in Figures (4 - 3a, b, c, d).

Analysis

A model of a partially compensated p-type semiconductor was used to describe the temperature dependence of
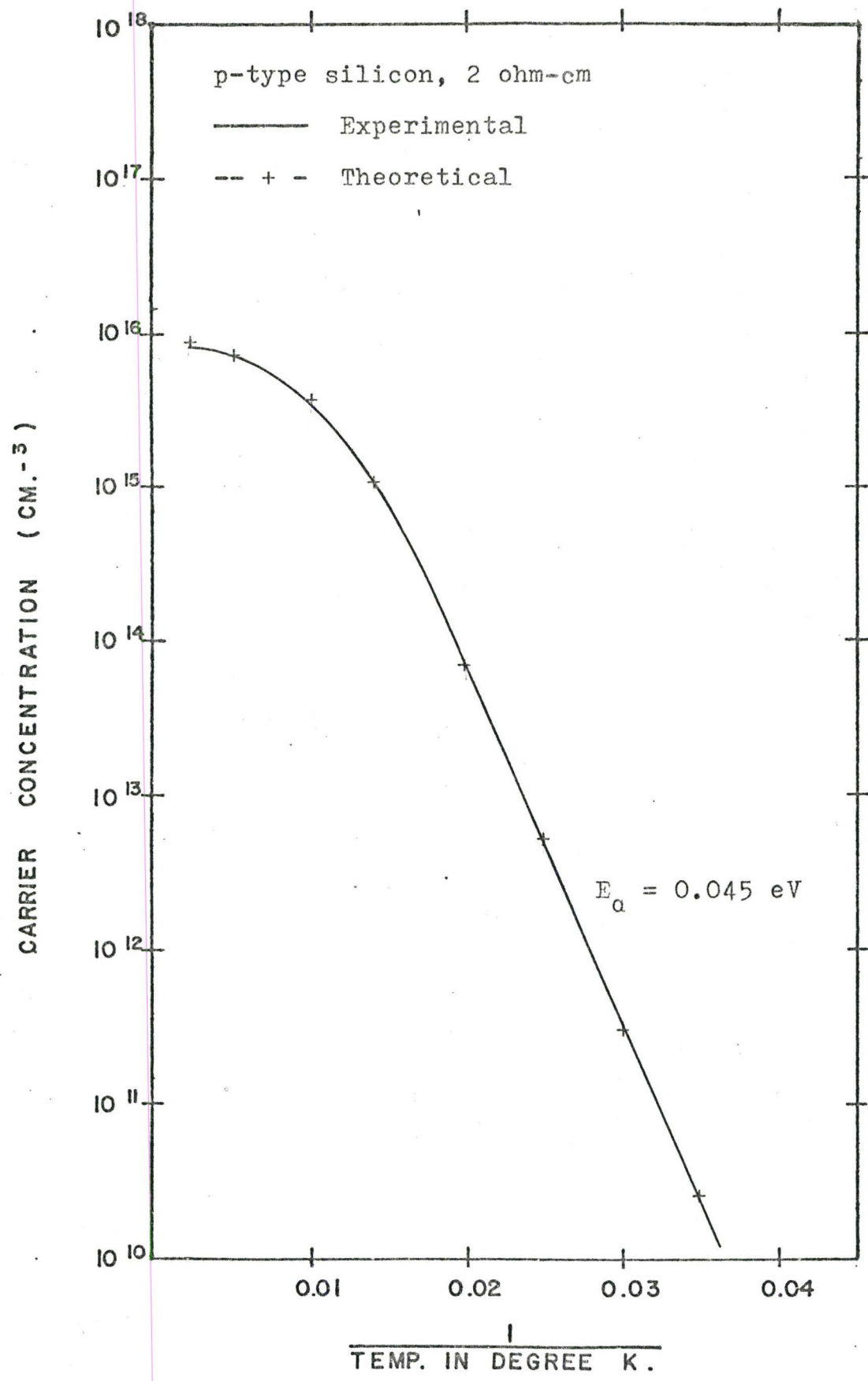
Figure (4-3 a).   Carrier concentration vs. (1/T) graph of a
2 ohm-cm resistivity p-type silicon sample.
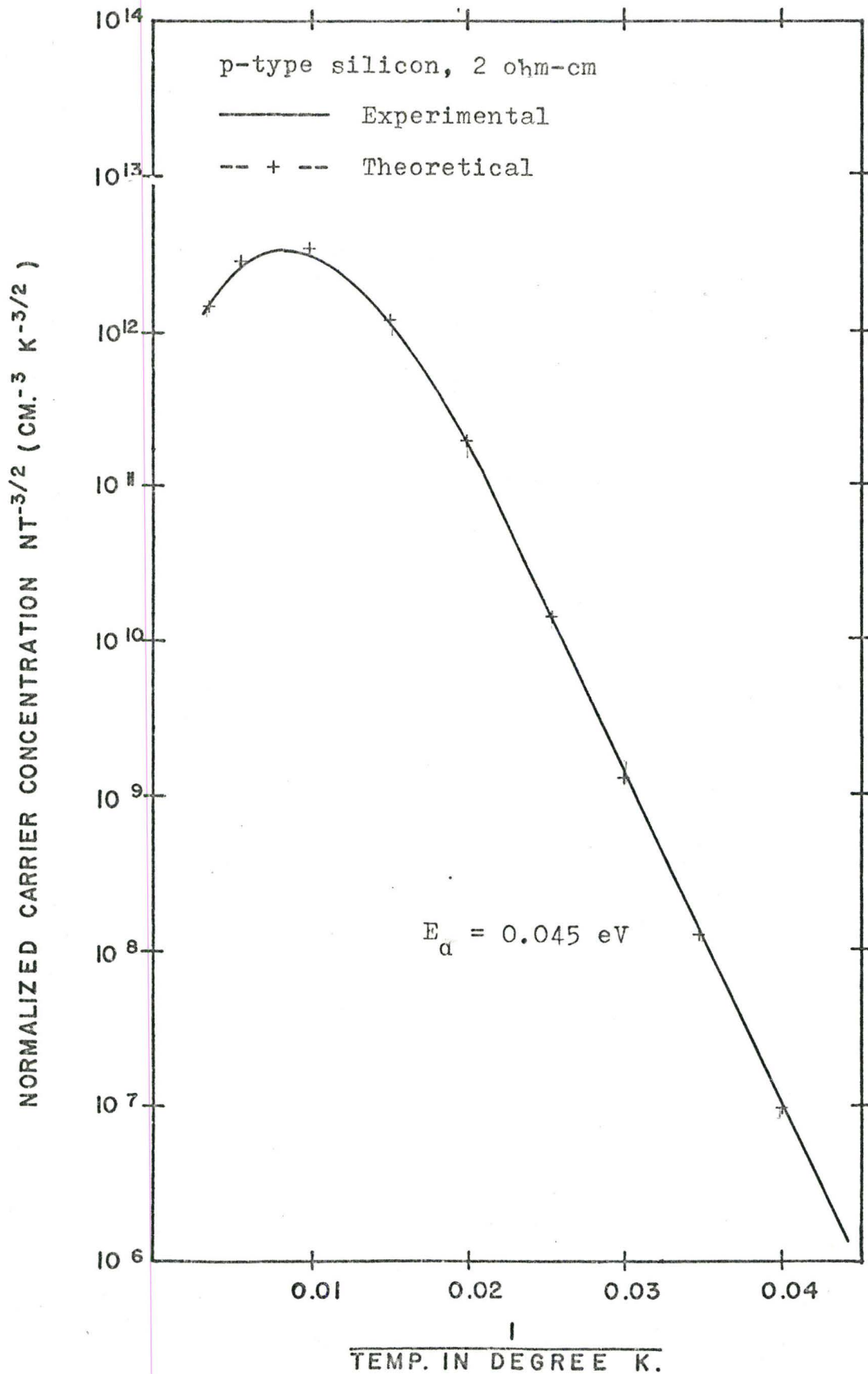
Figure (4-3 b). Normalized carrier concentration vs. (1/T) graph of a 2 ohm-cm resistivity p-type silicon sample.
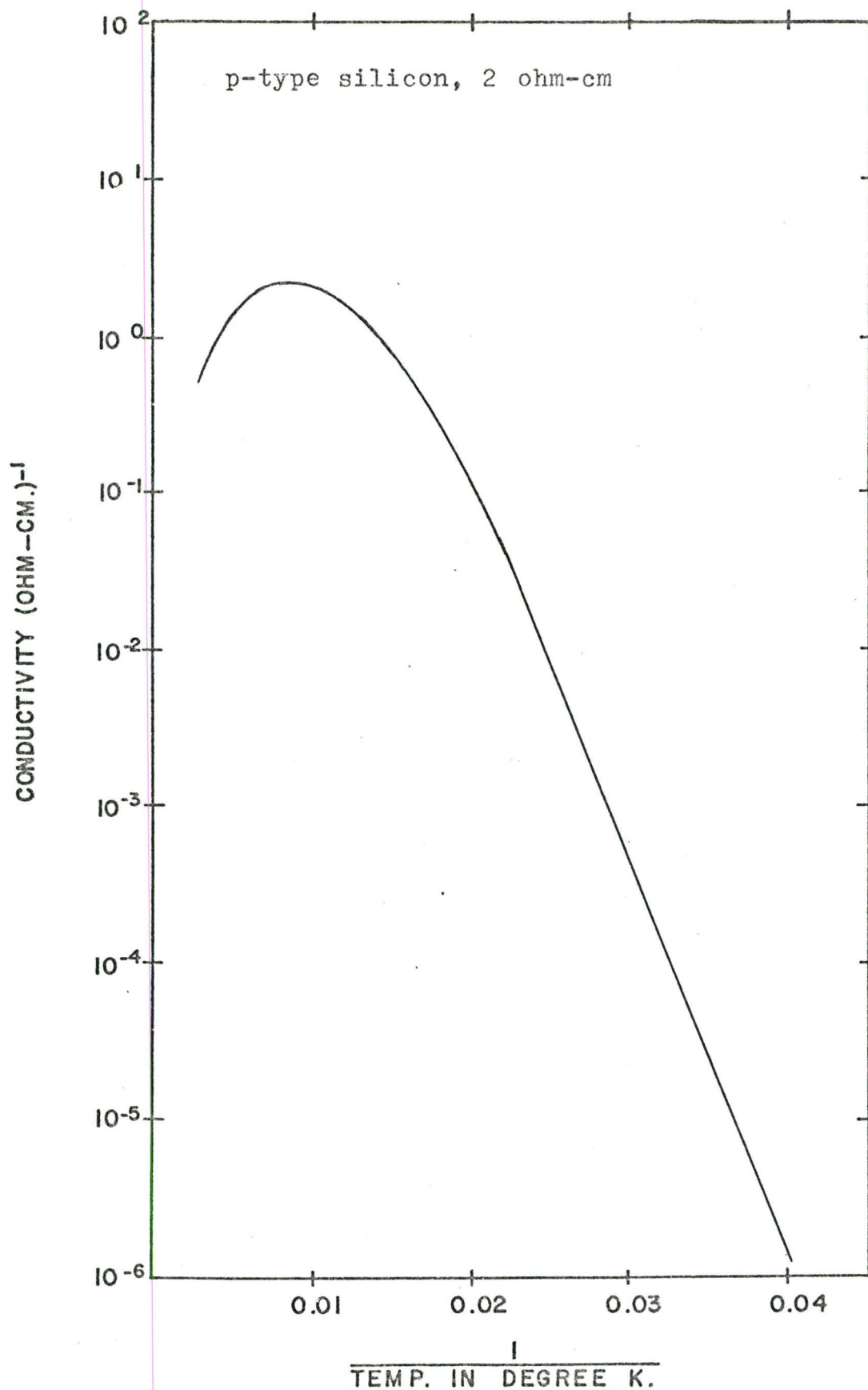
Figure (4-3 c). Conductivity vs. (1/T) graph of a 2 ohm-cm
resistivity p-type silicon sample.
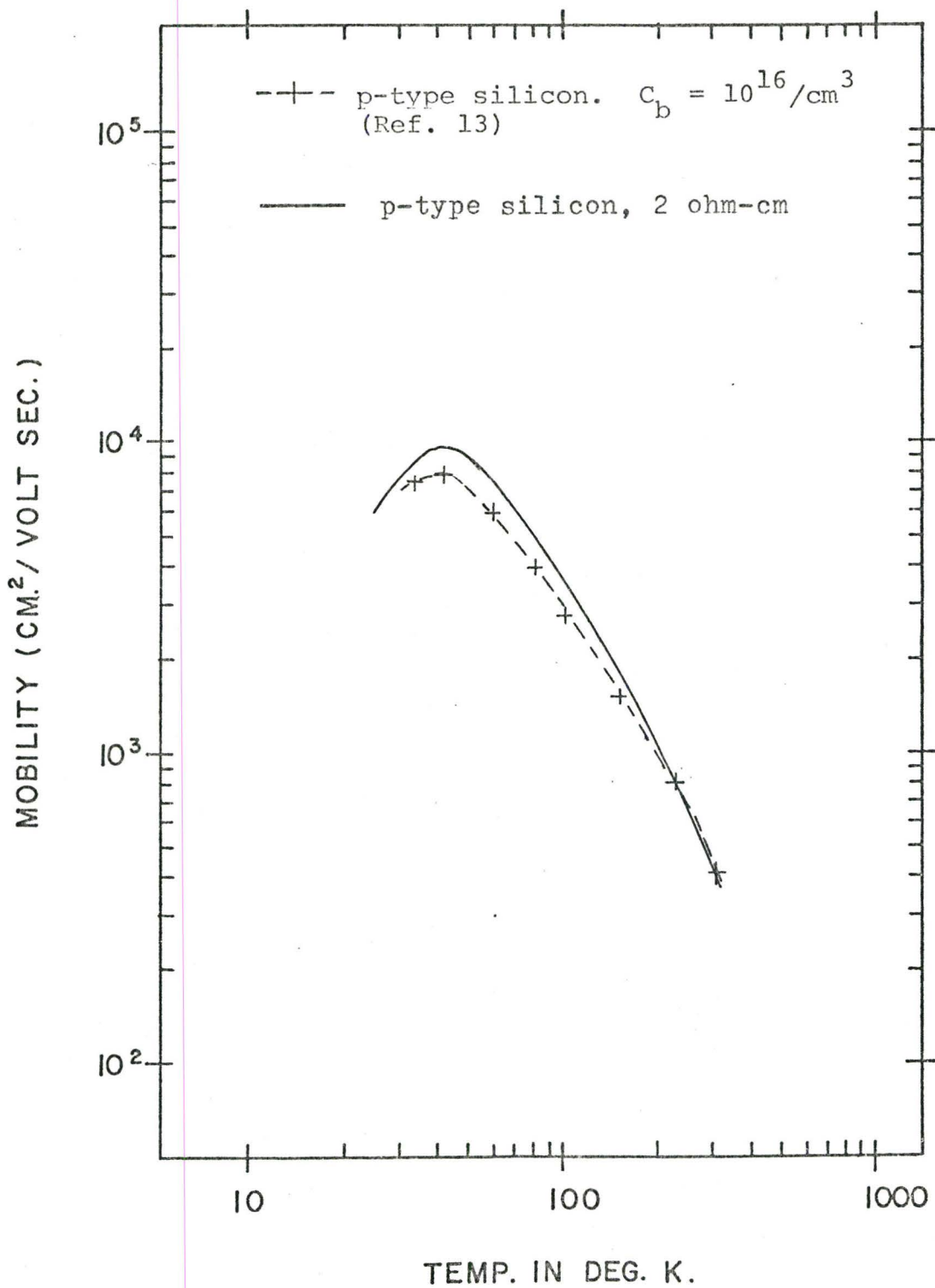
Figure (4-3 d). Mobility vs. (1/T) graph of a 2 ohm-cm resistivity p-type silicon sample.

the electrical properties of the sample[11] (Figure 4-4).

The number of holes in the valence band at a temperature T is given by Equation (4.4).

$$p = \left(\frac{K_a + N_d}{2} \right) \left[1 + \frac{4 K_a (N_a - N_d)}{(K_a + N_d)^2} \right]^{1/2} - 1 \qquad (4.4)$$

where:

K_a = equilibrium constant

g_a = acceptor degeneracy factor = 4

N_v = density of states in the valence band

$$K_a = \frac{N_v}{g_a} = 1.2 \times 10^{15} \times T^{3/2} \exp \left(- \frac{E_a}{kT} \right) \qquad (4.5)$$

$$N_v = 4.82 \times 10^{15} \times T^{3/2} \left(\frac{m_p}{m_o} \right)^{3/2} \qquad (4.6)$$

$\frac{m_p}{m_o} = 0.59$, effective mass of holes

The following values were obtained from the analysis and used to approximate theoretically the experimental curve of carrier concentration versus $1/T$:

$E_a = 0.045$ eV $\pm$ 0.001 eV

$N_a = 8.58 \times 10^{15}$ acceptors/cm^3

$N_d = 5.88 \times 10^{14}$ donors/cm^3

A mobility versus T curve of a boron doped silicon sample is also provided for comparison [13]. The above E_a activation

energy is very close to the 0.044 - 0.045 eV values for boron in silicon, measured by Morin and Maita [13].

4.1.4. Summary

The electrical properties of a phosphorus - doped, n-type, and a boron - doped, p-type silicon samples were investigated in the 15 ^{O}K - 300 ^{O}K temperature range.

Partially compensated semiconductor models were used to analyse the experimental results. The activation energies of the phosphorus and boron impurities in silicon were determined as 0.045 $\pm$ 0.001 eV, and 0.045 $\pm$ 0.001 eV respectively. These values are in good agreement with the generally accepted values of ionization energies of the above two impurities. The deviation is within the experimental error of the conductivity and Hall effect measurements, as the accuracy of the temperature measurement was $\pm$ 1^{O}K. Mobility versus temperature curves were also provided for comparison in both cases from available references.

It was necessary to carry out these experiments before starting to investigate the electrical properties of ion implanted silicon samples in order to ensure that the automatic Hall effect measuring equipment was calibrated and to determine the overall accuracy of the system.

4.2   Nitrogen Ion Implanted Silicon Samples.

4.2.1. Introduction

The electrical properties of nitrogen ion implanted silicon layers were investigated as a function of various implantation and annealing conditions. Low temperature Hall effect measurements were made to characterize the ion implanted layers i.e. to determine the carrier concentration and mobility in the layer, the activation energy of the implanted ions and the amount of compensating centers present in the implanted layer. The depth distribution of free carriers were determined theoretically (Ref. 16.). Normalized carrier concentration versus temperature curves were obtained in the $15^{\circ}K - 300^{\circ}K$ temperature range and analysed for each sample.

The p-type silicon substrate was manufactured by the Monsanto Co. and had a resistivity of approximately 10 ohm-cm (7.66 - 13.33 ohm-cm) The sample preparation prior to implantation is previously discussed in section 3.4.3 of Chapter III. The samples had $\langle 111 \rangle$ crystal orientations and missaligned several degrees to the implantation axis to avoid channeling effects. The implants were performed in 2.5×10^{-6} Torr vacuum. Implantations were made at room temperature and also at $(100^{\circ}K)$ low temperature in order to study the correlation

between the amount of crystal damage introduced by the implantation, and the resulting electrical conversion efficiency following a high temperature anneal [16]. The results of the above study was presented in Ref. 16, with the conclusion that the electrical behaviour observed in nitrogen implanted silicon depends on the implantation and annealing conditions.

The purpose of this study was to determine whether the various implantation conditions such as dose rate, total dose, implantation temperature, layer profile, and annealing conditions have effects on the electrical properties of the nitrogen ion implanted silicon layers or not.

4.2.2. Experimental Results

Silicon samples, fabricated from a p-type substrate with heavily doped n-type, diffused contacts (Fig. 4-5) were used for ion implantations. Dose rate was $20-30 \times 10^{-9}$ Amps normally, but implantations were made with dose rate as low as 5×10^{-9} Amps/cm^2 and as high as 300×10^{-9} Amps/cm^2. Samples were implanted with total dose as low as 1.4×10^{14} ions/cm^2 and as high as 8×10^{14} ions/cm^2. 80 keV and 40 keV ion beams with dose ratio 3:1 were used to develop a relatively uniform implant layer.
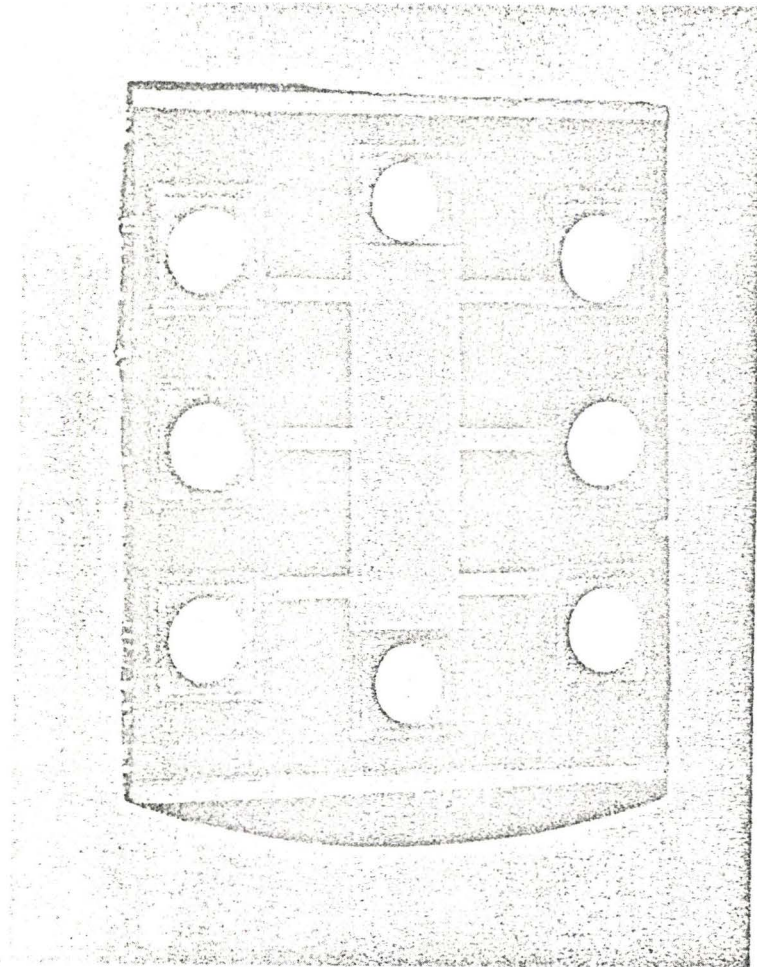
Figure (4 - 5). Diffused contact Hall sample with aluminium
contacts.

A different layer profile was established in one sample implanted with only a 50 keV ion beam. The schematic diagram of the dopant distribution profiles for both cases are shown in Figures (4-6) and (4-7). The theoretical depth (2000-2500 $\overset{o}{A}$) of the implanted layer was checked by means of room temperature Hall effect measurements combined with anodization and HF acid stripping [16]. The location of the p - n junction was determined to be approx. 2000 $\overset{o}{A}$ from the surface of the substrate, and this value was used in the analysis of the Hall effect data.

Following implantation, the samples were annealed in a quartz tube of a Lyndberg furnace. One end of the quartz tube was vacuum sealed, the other was connected to a vacuum system consisting of a liquid nitrogen trapped oil diffusion pump and a mechanical prevacuum pump. Anneal temperature could be set between 100 ^{o}C and 1200 ^{o}C, and the vacuum pressure was less than 2 x 10^{-6} Torr during anneal. Generally, the samples were subjected to 10 minute anneal cycles at a given temperature and then they were measured on the automatic Hall effect measuring equipment. Carrier concentration vs. $1/T$, mobility vs. $1/T$, and conductivity vs. $1/T$ graphs were plotted for temperatures between 15 ^{o}K and 300 ^{o}K , for each sample. In order to determine the activation energies of the impurities and the compensating impurity concentrations, the normalized
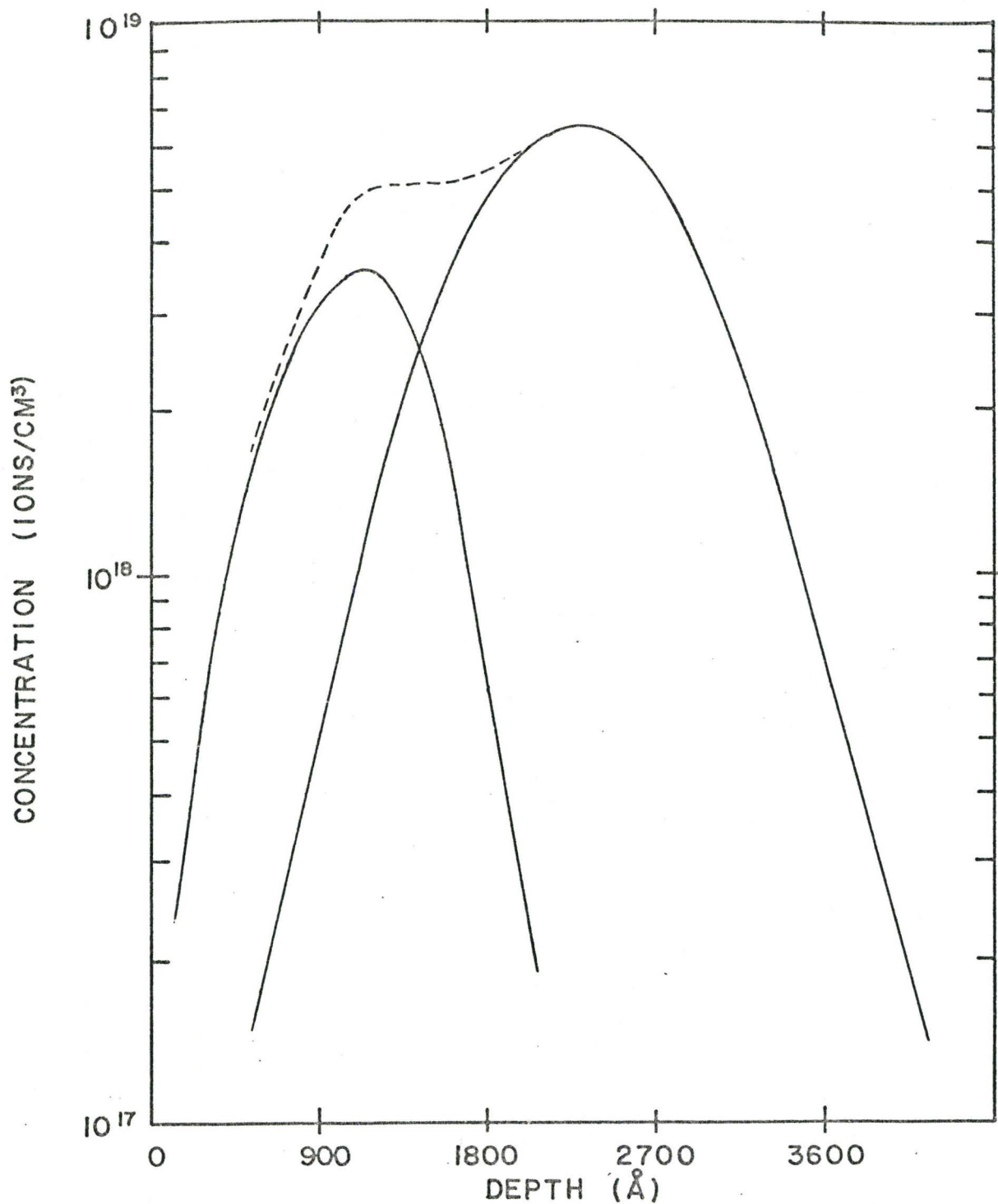
Figure (4-6). The theoretical distribution of 80/40 keV
nitrogen in silicon. The dose ratio is 3:1.
The dotted line is the resultant distribution.
(Ref. 16)
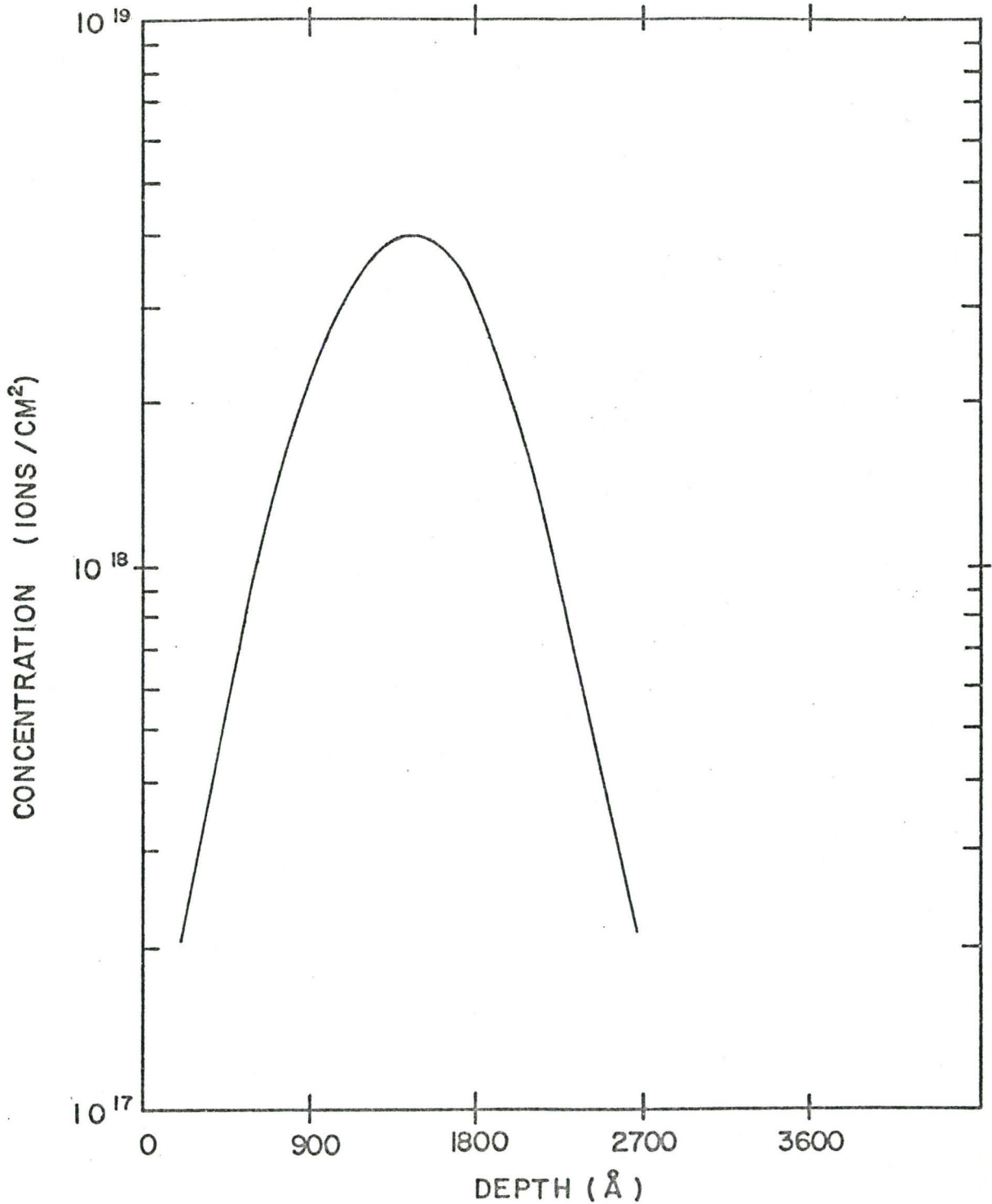
Figure (4-7). The theoretical distribution of 50 keV nitrogen
in silicon.

carrier concentration versus reciprocal temperature curves were analysed.

At the first attempt, a partially compensated n-type semiconductor model was used to determine the electrical properties of the nitrogen implanted samples. This model was applicable only to obtain an ionization energy value from the low temperature Hall effect and conductivity measurements. However, it failed to describe the carrier concentration function in the intermediate (65 ^{o}K - 200 ^{o}K) temperature range. Although all normalized carrier concentration curves could be characterized by the same ionization energy at low temperatures, the presence of another donor energy level might be responsible for the particular behaviour at intermediate temperatures. By comparing the n vs 1/T curves of the implanted samples to the same curves of the bulk silicon samples, the possibility of the presence of a second, deeper donor level in the energy band structure of the implanted samples seemed to be obvious. It was possible to approximate the carrier concentration curves resulted from the experiments in the entire temperature range (15°K-300°K) with theoretical ones, which were obtained by using a n-type semiconductor model having two monovalent donor levels and a compensating acceptor impurity level. The analysis of the experimental results on the basis of the above model is presented later in this chapter, following the pre-

sentation of the experimental results.

Six nitrogen implanted silicon samples were pro-
duced. The implantation and annealing conditions are tabu-
lated in Table 4.1 . Dose ratio was defined as the ratio
of the 80 keV and 40 keV implantation doses. The total
dose is the sum of the two doses implanted by the two
different energy implantations. Figure (4-8) shows the
number of active impurities in the nitrogen implanted
layer as a function of the total dose. It can be seen
that the application of nitrogen implantation doses
higher than $2 - 3 \times 10^{14}$ ions/cm^2 are not practical.

The carrier concentration, normalized carrier
concentration, conductivity, and mobility versus recip-
rocal temperature graphs for the six nitrogen implanted
samples are shown in Figures (4-9, 4-10, 4-11, 4-12,
4-13, and 4-14) respectively. The points of the theo-
retical approximations of the carrier concentration
functions obtained from the analysis are also plotted
beside the experimental curves for comparision.

SAMPLE	SI-146	SI-170	SI-171	SI-192	SI-58	SI-35
IMPLANT TEMP. ($^\circ$K)	100	100	100	300	300	300
TOTAL DOSE ($1/cm^2$)	1.4×10^{14}	2.8×10^{14}	1.4×10^{14}	1.4×10^{14}	6.0×10^{14}	1.4×10^{14}
DOSE RATE (nA/cm^2)	30-40	30-40	20-40	30-40	200	50
1st IMPLANT ENERGY (keV)	80	80	80	80	80	50
2nd IMPLANT ENERGY (keV)	40	40	40	40	40	—
ANNEAL TEMP. ($^\circ$C)	825	825	825	825	825	825
TOTAL ANNEAL TIME (MIN.)	10	20	30	30	10	20
CARRIER CONC. (cm^{-3})	4.3×10^{16}	7.8×10^{16}	4.0×10^{16}	3.6×10^{16}	1.25×10^{16}	3.12×10^{16}

Table 4.1 Summary of the implantation and annealing conditions of the nitrogen
ion implanted silicon samples.
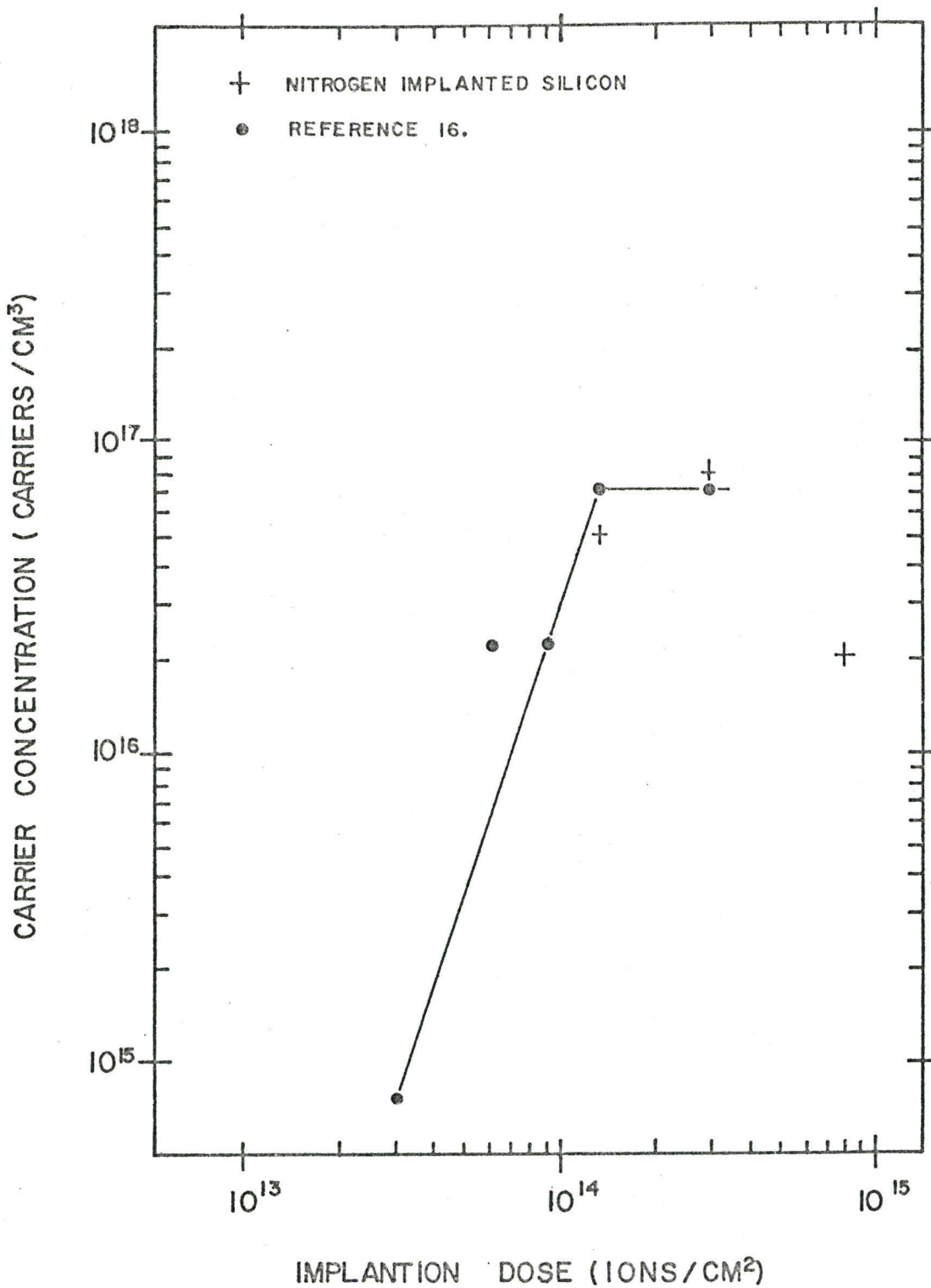
Figure (4 - 8). The number of active impurities produced in nitrogen implanted silicon as a function of implantation dose.
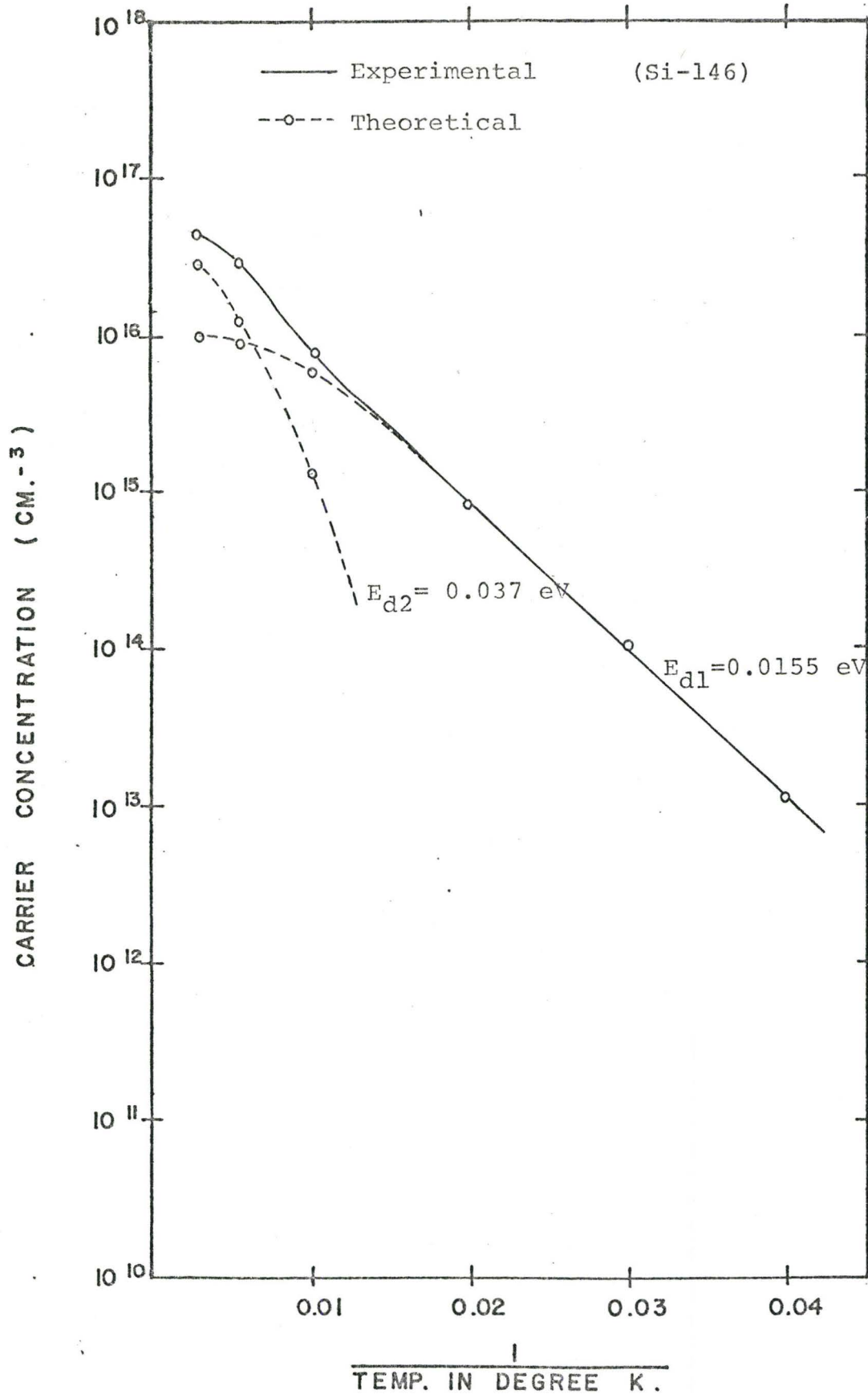
Figure (4-9 a). Carrier concentration vs. (1/T) graph of silicon sample (Si-146) implanted at $100^{\circ}K$ with 1.4×10^{14} N/cm^2, 80/40 keV.
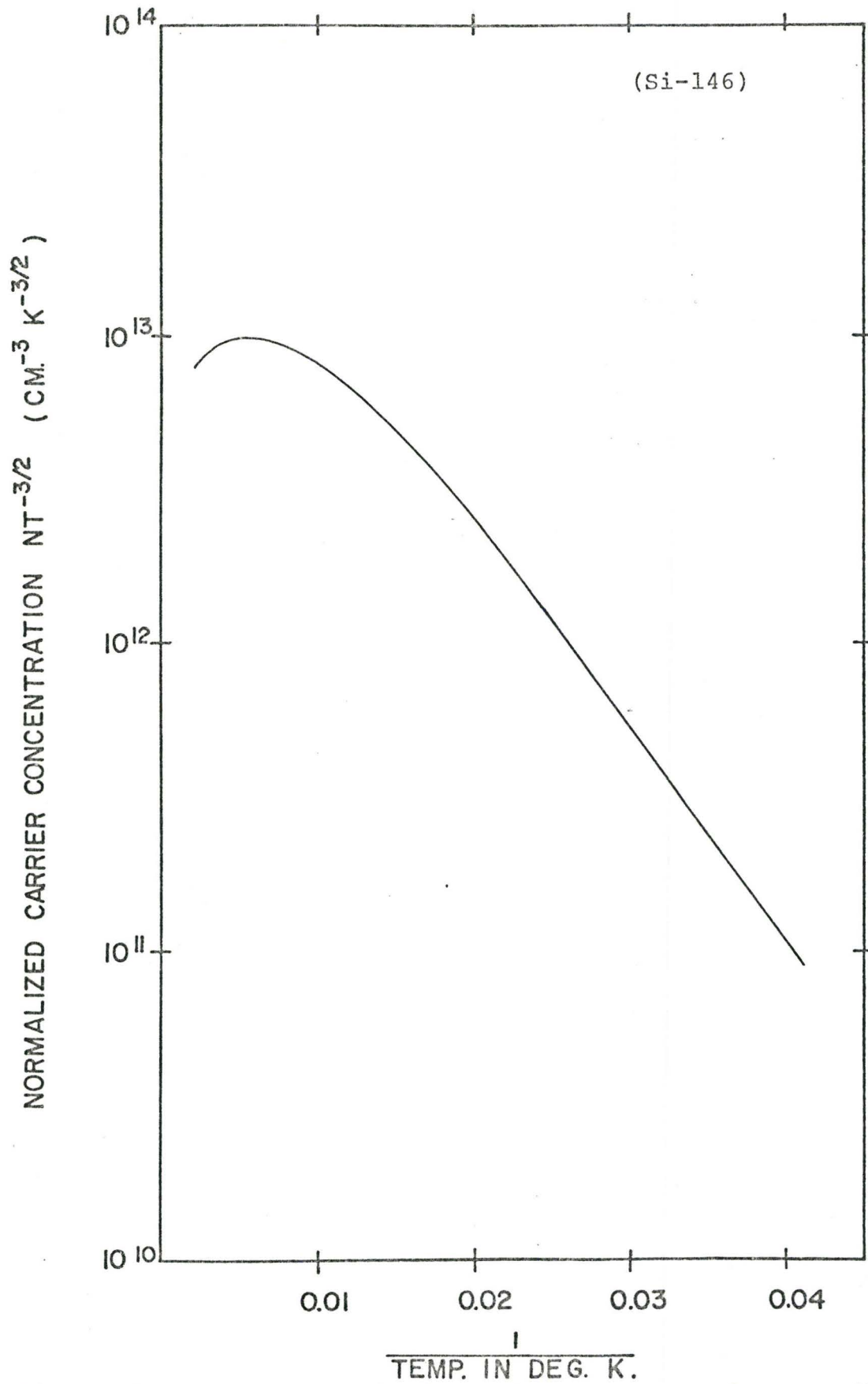
Figure (4-9 b). Normalized carrier concentration vs. (1/T)
graph of a silicon sample (Si-146) implanted
at $100°$ K with 1.4×10^{14} N/cm^2, 80/40 keV.
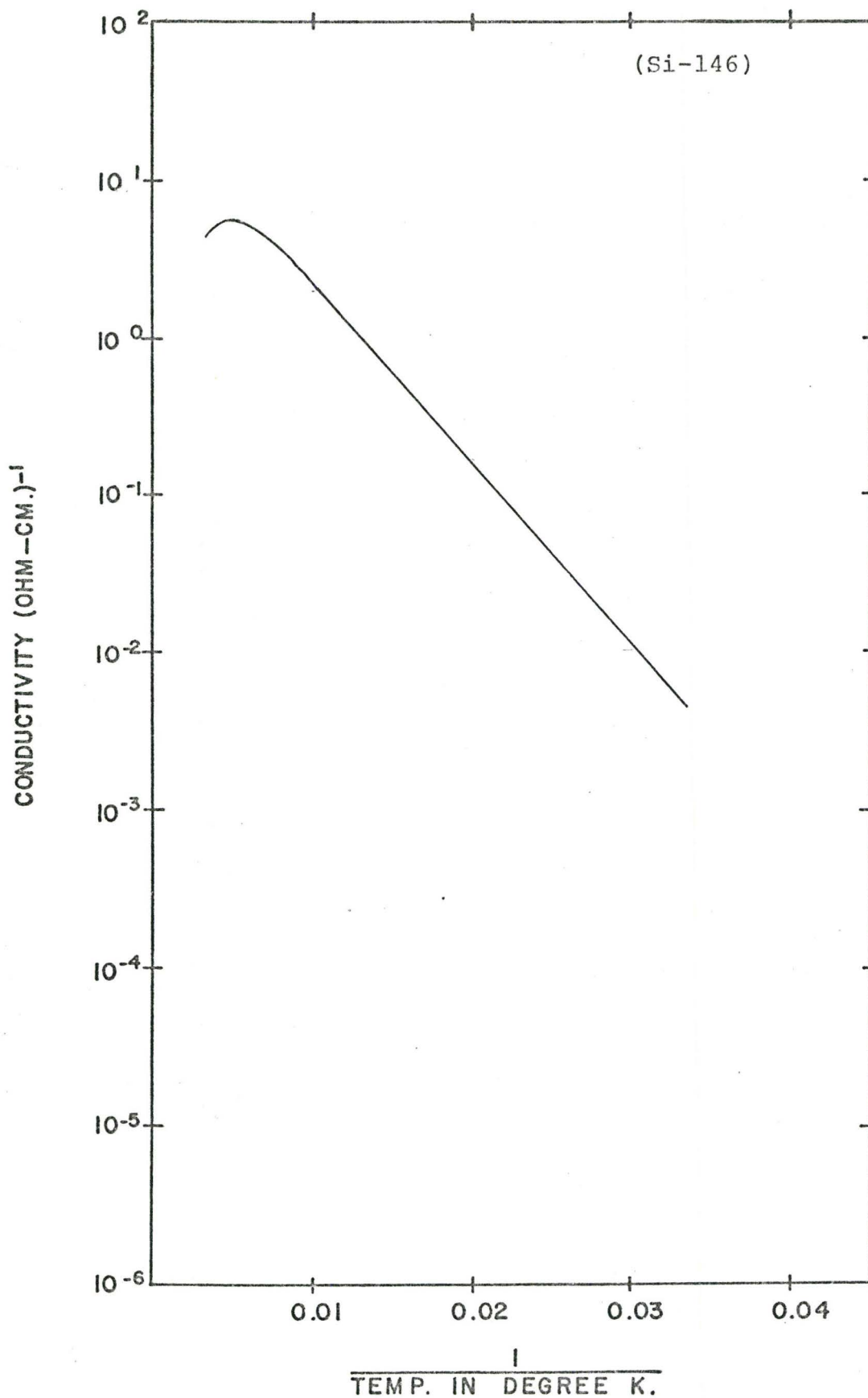
Figure (4-9 c).   Conductivity vs. (1/T) graph of a silicon
                  sample (Si-146) implanted at 100°K with
                  1.4×10^{14} N/cm^2, 80/40 keV.
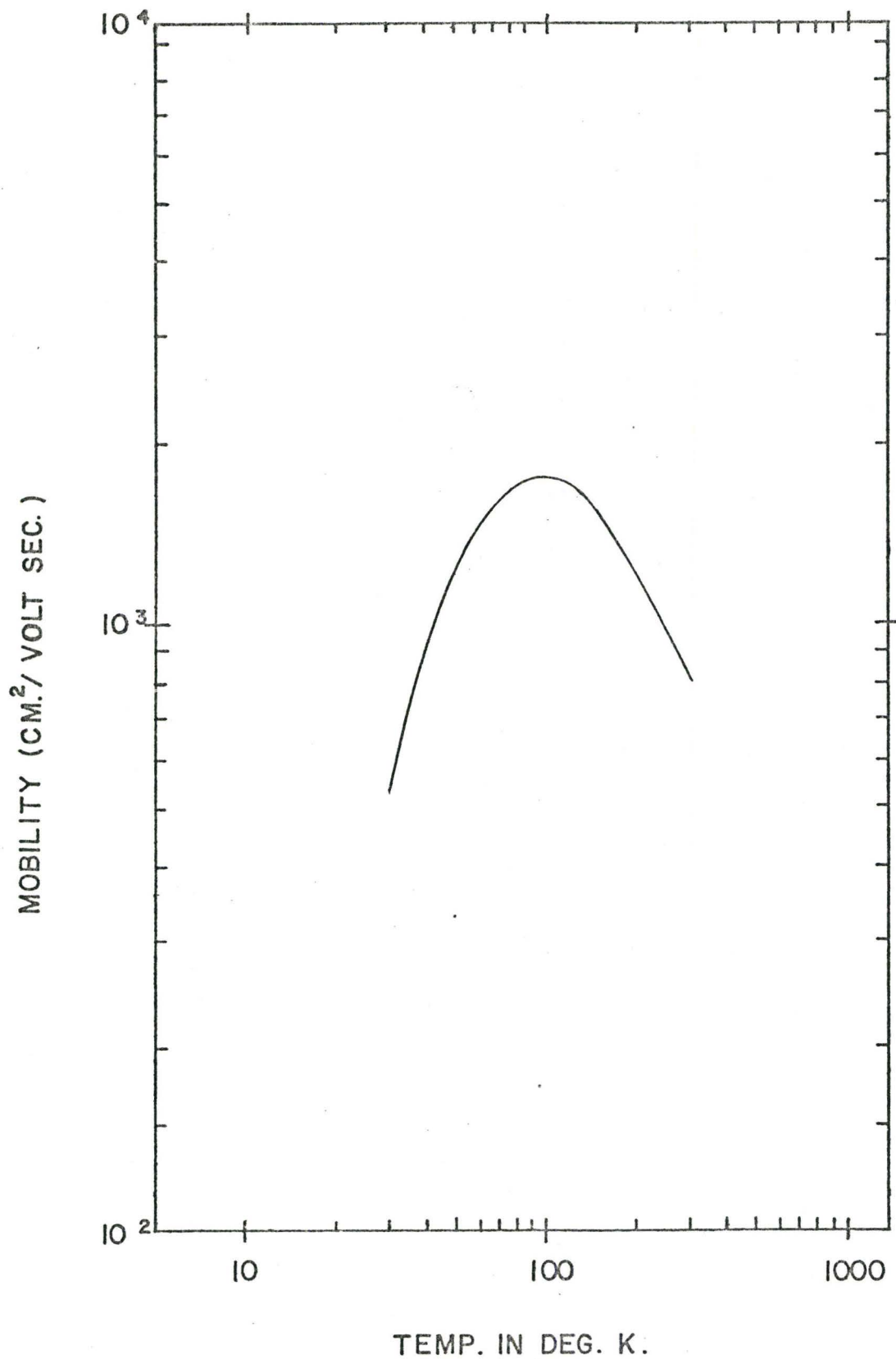
Figure (4-9 d). Mobility vs. (1/T) graph of a silicon sample
(Si-146) implanted at $100^{\circ}K$ with 1.4×10^{14} N/cm^2,
80/40 keV.
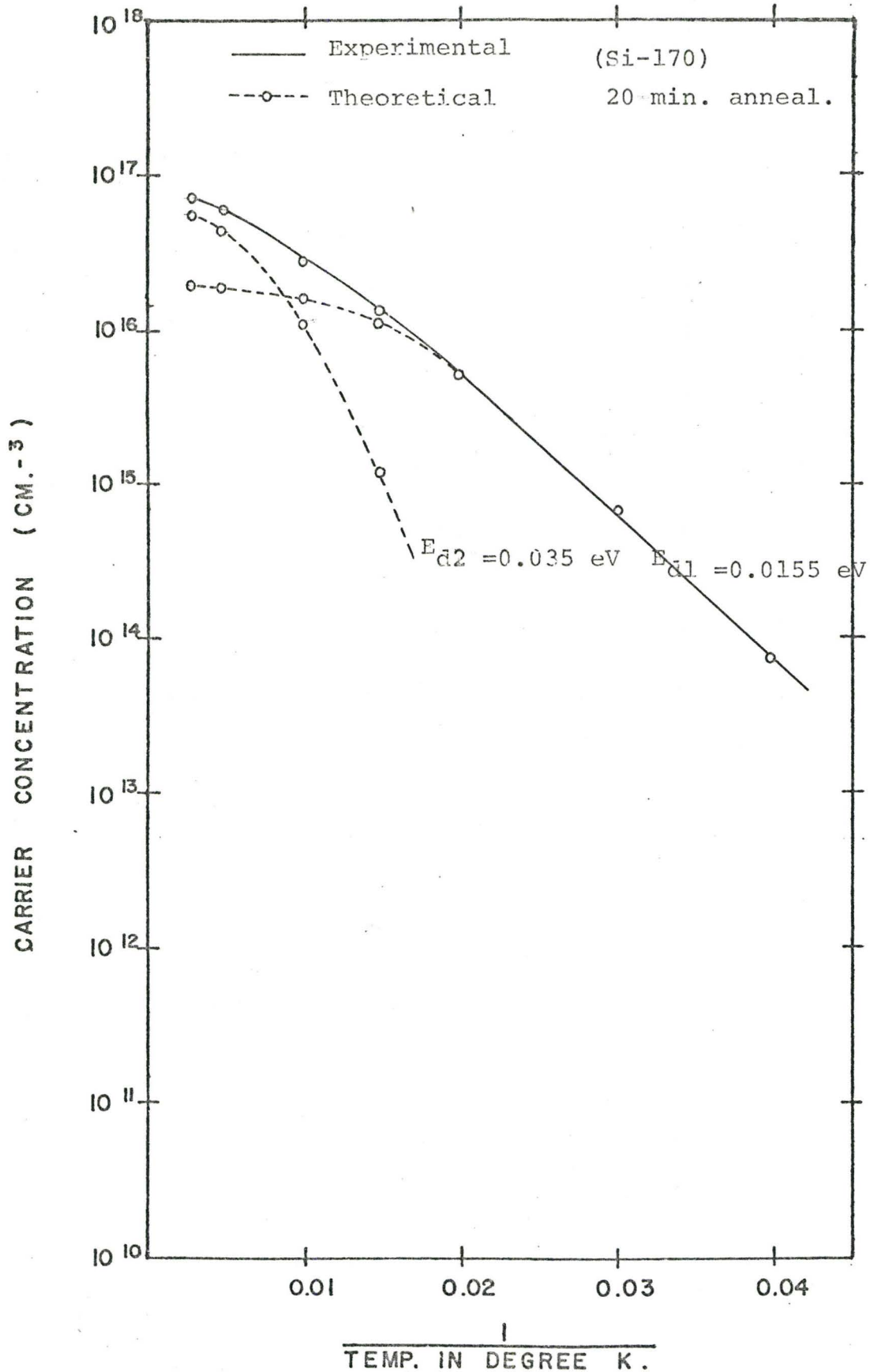
Figure (4-10 a)   Carrier concentration vs. (1/T) graphs of (Si-170) sample implanted at 100°K with 2.8×10^{14} N/cm^2, 80/40 keV.
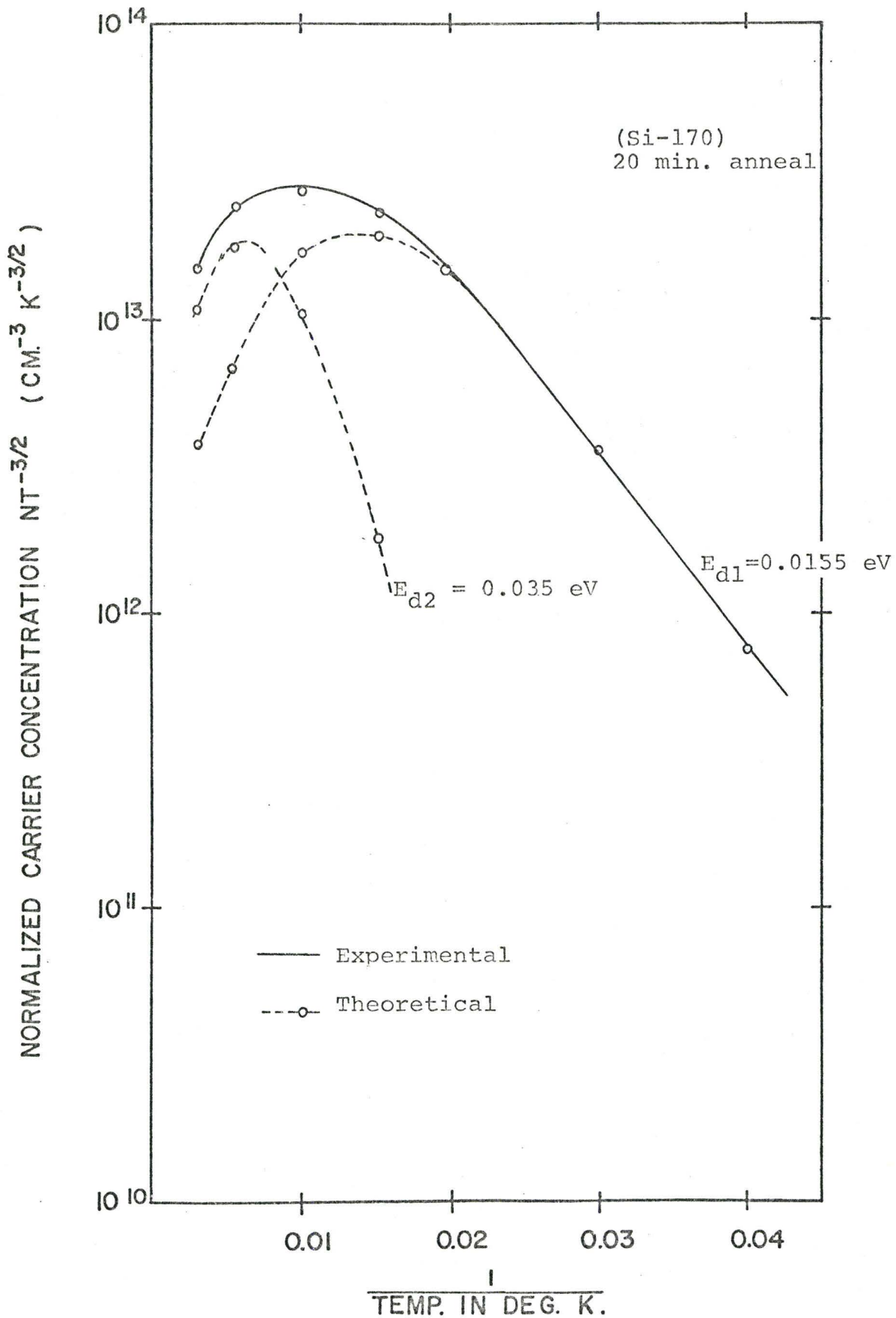
Figure (4-10 b)   Norm. carrier concentration vs. (1/T) graphs of (Si-170) sample implanted at 100°K with 2.8×10^{14} N/cm^2, 80/40 keV.
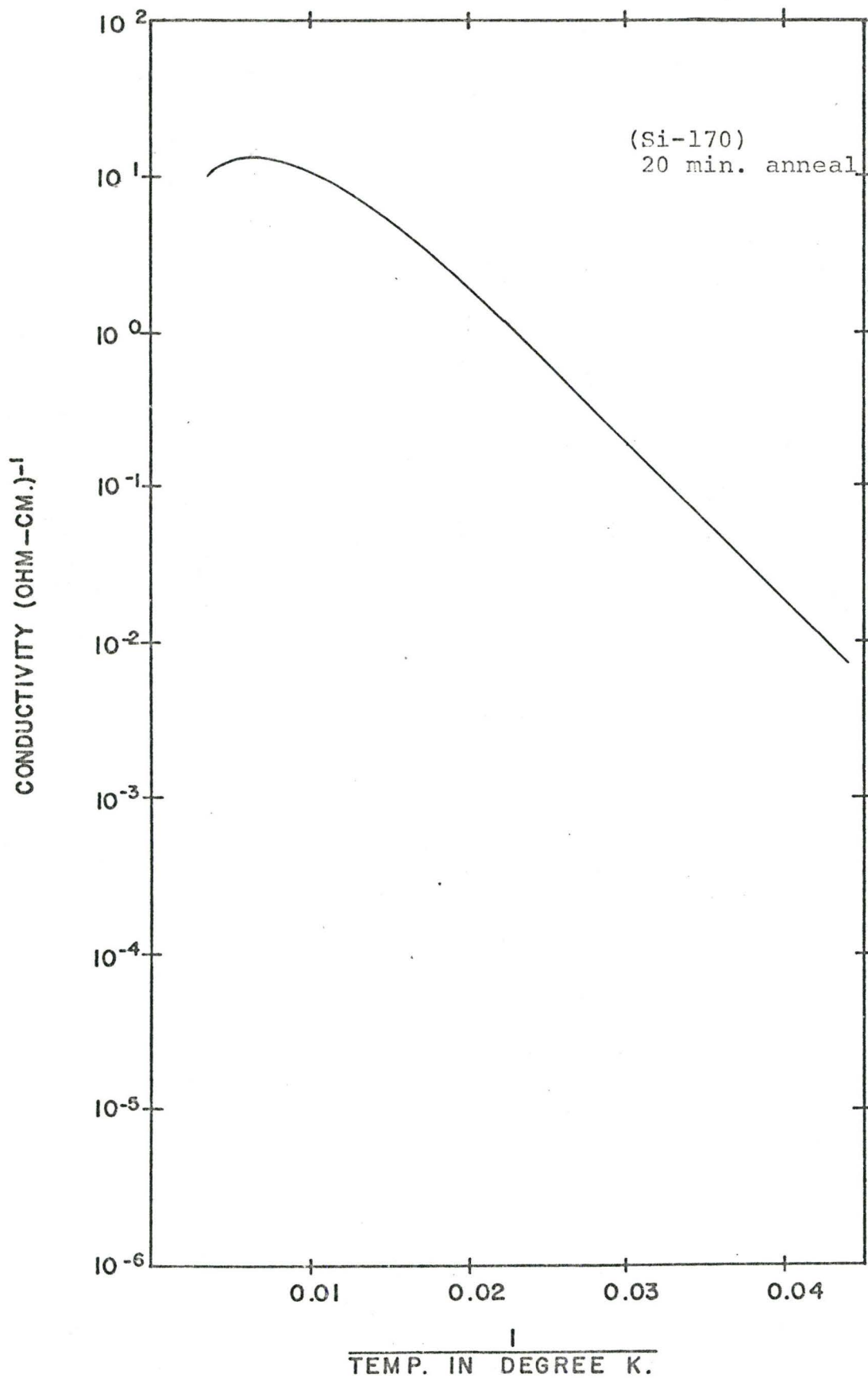
Figure (4-10 c)   Conductivity vs. (1/T) graph of (Si-170) sample implanted at $100^{\circ}K$ with 2.8×10^{14} N/cm^2, 80/40 keV.
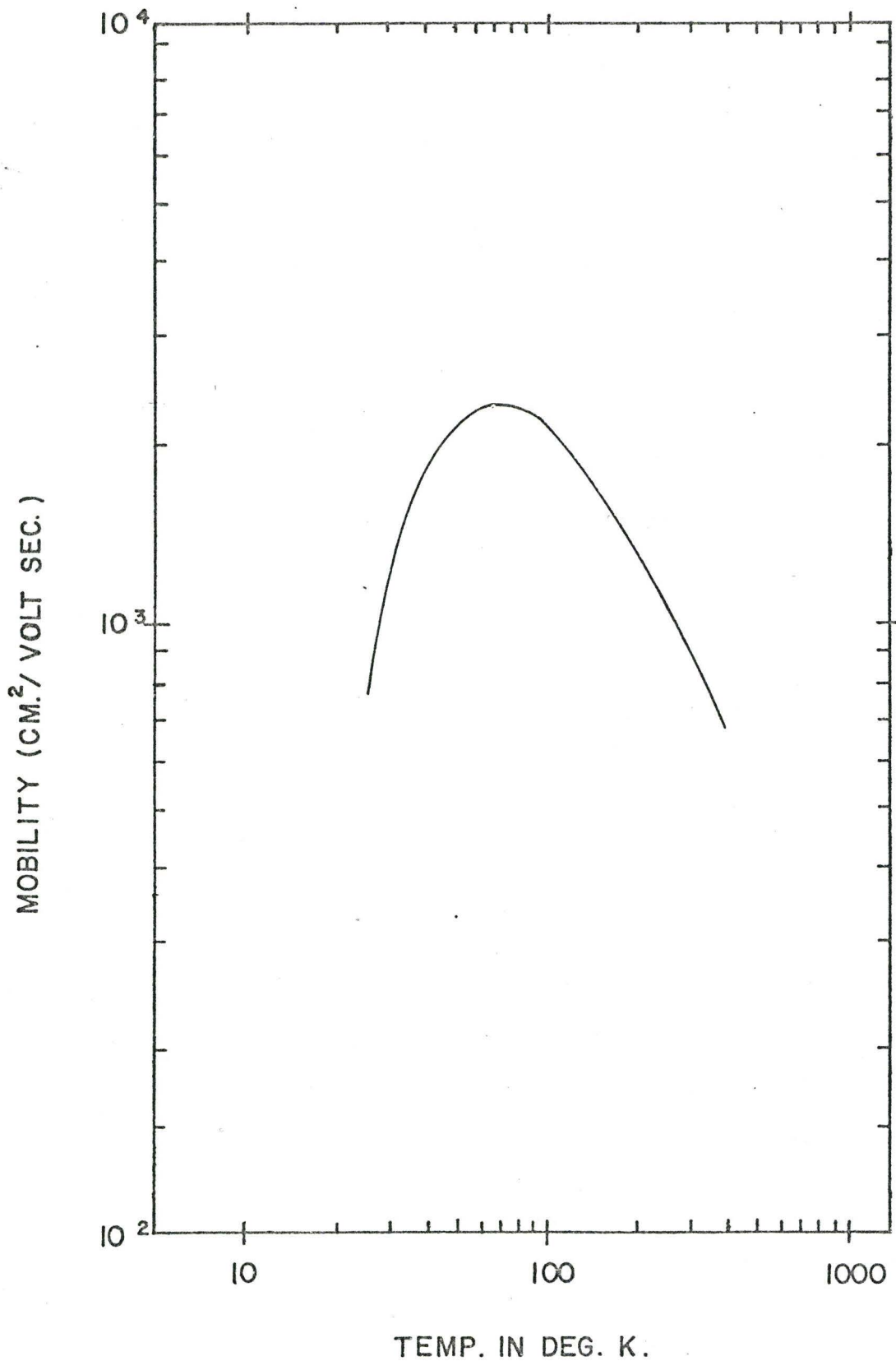
Figure (4-10 d) Mobility vs. (1/T) graph of (Si-170) sample
implanted at 100° K with 2.8×10^{14} N/cm^2,
80/40 keV.
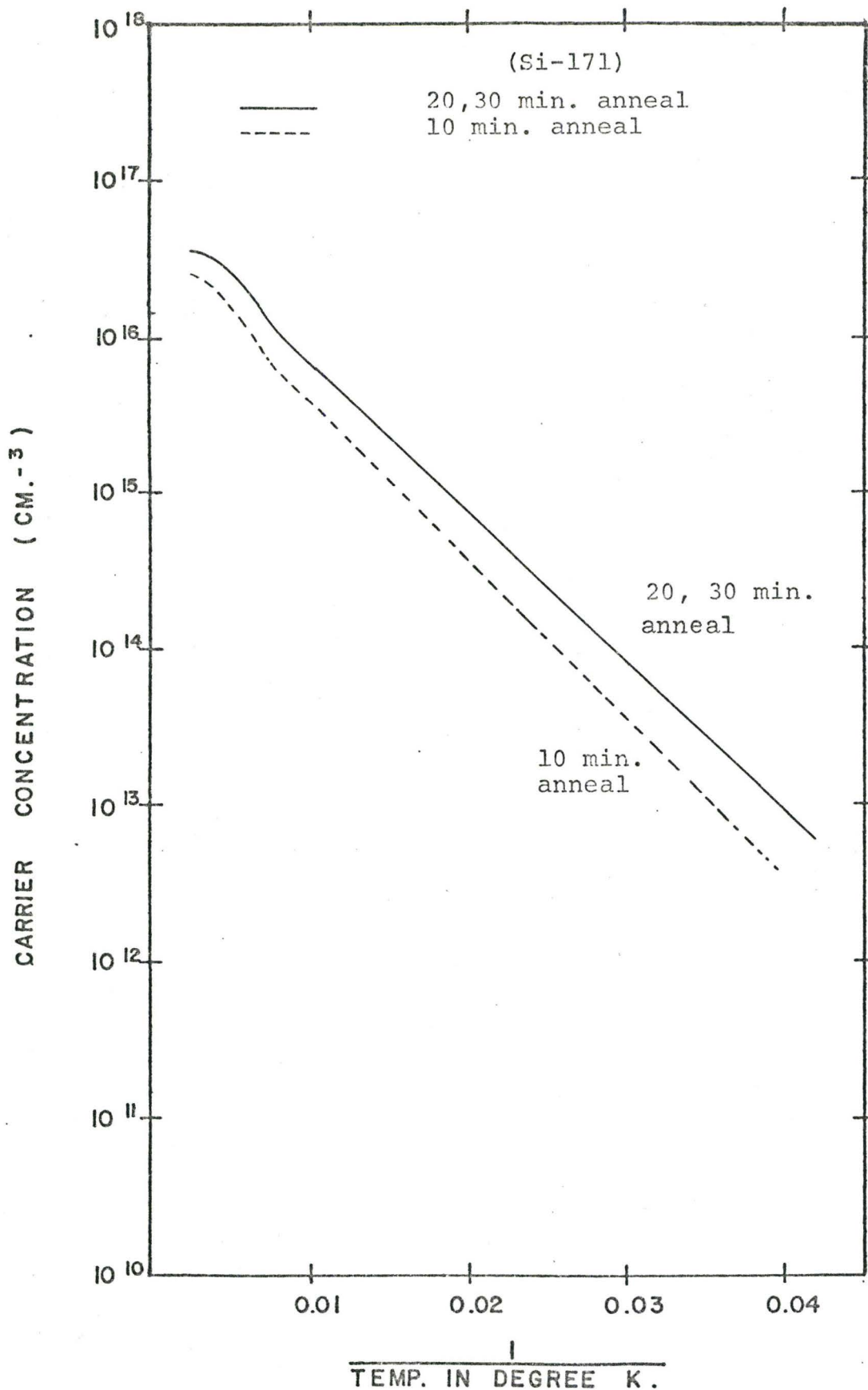
Figure (4-11 a). Carrier concentration vs. (1/T) graphs of
sample (Si-171) implanted at 100°K with
1.4×10^{14} N/cm^2, 80/40 keV.
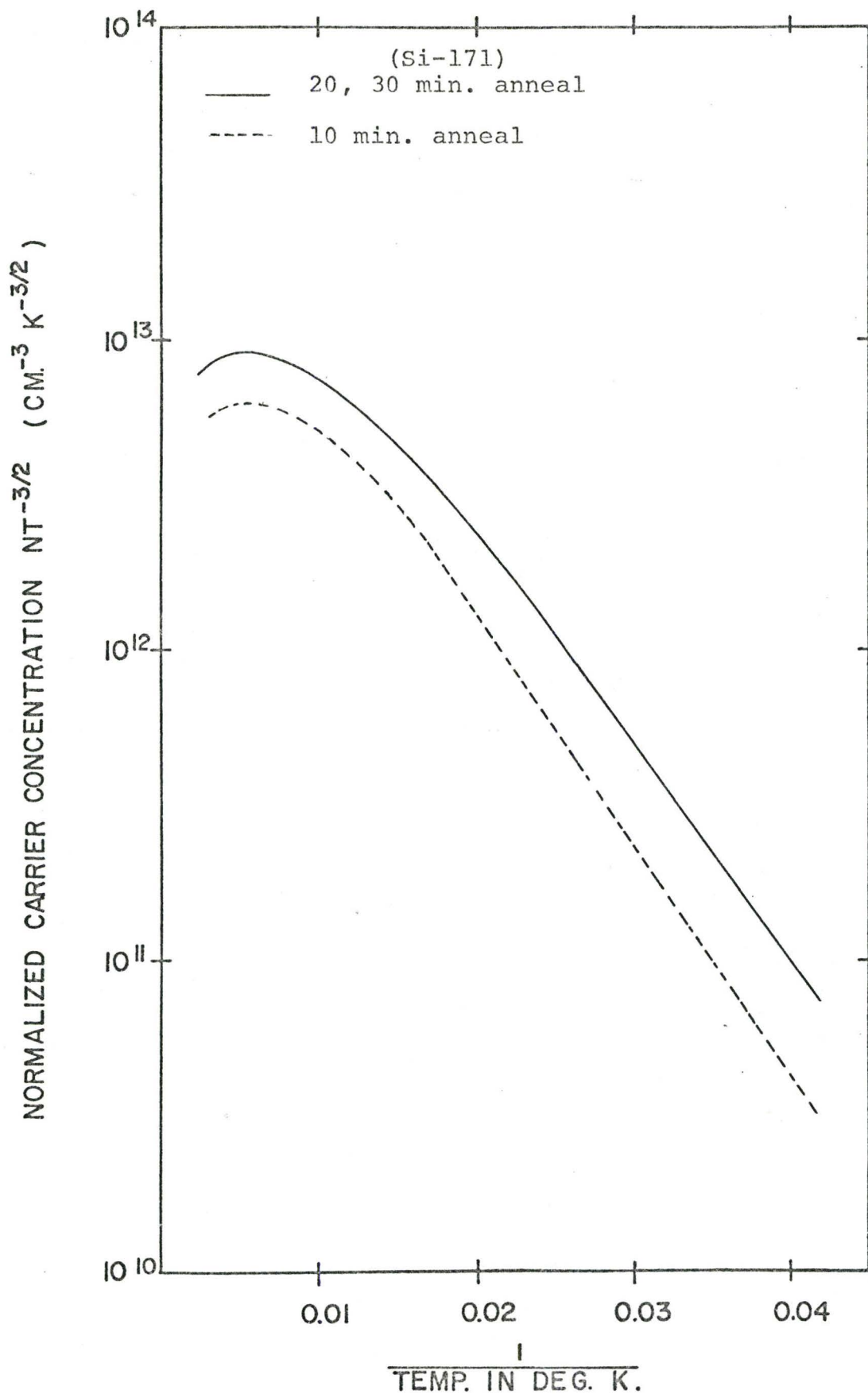
Figure (4-11 b.) Normalized carrier concentration vs. (1/T) graphs of sample (Si-171) implanted at 100° K with 1.4×10^{14} N/cm^2, 80/40 keV.
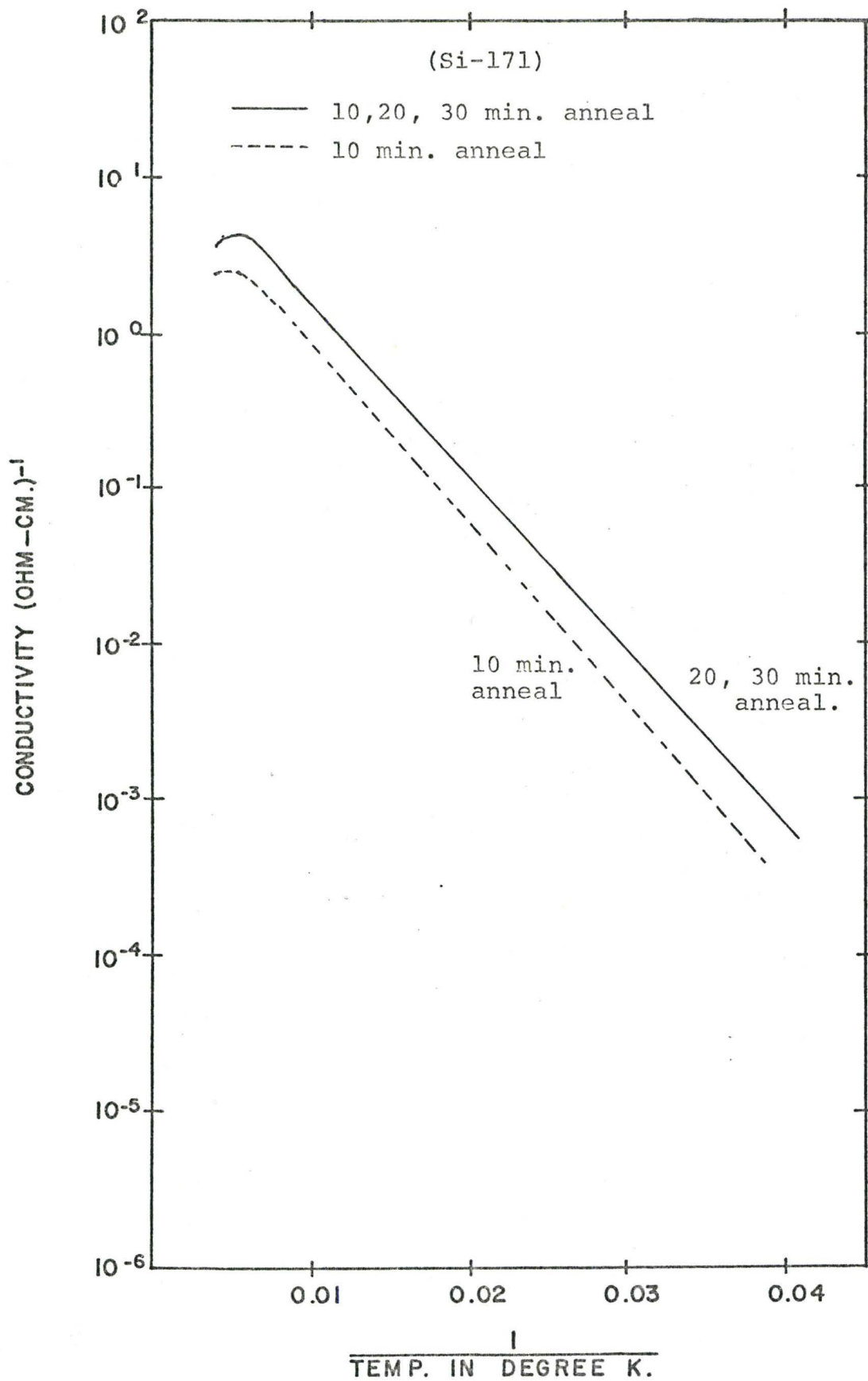
Figure (4-11 c). Conductivity vs. (1/T) graphs of sample
(Si-171) implanted at $100^{\circ}K$ with 1.4×10^{14} N/cm^2,
80/40 keV.
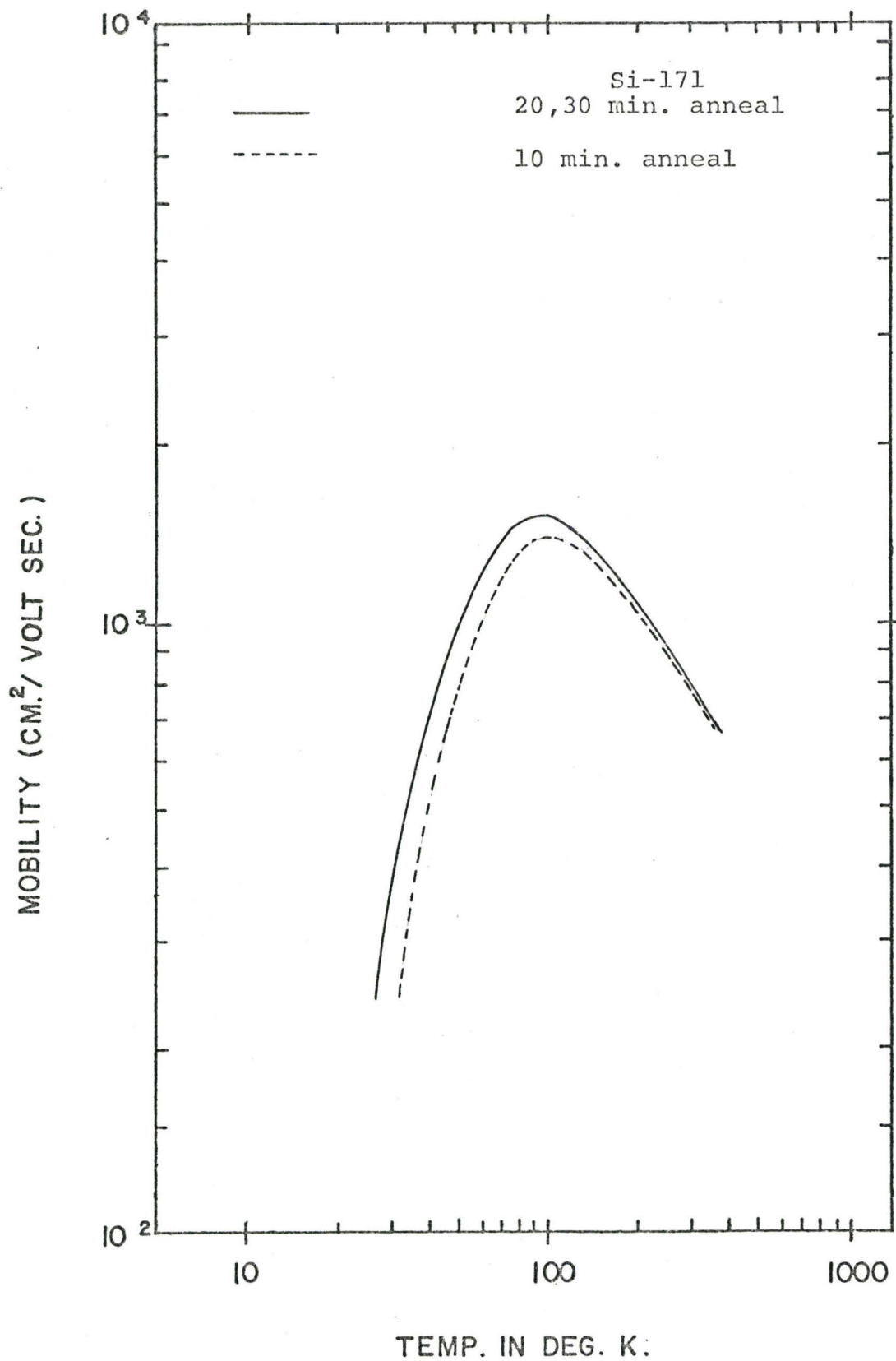
Figure (4-11 d). Mobility vs. (1/T) graphs of sample (Si-171) implanted at 100°K with 1.4×10^{14} N/cm^2, 80/40 keV.
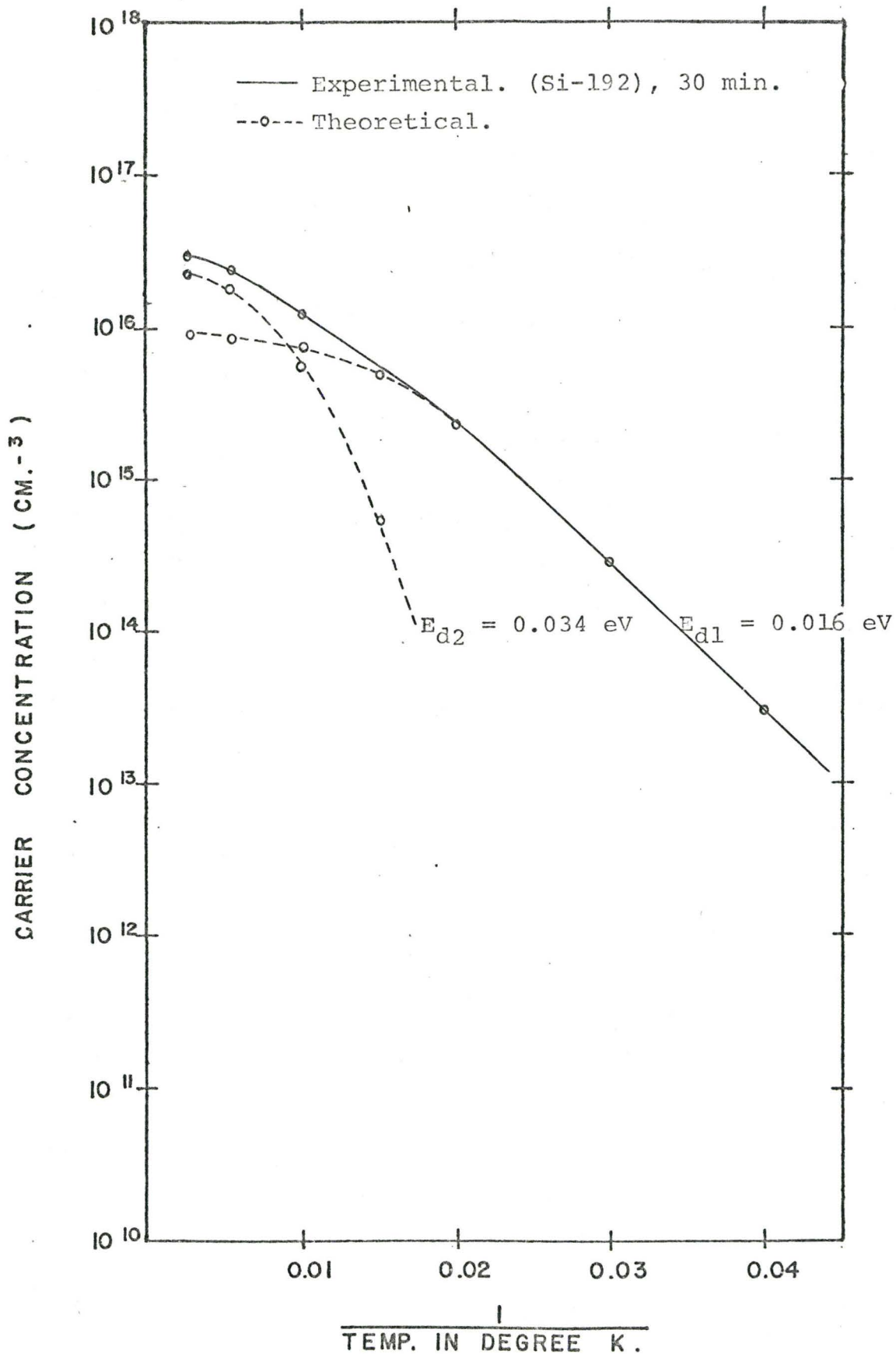
Figure (4-12 a). Carrier concentration vs. (1/T) graphs of sample (Si-192) implanted at 300°K with 1.4 x 10^{14} N/cm^2, 80/40 keV.
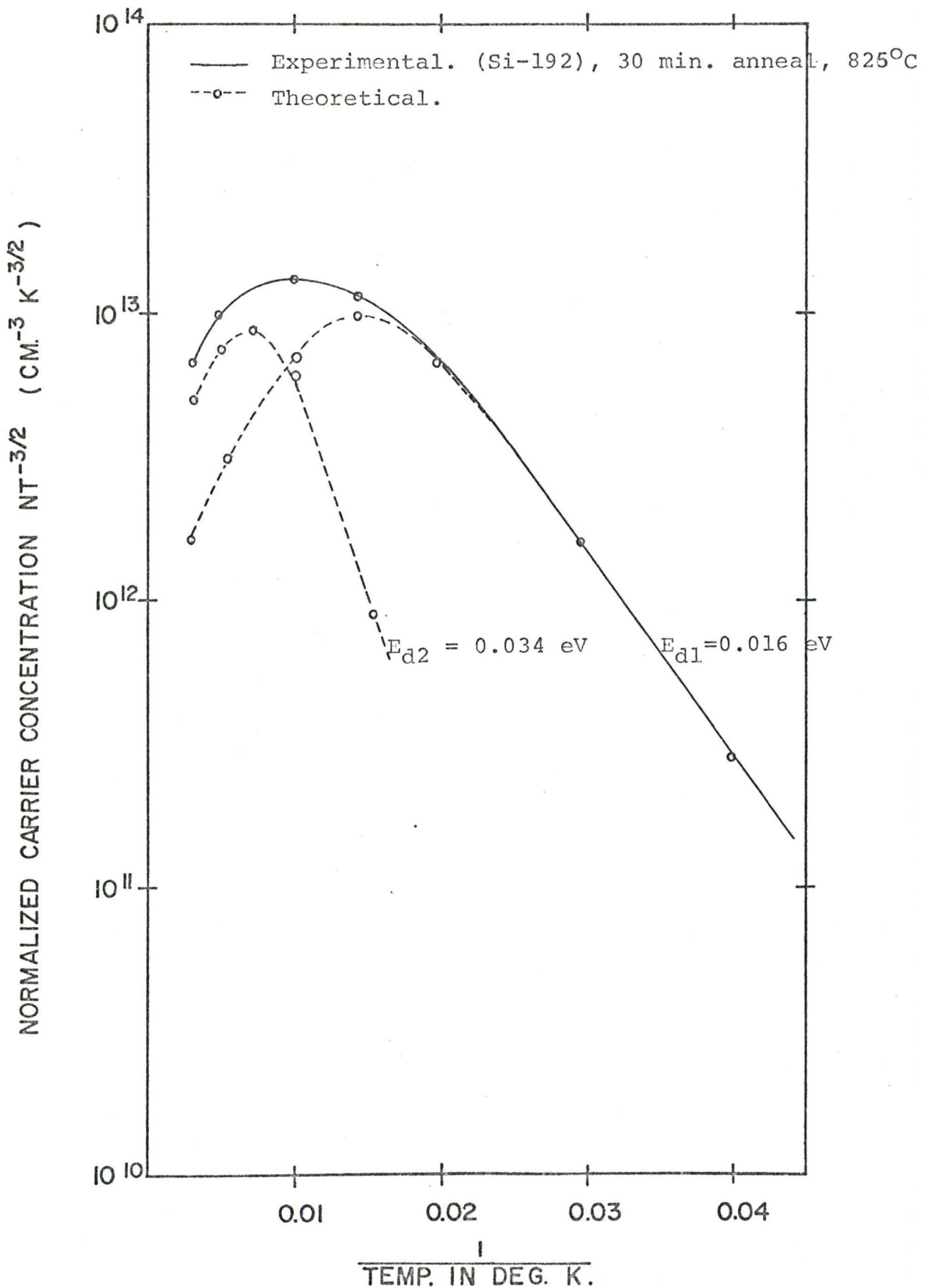
Figure (4-12 b). Normalized carrier concentration vs. (1/T)
graphs of sample (Si-192) implanted at 300° K
with 1.4×10^{14} N/cm2, 80/40 keV.
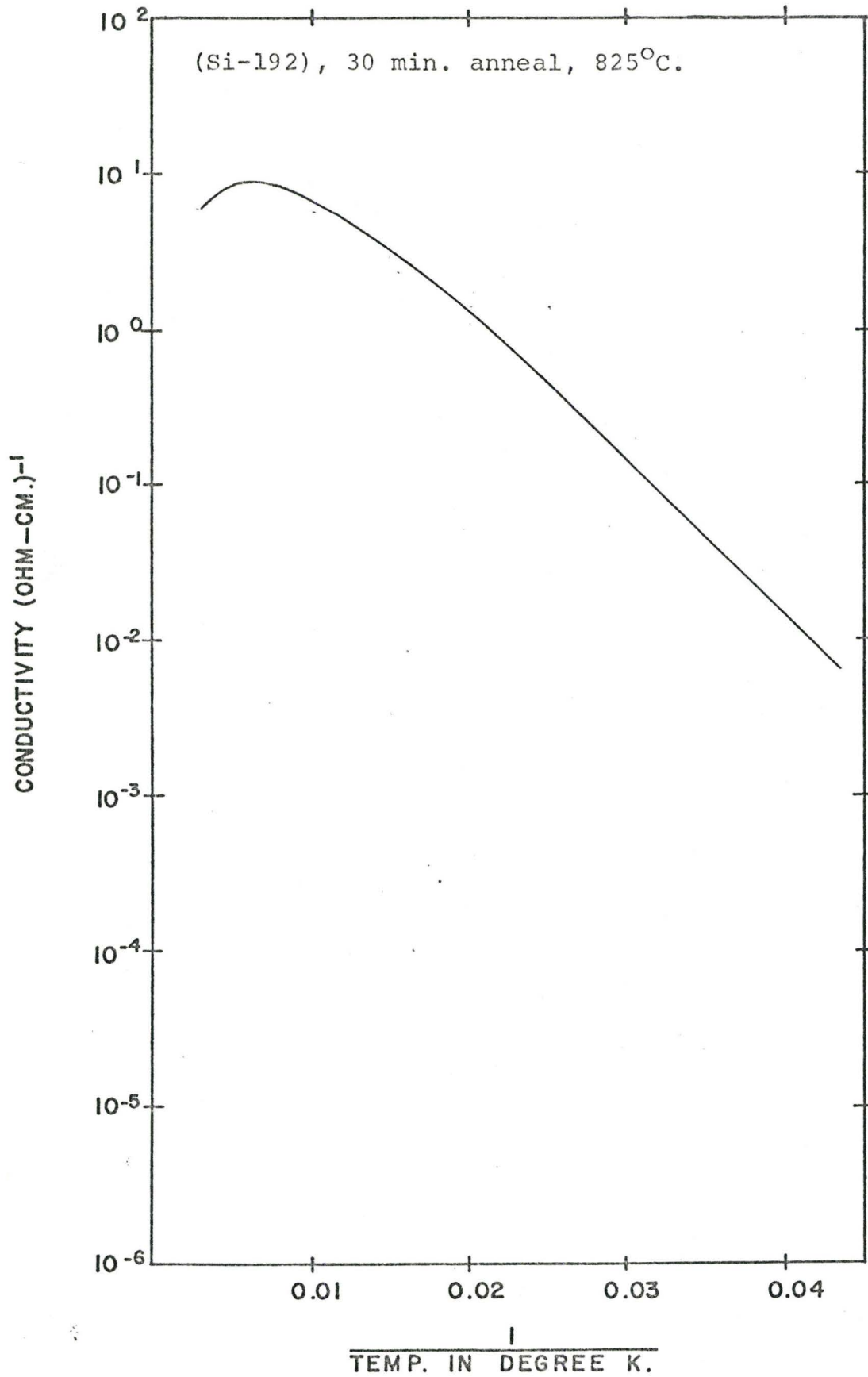
Figure (4-12 c). Conductivity vs. (1/T) graph of sample
(Si-192) implanted at 300^OK with 1.4×10^{14} N/cm^2,
80/40 keV.
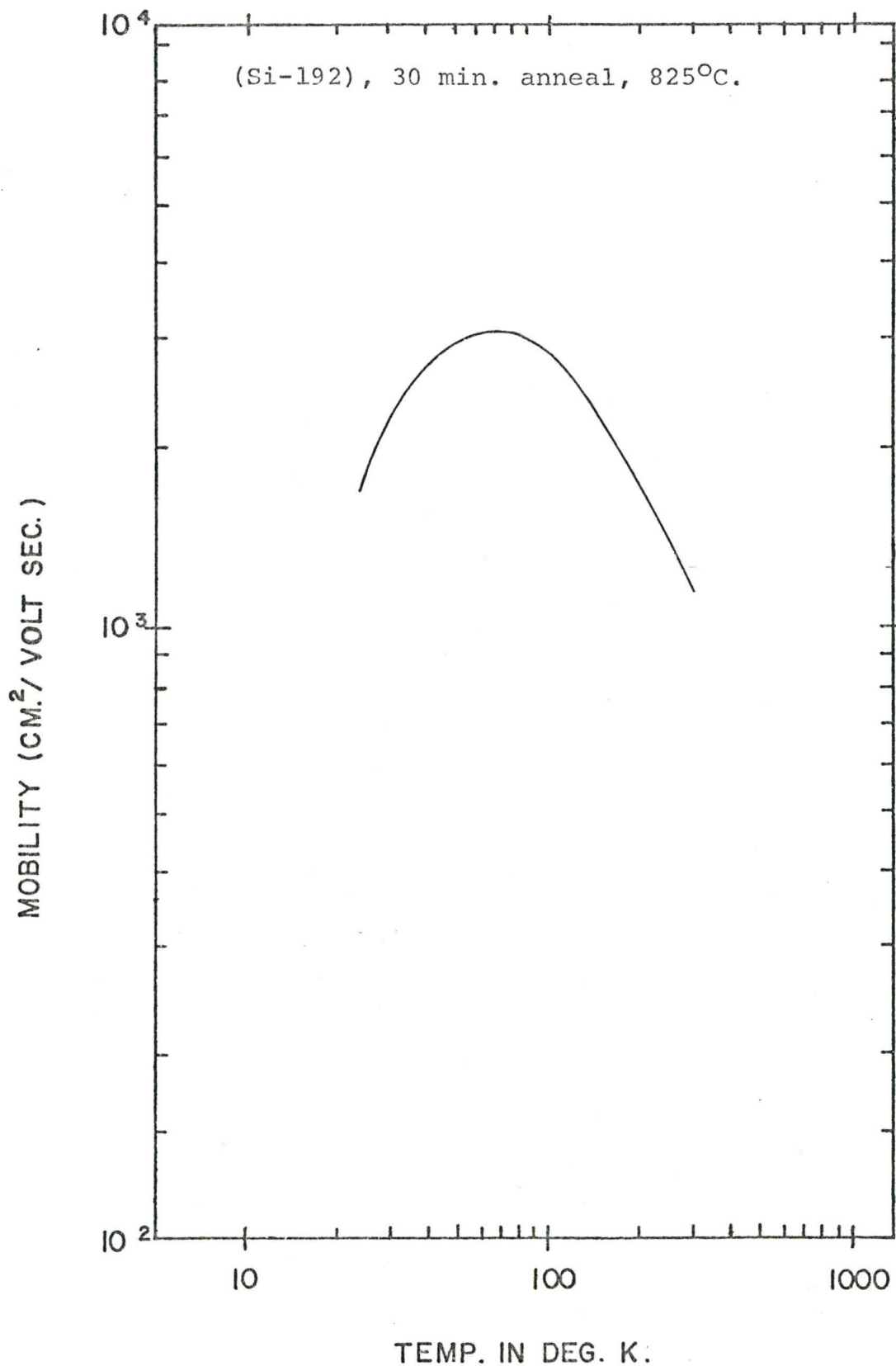
Figure (4-12 d). Mobility vs. (1/T) graph of sample (Si-192) implanted at 300^OK with 1.4×10^{14}N/cm^2, 80 / 40 keV.
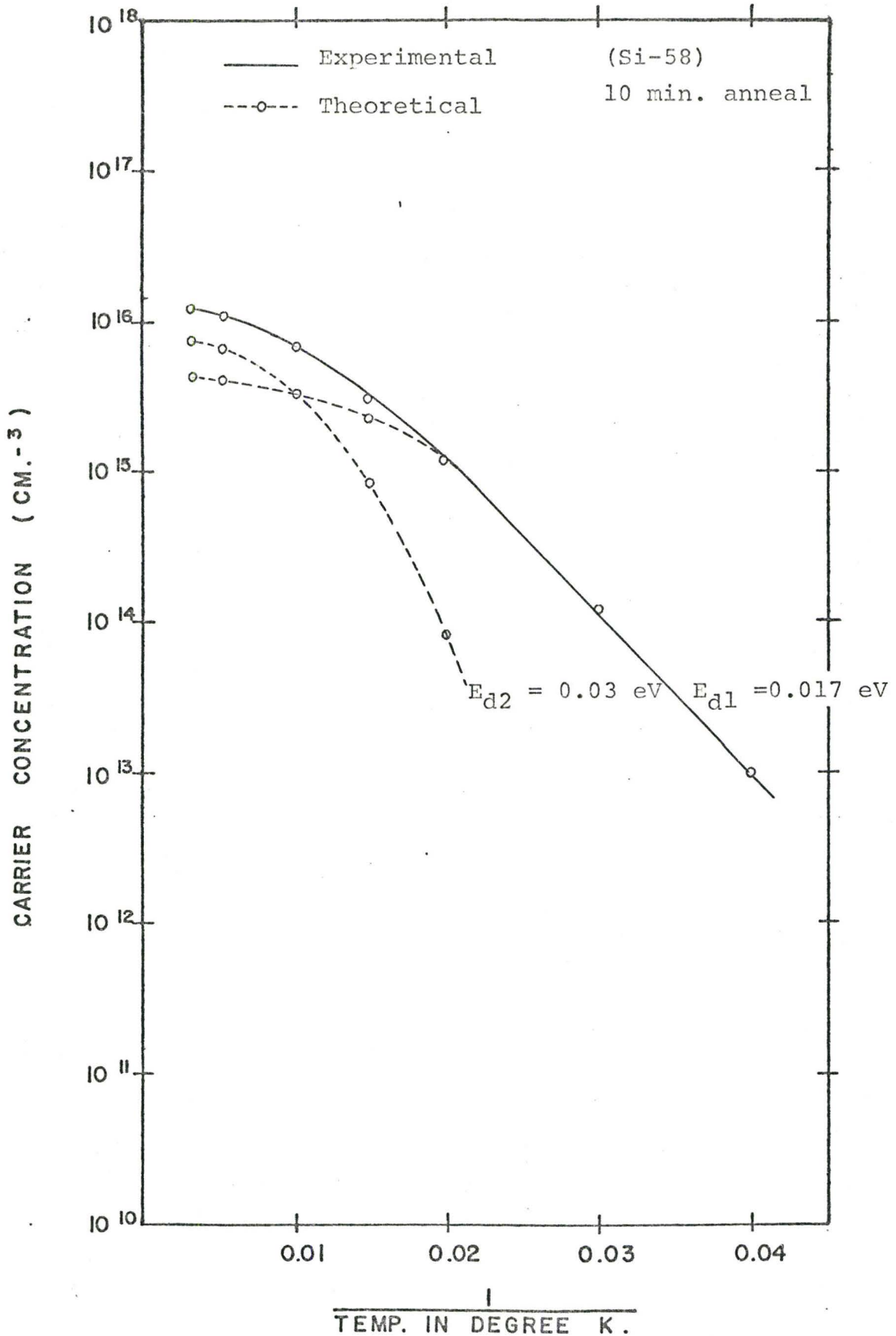
Figure (4-13 a) Carrier concentration vs. (1/T) graphs of sample (Si-58) implanted at 300°K with 8 x 10¹⁴ N/cm², 80/40 keV.
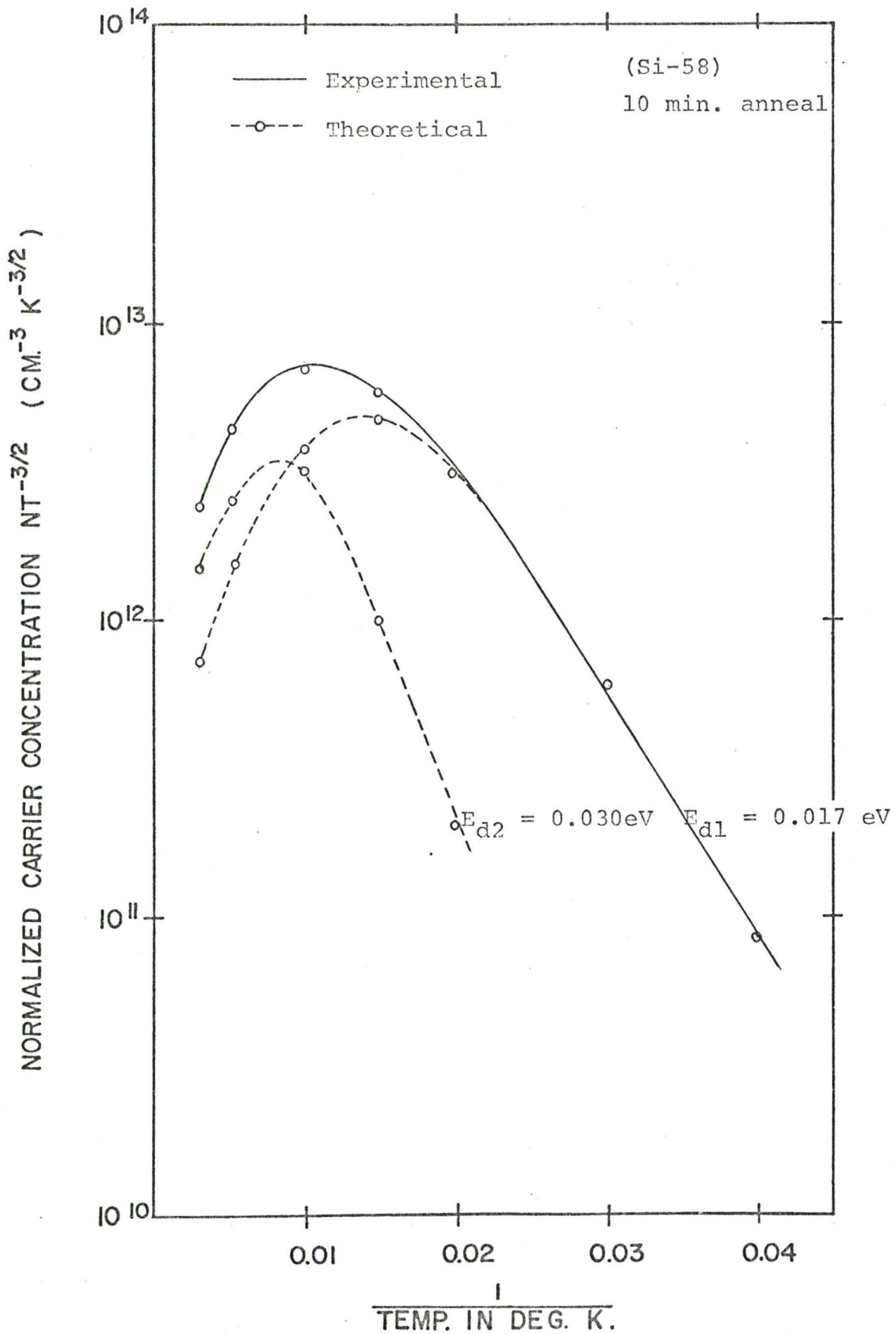
Figure (4-13 b)   Norm. carrier concentration vs. (1/T) graphs
of sample (Si-58) implanted at 300°K with
8×10^{14} N/cm^2, 80/40 keV.
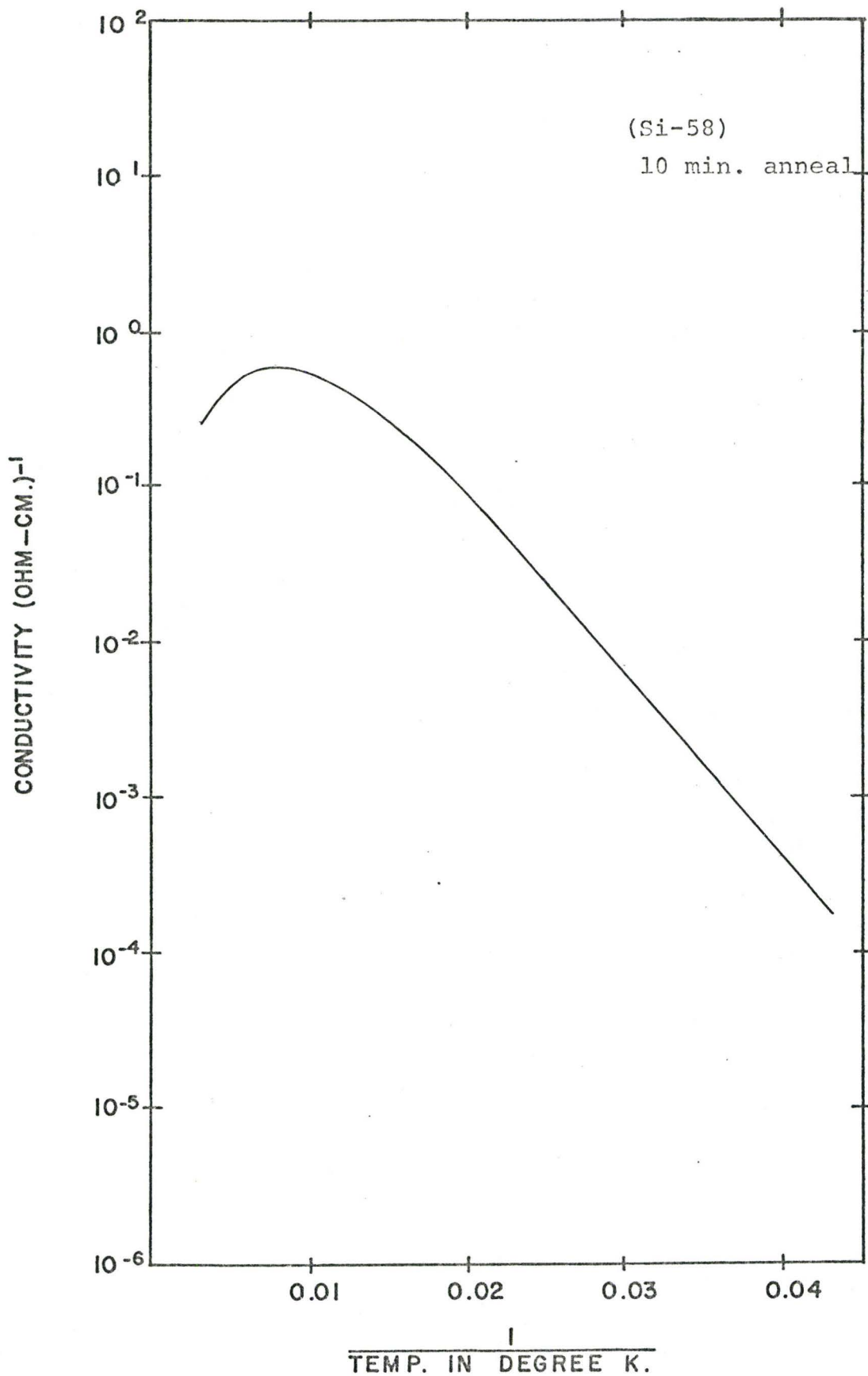
Figure (4-13 c) Conductivity vs. (1/T) graph of sample (Si-58) implanted at 300°K with 8×10^{14} N/cm^2, 80/40 keV.
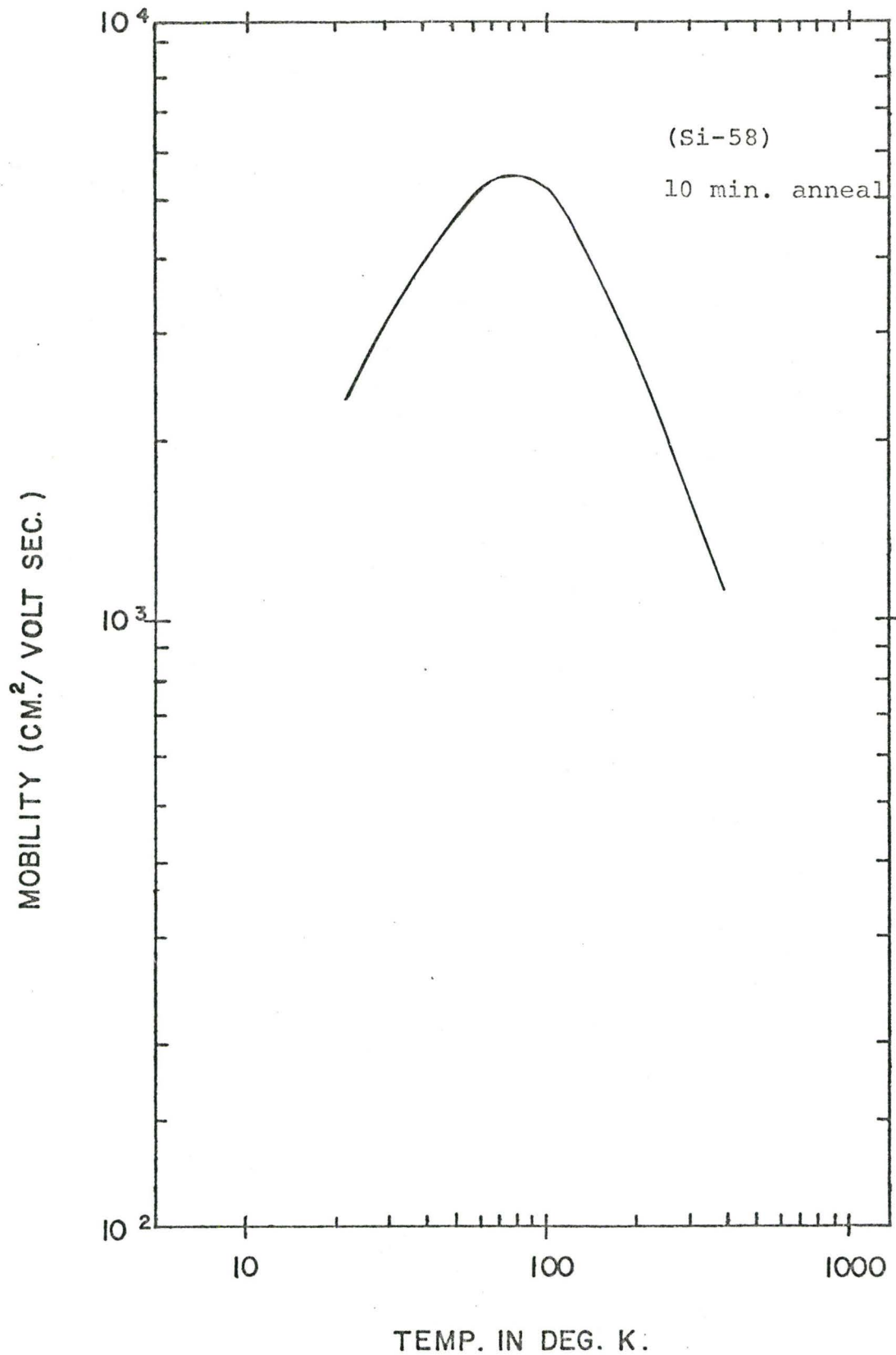
Figure (4-13 d). Mobility vs. (1/T) graph of sample (Si-58) implanted at $300°K$ with 8×10^{14} N/cm^2, 80/40 keV.
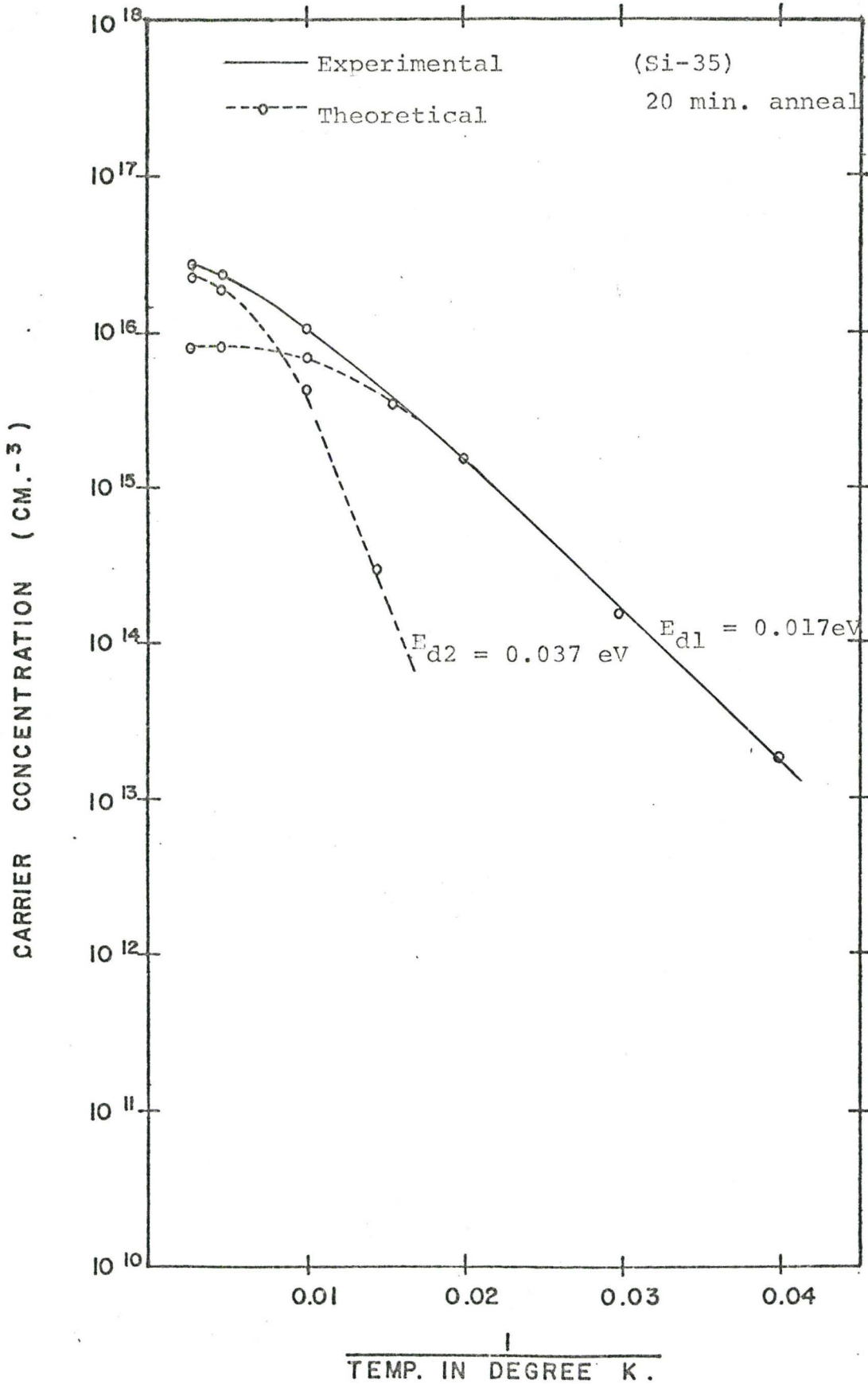
Figure (4-14 a). Carrier concentration vs. (1/T) graphs of sample (Si-35) implanted at 300°K with 1.4×10^{14} N/cm^2, 50 keV.
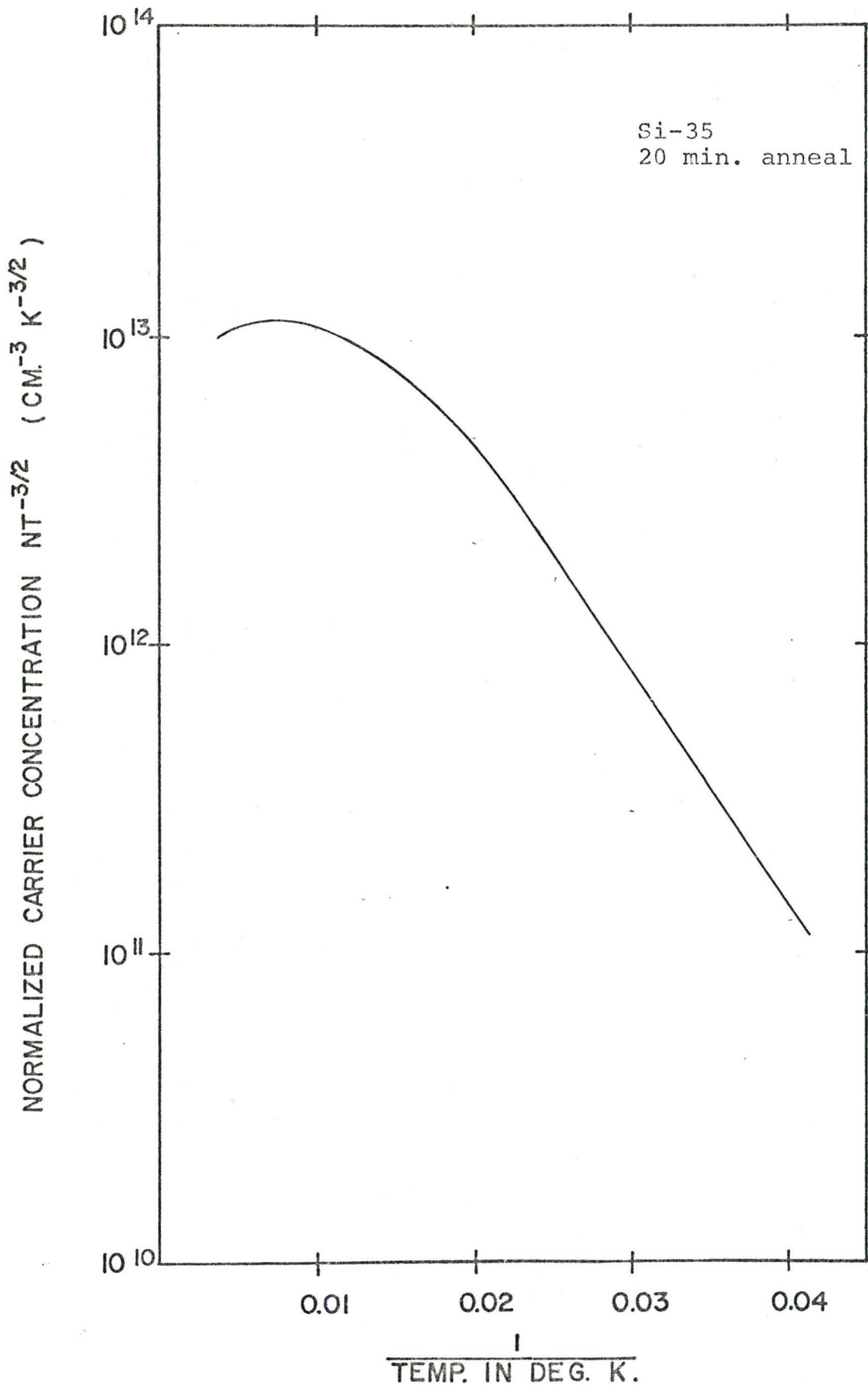
Figure (4-14 b)   Norm. carrier concentration vs. (1/T) graph
of sample (Si-35) implanted at 300°K with
1.4×10^{14} N/cm^2, 50 keV.
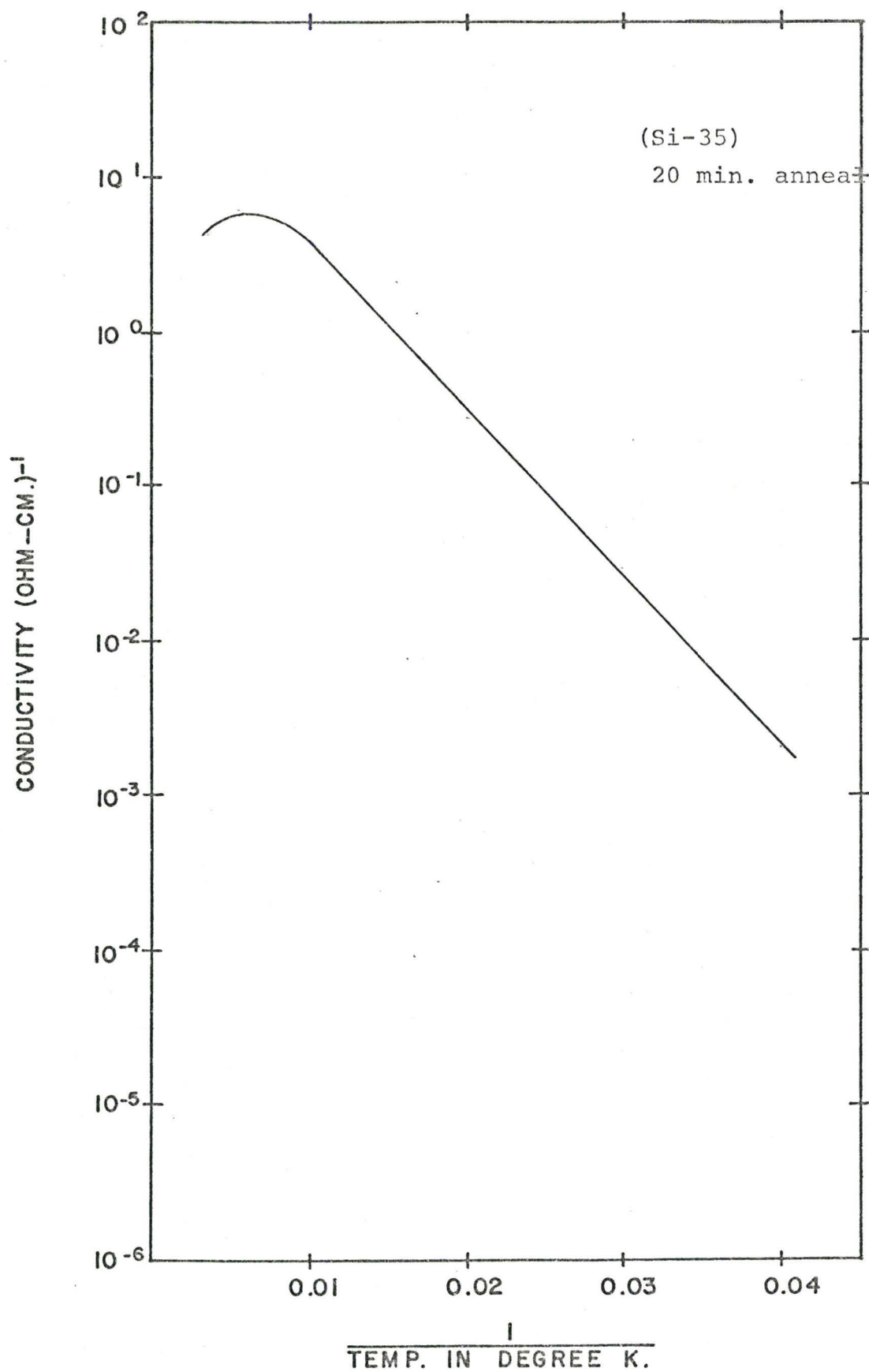
Figure (4-14 c) Conductivity vs. (1/T) graph of sample (Si-35) implanted at 300°K with 1.4 x 10^{14} N/cm^2, 50 keV.
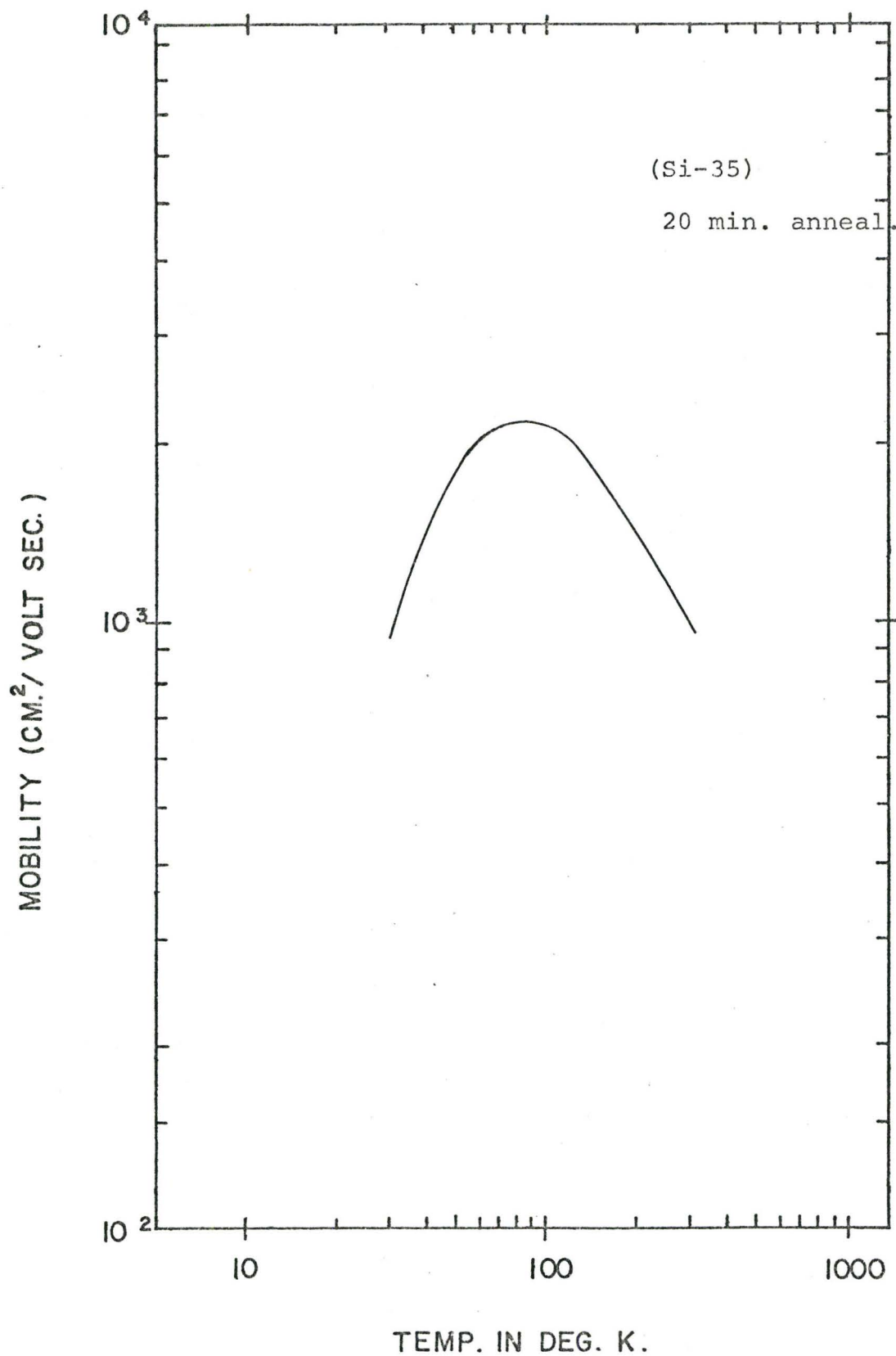
Figure (4-14 d). Mobility vs. (1/T) graph of sample (Si-35)
implanted at 300° K with 1.4×10^{14} N/cm^2, 50 keV.

4.2.3. Analysis

The model of a n-type semiconductor containing two monovalent donors at different energies and assorted low lying compensating acceptor centers [12] were applied. The model is shown in Figure (4-15). N_{d1} and N_{d2} donor densities were assumed to be on the E_{d1} and E_{d2} donor levels respectively, while the compensating acceptor density was assumed to be N_a. Therefore, only $(N_{d1} + N_{d2} - N_a)$ electrons remain for distribution between the two sets of donors and the conduction band.

Two different forms of behaviour could exist dependent upon whether $N_a > N_{d1}$ or $N_a < N_{d1}$. If $N_a > N_{d1}$, then the upper donor level will be completely free from electrons at $0\,^oK$ and the Fermi level will be locked to the energy $(E_c - E_{d2})$. By raising the temperature the Fermi level will decrease several kT under $(E_c - E_{d2})$ and the number of free carriers in the conduction band will increase. At a sufficient high temperature $(300\,^oK)$, the number of electrons in the conduction band reaches its limiting value $(N_{d1} + N_{d2} - N_a)$.

If $N_a < N_{d1}$, (which is the case in our experiments too) at $0\,^oK$ temperature the Fermi level coincides with the energy $(E_c - E_{d1})$, the lower donor level will be completely full and the upper one will contain
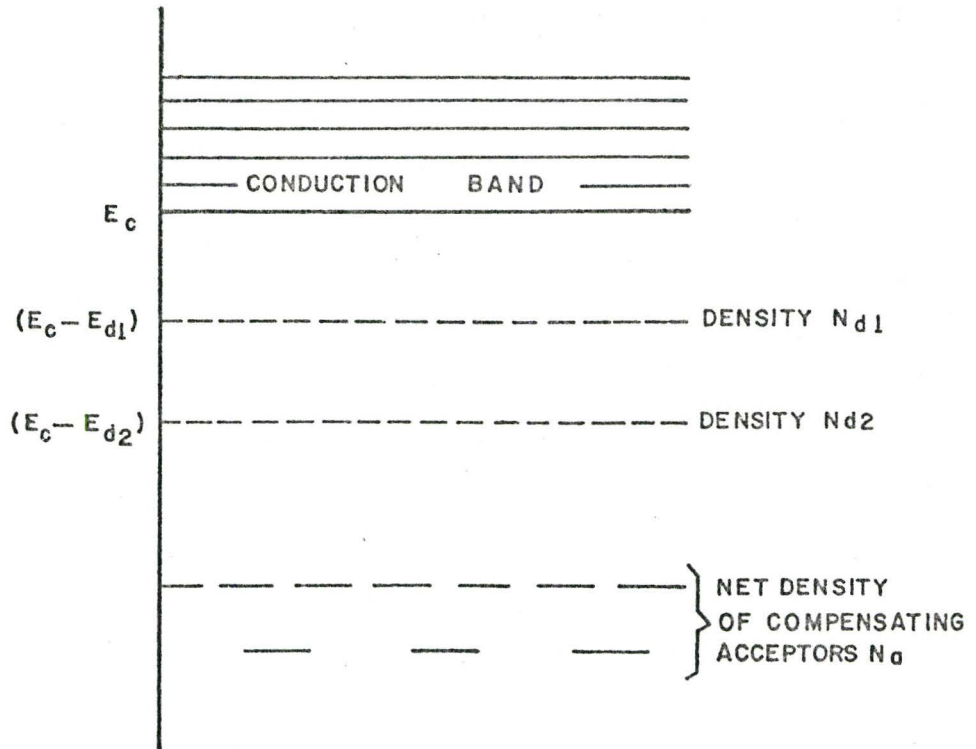
Figure (4 - 15). The model of a partially compensated n-type semiconductor containing two monovalent kinds of donors with different activation energies.

N_{d1} - N_{d2} electrons. When the temperature rises the
upper donors offer their electrons to the conduction
band, and the Fermi level moves below (E_c - E_{d1}) as
this level becomes exhausted. On further warming, no
appreciable increase of the number of free electrons in
the conduction band (n_o) is possible until the Fermi
level drops close to the energy (E_c - E_{d2}); and then the
second set of donors begins to lose electrons. At suffi-
ciently high temperatures n_o levels off to the value
of $(N_{d1} + N_{d2} - N_a)$ while the Fermi level (ϕ) drops
in accordance with Equation (4.8).

$$\phi = E_c - kT \times \ln \left(\frac{N_c}{N_{d1} + N_{d2} - N_a} \right) \qquad (4.8)$$

If the two donor energy levels are relatively far from
each other (several kT), it is possible that the first
donor level supply could became totally exhausted before
the second donor level will contribute substantially in
the conduction process. In this case a distinct step to
the carrier concentration versus 1/T curve could be
expected, as it is shown in Figure (4-16) .
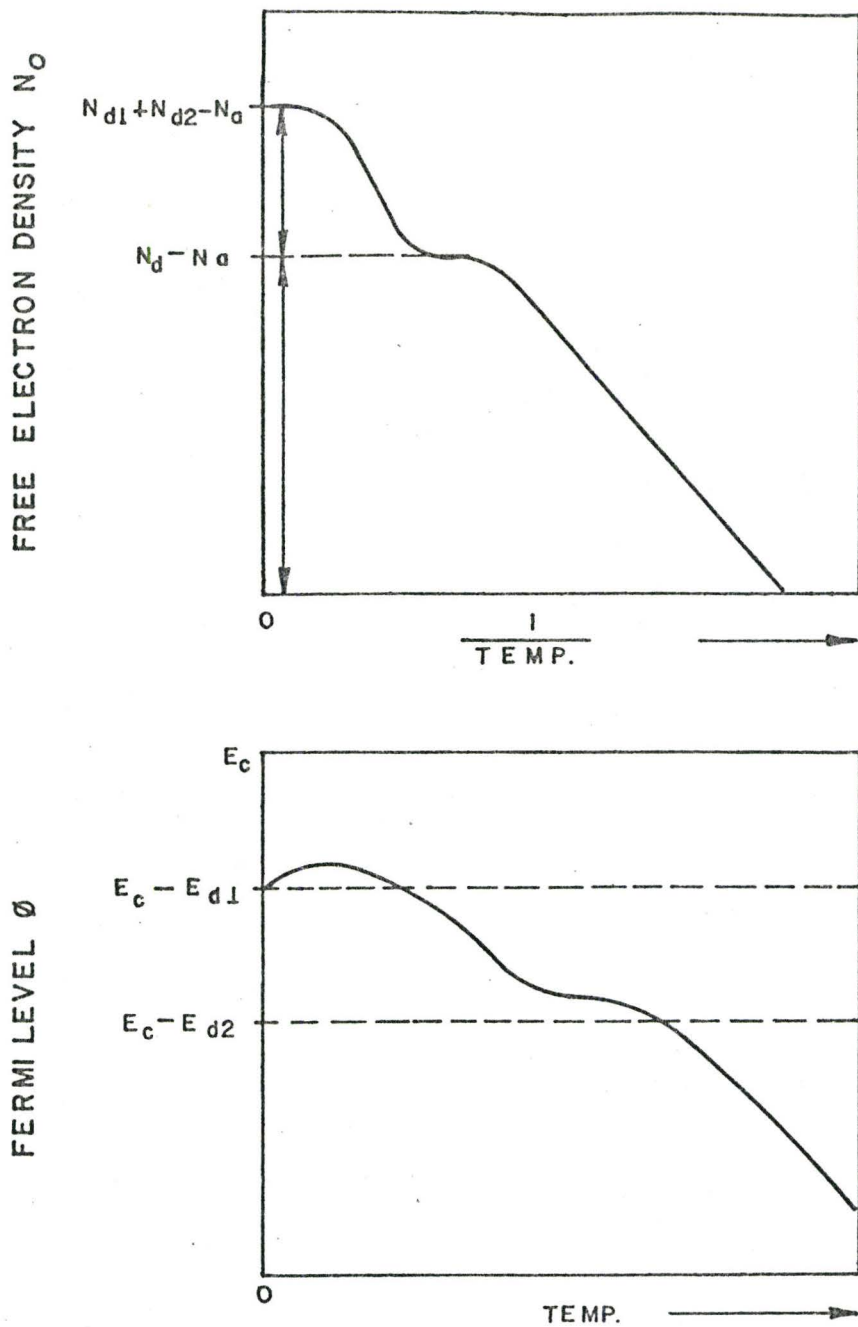
Figure (4 - 16). The carrier density vs. (1/T) and the Fermi-level vs. (1/T) when $N_A < N_{D1}$ of a n-type partially compensated semiconductor model having two monovalent kinds of donors.

If the donor energy levels are not too far apart, the concentration curve rises rather smoothly to the saturation value of $N_{d1} + N_{d2} - N_a$. In other words the ionization of the first donor level is incomplete before the effect of the second level ionization shows up, as it is illustrated in Figure (4-17). This kind of properties were found in the experimental carrier concentration vs 1/T curves of the nitrogen ion implanted samples. The above behaviour was expressed in mathematical form by Ref.(12). Generally, M species of monovalent donor impurities were considered. The N_{dj} density with the corresponding binding energy E_{dj} was designated to the jth class. Then the number of ionized donors could be written in the following form :

$$N_{dj} \text{ (ion) } = \frac{N_{dj}}{1 + g_{dj}^{-1} \exp (\in_{dj} + \eta)} \tag{4.9}$$

where the possible influence of excited states are neglected. $g_{dj} = 2$; degeneracy factor of the jth class,

$$\in_{dj} = \frac{E_{dj}}{kT} \qquad ; \qquad \eta = \frac{\phi - E_c}{kT}$$

The sum of all ionized donors can be expressed as in Equation (4.10) .
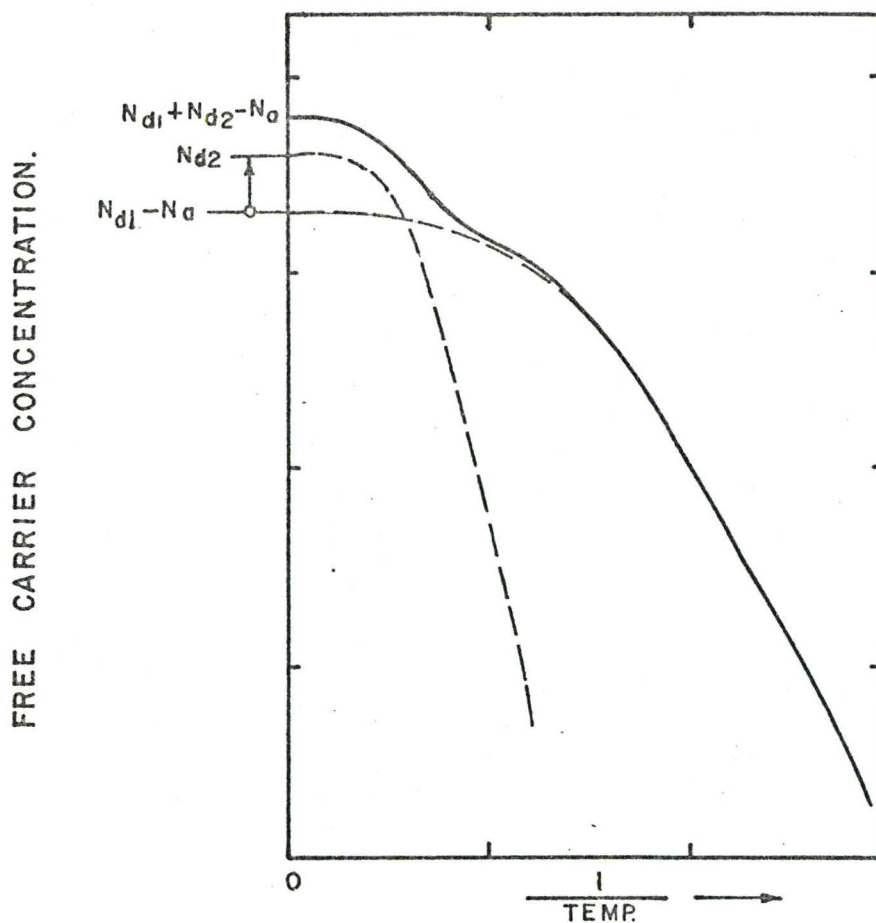
Figure (4-17). Free carrier concentration vs. (1/T) function of a partially compensated n-type semiconductor model having two monovalent types of donors. (E_{D1} and E_{D2} are relatively close to each other.)

$$n_o + N_a = \sum_{j=1}^{M} \frac{N_{dj}}{1 + g_{dj} \exp (\in_{dj} + \eta)} \qquad (4.10)$$

where the condition is assumed to be not degenerate.
Since:

$$n_o = N_c \; F_{1/2}(\eta) = 2 \; K_d \; F_{1/2}(\eta)$$

than n_o can be expressed in the form of

$$n = \sum_{j=1}^{M=2} \left(\frac{K_{dj} + N_a}{2} \right) \left\{ \left[1 + \frac{4K_{dj} (N_{dj} - N_a)}{(K_{dj} + N_a)^2} \right]^{1/2} - 1 \right\} \qquad (4.11)$$

where:

$M = 2$, independent donor levels

$$K_{dj} = 2.7 \times 10^{15} \times T^{3/2} \exp (- \frac{E_{dj}}{kT}) \qquad (4.12)$$

N_{d1} = density of the donors on the first donor level.

N_{d2} = density of the donors on the second donor level.

N_a = compensating acceptor level.

To approximate the carrier concentration vs. 1/T
experimental curves the following method was used:

From the n vs. 1/T graph it could be determined that:

$$n \; (T = 300^{\circ}K) = N_{d1} + N_{d2} - N_a \qquad (4.13)$$

The E_{d1} activation energy of the N_{d1} impurities was determined from the gradient of the plot of normalized carrier concentration vs. 1/T at very low temperatures. From the shape of the curve N_{d1} as well as N_{d2} could be graphically approximated. Knowing N_{d1} the carrier concentration function $n_1(T)$ for the first energy level can be calculated. The ionization graph $n_2(T)$ of the second donor energy level can be derived from Equation (4.14.)

$$n_2(T) = n(T) - n_1(T) \qquad (4.14)$$

The ionization energy of the second donor level (E_{d2}) was obtained from the theoretical expression of $n_2(T)$. It must be emphasized that E_{d2} was determined relatively less accurately than E_{d1} because E_{d2} was obtained by fitting the $n_2(1/T)$ curve in the intermediate temperature range. The deviation of E_{d2} from its main value considering the results of all the samples is approximately twice of the deviation calculated for E_{d1}. The reason for this is that $n_2(T)$ can not be given very accurately in the very low temperature range from Equation (4.14)

because if T is very low, then $n_2(T) \ll n_1(T) = n(T)$.
It was found that at temperatures lower than 66 ^oK the
$n_2(T)$ values were in the same order of magnitude or less
than the experimental errors of the $n(T)$ measurements.

The experimental results of all ion implanted
samples were analysed with the above described method.
The theoretical approximations of the carrier concentra-
tion curves that resulted from the Hall effect and con-
ductivity measurements are also plotted on the graphs. In
Table (4.2) the electrical properties of nitrogen implanted
silicon samples, that were obtained from this study are
summarized. The donor impurity concentrations, the ioniza-
tion energies and the level of compensation in percent are
listed for each sample.

It must be emphasized that this is not the only
model which could be used for the analysis of the electri-
cal characteristics of semiconductors dominated by several
localized impurity levels. It is sometimes useful to apply
the phenomenon of "multivalent flaw" suggested by Shockley
and Last [40] as a general name for any permanent pertur-
bation of the periodic crystal lattice which could give
rise to localized states. The word "impurity" sometimes
carries the connotation that localized states have arisen
from the presence of foreign atoms. Similarly word "defect"
or imperfection are often taken to imply the activities of

SAMPLE	SI-146	SI-170	SI-171	SI-192	SI-53	SI-35
TOTAL DOSE $(1/cm^2)$	1.4×10^{14}	2.8×10^{14}	1.4×10^{14}	1.4×10^{14}	8.0×10^{14}	1.4×10^{14}
TOTAL ANNEAL TIME (M.)	10	10	30	30	10	20
$N_{d1}+N_{d2}-N_a$ $(1/cm^3)$	4.3×10^{16}	7.8×10^{16}	4.0×10^{16}	3.6×10^{16}	1.25×10^{16}	3.12×10^{16}
$N_{d1}-N_a$ $(1/cm^3)$	1.0×10^{16}	2.0×10^{16}	1×10^{16}	9.0×10^{15}	4.5×10^{15}	8.0×10^{15}
E_{d1} (eV)	0.0155	0.0155	0.016	0.016	0.017	0.017
E_{d2} (eV)	0.0365	0.035	0.035	0.034	0.030	0.037
COMPENSATION (%)	49	43	49	46	48	45

Table 4.2 Electrical characteristics of the nitrogen implanted silicon samples, obtained from low temperature conductivity and Hall effect measurements.

lattice vacancies, interstitials or combinations of
the two. The term "flaw" encompasses foreign atoms,
vacancies, interstitials or combinations of any of these.
Some flaws are monovalent and present a single level
in the energy band gap. Other kinds of flaw are multi-
valent, and a series of levels are presented.

When a set of multivalent centers is the dominant
one in determining the electronic equilibrium, it is
necessary to give a generalized discussion of the distri-
bution over the available states. The equations can be
formulated from a direct statistical approach or from
free energy considerations. This subject has been dis-
cussed by Landsberg,[41, 42] and by Shockley and Last [40];
while the particular case of divalent donors was discussed
by Champness [43]. It has been shown in these studies
that the problem of divalent donors is very similar to that
of several kinds of monovalent donors present in identical
amounts.

4.2.4. Discussion

In the preceeding sections, the results of the Hall
effect and conductivity measurements in nitrogen implan-
ted silicon as a function of temperature are presented.

It has been established that the implantation tempe-
rature, dose rate , total dose, layer profile and annealing

have little effect on the resulted n-type behaviour of the nitrogen implanted layers.

It has been indicated in previous studies on the nitrogen-silicon system that the implantation of nitrogen into silicon does produce a layer with n-type characteristics and the number of active carriers in the layer is much less than the number of implanted ions. These two results are common with the findings of this investigation. In most of the previous works, it was assumed that the nitrogen is substitutional and ionization energies were quoted based on this assumption. However, data and the method of calculating the ionization energy were not presented in these reports with the exception of Zorin et.al.[44]. Zorin calculated the ionization energy of the donor-like impurities by fitting a theoretical curve to data obtained from Hall effect measurements in the 100 $^{\circ}$K to 300 $^{\circ}$K temperature range. These temperatures are relatively high and the range is too narrow to determine the ionization energy with resonable accuracy.

In this study Hall effect and conductivity data were obtained in a much wider temperature range, between 15 $^{\circ}$K and 300 $^{\circ}$K . However, it was impossible to fit the normalized carrier concentration data with theoretical curves of a semiconductor model with single donor level. This fact indicated the possibility of the presence of more than one

donor level . Therefore, it was assumed that either several monovalent donors or a set of multivalent defects can account for the observed behaviour. The attempts to fit the experimental curves with theoretical ones were successful when a semiconductor model dominated by several donor levels was applied. It has been found that the concentration curves of all the samples could be characterized by the same ionization energies.

The results imply that the n-type properties observed in the implanted layers are unique to nitrogen. However, it is not known whether substitutional nitrogen or nitrogen induced defects are responsible for this type of behaviour.

There are arguments to support either substitutional donor behaviour or a defect conduction mechanism of the implanted nitrogen. The ionization energies which are independent of implantation and annealing conditions suggest a substitutional position for the nitrogen. The fact that nitrogen does not fit into the silicon lattice very well and hence could trap or stabilize defects supports the idea of interstitial nitrogen or a defect conduction mechanism created by the implanted nitrogen [16].

In order to determine whether substitutional nitrogen or nitrogen induced defect centers (or the combination of the two) is responsible for the observed electrical characteristics experimental techniques other than the ones

used in previous investigations [16] have to be developed.

It has to be also noted that the observed electrical behaviour is not unique to the nitrogen - silicon system. Similar properties of the zinc-doped germanium is well known from the experimental data of Tyler and Woodbury [32], where the multivalent acceptor behaviour of zinc impurities are described by a semiconductor model dominated by several localized acceptor levels.

4.2.5. Summary

Donor like behaviour of the nitrogen implanted silicon samples was observed and it was found that the number of active donor centers in the implanted layer were much less than the number of implanted nitrogen ions. The conversion efficiency was found to be very low, less than one percent. These results are in agreement with earlier reports on nitrogen implanted silicon.

It was assumed that more than one donor level exists in the energy band model of nitrogen implanted silicon and their presence could account for the typical temperature dependence of the carrier concentration.

In the analysis, a semiconductor model was used which had two species of monovalent donor impurities

with some assorted compensating acceptors. The activation
energy obtained for the first donor level was 0.016 ± 0.001 eV
and for the second deeper donor energy level 0.034 ± 0.003 eV
was determined. The less accurate determination of the acti-
vation energy of the second donor level was due to that it
was obtained by fitting the carrier concentration curves
in the intermediate temperature range; while, the first do-
nor level activation energy was determined from the course
of the carrier concentration vs. 1/T at very low temperatu-
res.

It has been stated in the analysis that this is
not the only model which could describe the particular
properties of nitrogen implanted silicon. The equations
formulated for a semiconductor model comprising of a set
of multivalent flaws (defects) would give similar results
in the particular case of divalent donors.

It has been established throughout the course of
these experiments that the donor behaviour of nitrogen
implanted silicon could be characterized by two types of
monovalent donors or a set of multivalent defects. Both
ionization energies were found to be independent of the
implantation and annealing conditions.

It was possible to produce controlled, reproducible
dopant concentrations in the implanted layer when the
total dose of the implants was in the order of 1.4×10^{14}
ions/cm^2 .
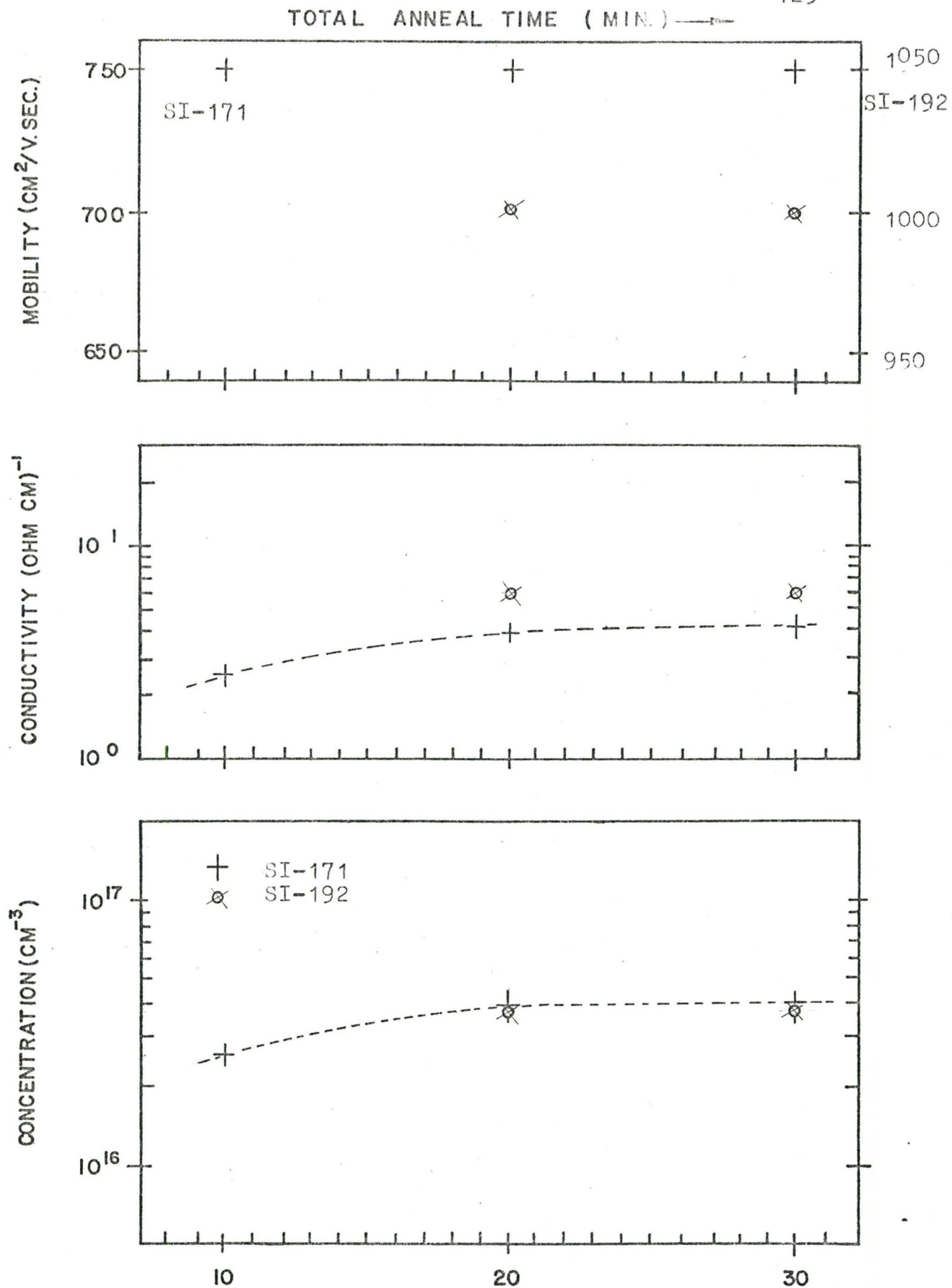
Figure (4-18). The effect of the anneal time on the fundamen-
electrical parameters of nitrogen implanted silicon.
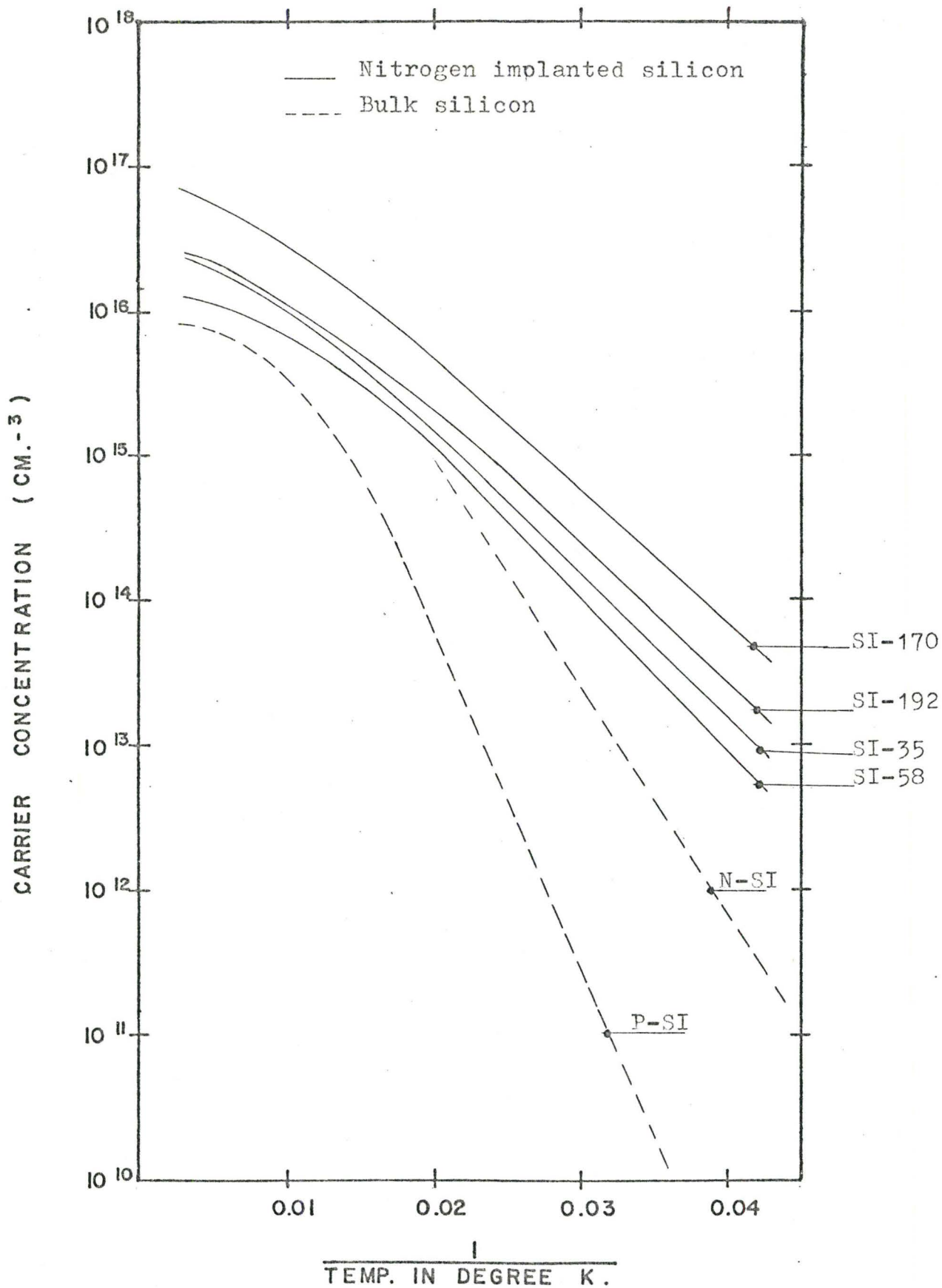
Figure (4-19). Comparison between the n vs. (1/T) graphs of nitrogen implanted silicon samples and bulk silicon samples.

A slight increase in the carrier concentration and conductivity was observed by increasing the annealing time from 10 to 20 minutes, as it is shown in Figure (4-18). In Figure (4-19) the carrier concentration curves of the nitrogen implanted samples are compared with the characteristics of typical bulk silicon samples and presented in a summary form.

4.3.   Oxygen Ion Implanted Silicon Samples

4.3.1.   Introduction

In this chapter the results of the study of the electrical properties of oxygen ion implanted silicon are presented.

The donor behaviour of oxygen in silicon is well known from previous investigations on the subject.   In the earlier experiments the oxygen content of silicon single crystals was studied. It was demonstrated that pulled silicon single crystals contain considerable amounts of oxygen as an impuity [45, 46]. The formation of donor states during a heat treatment (at about 450 $^{\circ}$C) of high oxygen content silicon crystals was first reported by Fuller, Dietzenberger, Hannay and Buehler [47], and connected with the oxygen concentrations in the silicon samples. W.Kaiser and P.H. Keck [48] determined the oxygen content of pulled silicon crystals by vacuum fusion gas analysis and correlated it with the infrared absorption of $9\,\mu$. This band was identified to be a vibrational band of the interstitial oxygen.

Later a theory was proposed by Kaiser, Frisch and Reiss [17] which was able of explaining the mechanism of donor formation during heat treatment of silicon crystals. In their theory the creation of silicon - oxygen atomic

aggregates (SiO_2, SiO_3, SiO_4) was used to describe the creation of active impurity centers due to heat treatment, in good agreement with experiments. A new infrared band was observed at 12 μ in electron-irradiated silicon, and was identified as the vibrational band of substitutional oxygen.[49] In addition to the localized modes of oxygen in crystalline silicon, an optical absorption band at 1.8 μ associated with an electronic transition of divacancies (defects) had been measured in electron- [50] and neutron- [51, 52] irradiated silicon. The same 1.8 μ characteristic divacancy absorption band was detected in 400 keV oxygen ion implanted silicon [53]. It was found that the divacancies produced by ion implantation anneal completely between 100 ^{o}C and 250 ^{o}C [53].

H.J. Stein and Wendland Beezhold [54] reported that the optical absorption bands of the vibrational modes for both interstitial (9 μ) and substitutional (12 μ) oxygen have been observed in crystalline silicon implanted with 220 keV oxygen ions at 300 ^{o}K . In their experiments, the sum of the observed interstitial and substitutional oxygen atoms was found to be approximately equal to the number of implanted oxygen ions. In addition of the above two vibrational modes, the electronic transition of the divacancy (1.8 μ) was also measured.

The results of the previous investigations of the

oxygen – silicon system can be summarized as follows :

1) The donor formation in high oxygen content silicon was observed during heat treatment, and a theory was established to explain the above process.

2) The localized vibrational modes of the interstitial and substitutional oxygen had been observed in oxygen-rich , and oxygen – rich irradiated silicon respectively. In addition, the $(1.8\ \mu)$ absorption band was identified with the electronic transition of the divacancy.

3) Both vibrational modes and the characteristic band of the divacancy have been observed in oxygen ion implanted silicon.

Although a number of studies have been carried out on the oxygen implanted silicon system, none of them investigated the electrical characteristics of oxygen implanted silicon layers using Hall effect and sheet resistivity measurements. The objective of this work was to fabricate oxygen ion implanted silicon Hall samples and investigate the electrical properties of such samples. 80/40 keV implantations into high resistivity silicon substrates were performed at 300 ^{o}K approximately 6° to 9° off the <111> axis. To produce relatively uniform implanted layer profiles, 3 : 1 dose ratio was maintained. The sample preparation and cleaning procedures were the same as those used in the nitrogen ion implantations. The electrical properties of the samples were studied as a function of various implantation and annealing

conditions.

4.3.2. Experimental Results

The implantation and annealing conditions are
summerized in Table (4.3) . The $1.4 \times 10^{14}/cm^2$ total dose
which was generally used in the nitrogen implantations was
applied to the first oxygen implantation experiment (Si - 1).
This sample was subjected to 20 minutes anneal cycles from
$375\ ^oC$ in 25^oC to $50\ ^oC$ steps. No electrical activities
were observed in the implanted layer until the sample was
annealed at $825\ ^oC$ for 20 minutes. Room temperature
Hall effect and conductivity measurements indicated donor
like behaviour of the implanted layer and in order to
characterize the layer the resistivity (0.64 ohm-cm) and
the carrier concentration ($1.08 \times 10^{16}/cm^3$) were deter-
mined from these measurements. The size of the implanted
layer used in the calculations is given by the following
dimensions : 0.5 cm in length, 0.2 cm in width, and
2×10^{-5} cm in thickness. The thickness of the layer was
estimated by using data available from the literature and
the results of the layer thickness measurements for the
nitrogen implants [16] under the same implantation condi-
tion .

The conversion efficiency was found to be very low
for the oxygen ion implantations after high temperature

SAMPLE	SI-I	SI-1	SI-3	SI-2	SI-9
IMPLANT TEMP.($°K$)	300	300	300	300	400
TOTAL DOSE ($1/CM^2$)	1.4×10^{14}	2.8×10^{14}	2.8×10^{14}	4.2×10^{14}	5.6×10^{14}
DOSE RATE (nA/CM^2)	100	100	120	260	100
1st IMPLANT. ENERGY (keV)	80	80	80	80	80
2nd IMPLANT. ENERGY (keV)	40	40	40	40	40
ANNEAL TEMP.($°C$)	825	825	850	850	825
TOTAL ANNEAL TIME (MIN.)	10	100	100	120	200
Carrier Conc. ($1/cm^3$)	1.05×10^{16}	2.0×10^{16}	2.14×10^{16}	5.42×10^{16}	2.0×10^{17}

Table 4.3 Summary of the implantation and annealing conditions of oxygen

ion implanted samples.

anneal. Less than 0.5% of the implanted oxygen ions have became active after the 825 ^{o}C, and 20 min. anneal. This sample was cleaned again and was implanted with the same amount of oxygen dose (1.4 x 10^{14} ions/cm^2), then annealed for an additional 10 minutes at 825°C and mounted in the automatic Hall effect and conductivity measuring equipment. The room temperature free carrier concentration was determined to be approximately twice as much as it was after the first part of the experiment.

In order to check the reproducibility of the oxygen implantations, another sample (Si-3) was implanted with 2.8 x 10^{14} ions/cm^2 dose at 300°K but only in one step. For (Si-3), practically the same conversion factor and number of active carriers in the implanted layer were measured after high temperature anneal as they were found in the case of (Si-1).

The total dose was increased by 1.4 x 10^{14} ions/cm^2 steps i.e. (Si-8) was implanted with 4.2 x 10^{14} ions/cm^2 and (Si-9) was implanted with 5.6 x 10^{14} ions/cm^2. The number of active carriers produced in oxygen implanted silicon as a function of implantation dose is shown in Figure (4-24). The anneal temperature was also increased from 825 ^{o}C to 850 ^{o}C , since at higher temperature the damage anneals out in shorter time . Figure (4-20),

Fig. (4.21), Fig. (4-22) and Fig. (4-23) show the electrical properties of the oxygen implanted silicon samples, obtained from the Hall effect and conductivity measurements. The normalized carrier concentration, carrier concentration, conductivity and mobility were plotted versus reciprocal temperature between $20^{\circ}K$ - $300^{\circ}K$. It was found that the number of active impurities in the implanted layer increased while the activation energies of the impurities decreased through an increse in the implanted oxygen doses. Sample (Si-9), which has the highest implanted dose, shows similar electrical properties as a heavily doped n-type semiconductor does. The decrease in the ionization energy was probably due to the donor level broading effect at higher impurity concentrations. A considerable decrease in the number of active impurity centers was experienced in case of sample (Si-8) after high temperature long time anneal, which may have been due to oxygen outdiffusing. Some increase in the activation energies toward the values obtained for lightly doped samples has been observed in the case of (Si-8) after longer duration anneal Fig. (4-22).
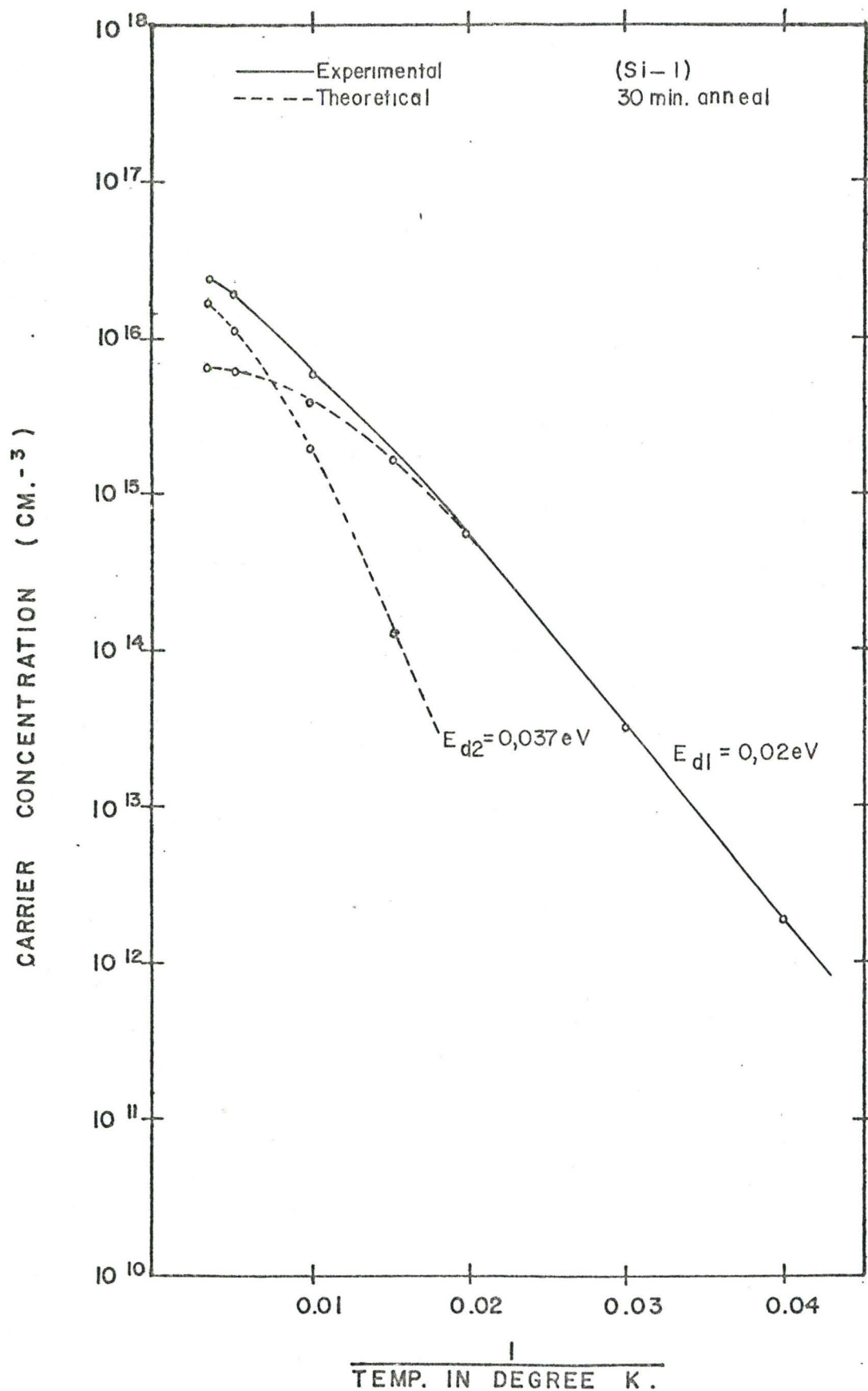
Figure (4-20 a). Carrier concentration vs. (1/T) graphs of silicon sample (Si-1) implanted at 300°K with 2.8×10^{14} $0^+/cm^2$, 80/40 keV.
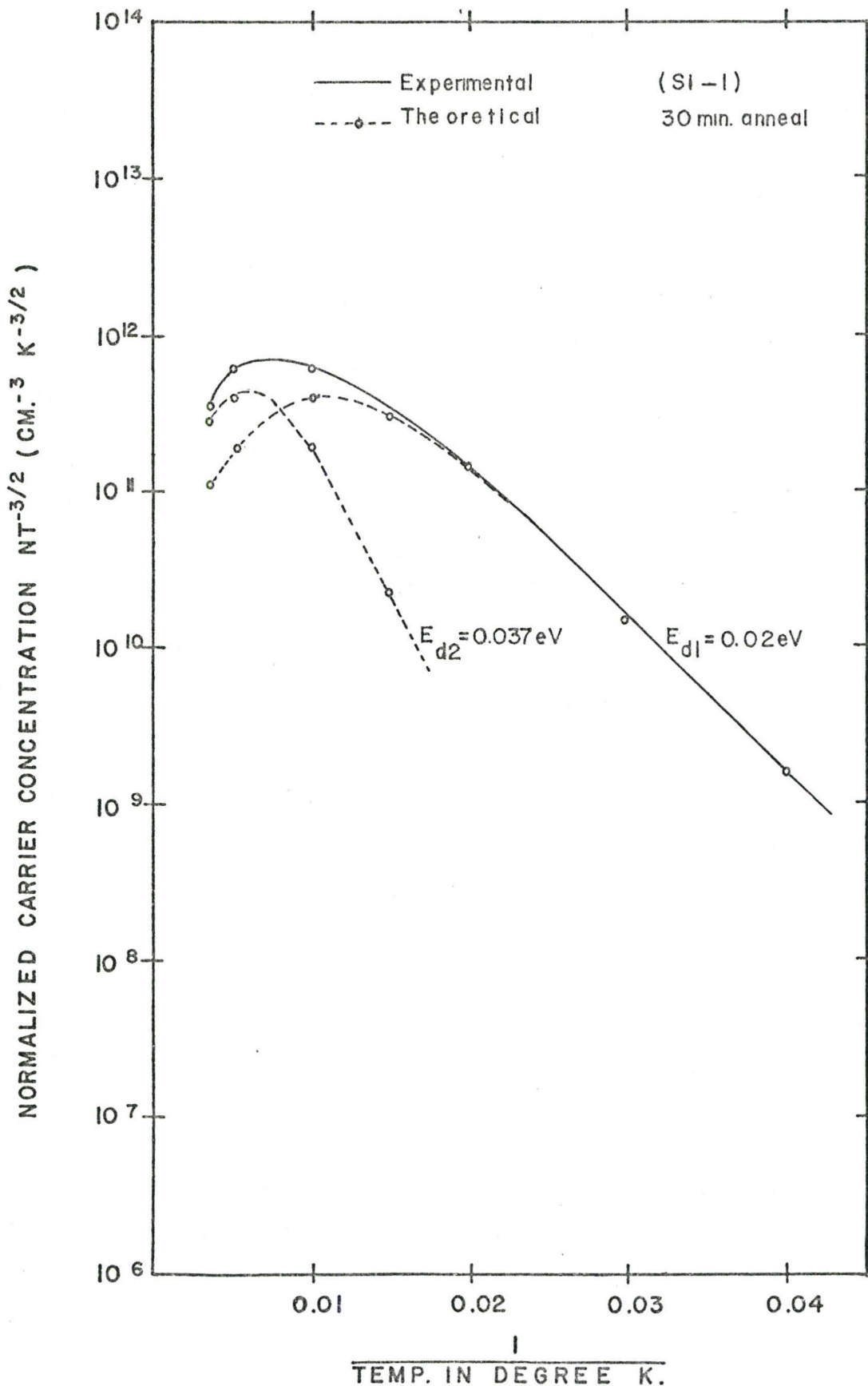
Figure (4 - 20b). Normalized carrier concentration vs.(1/T) graph of silicon sample (Si-1) implanted at 300°K with 2.8×10^{14} O^{+}/cm^2, 80/40 keV.
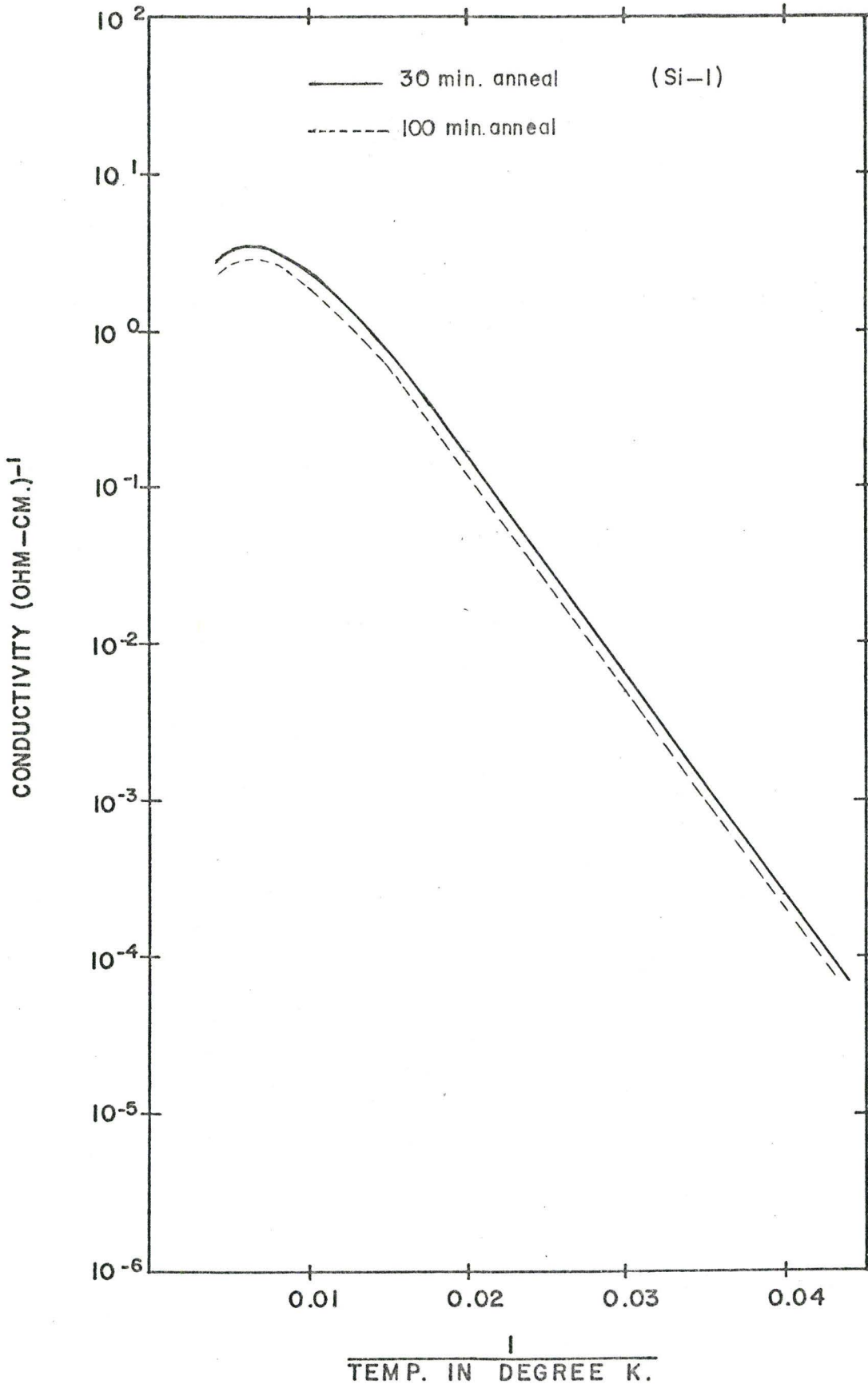
Figure (4-20 c). Conductivity vs. (1/T) graphs of silicon sample (Si-1) implanted at $300^\circ K$ with 2.8×10^{14} $0^+/cm^2$, 80/40 keV.
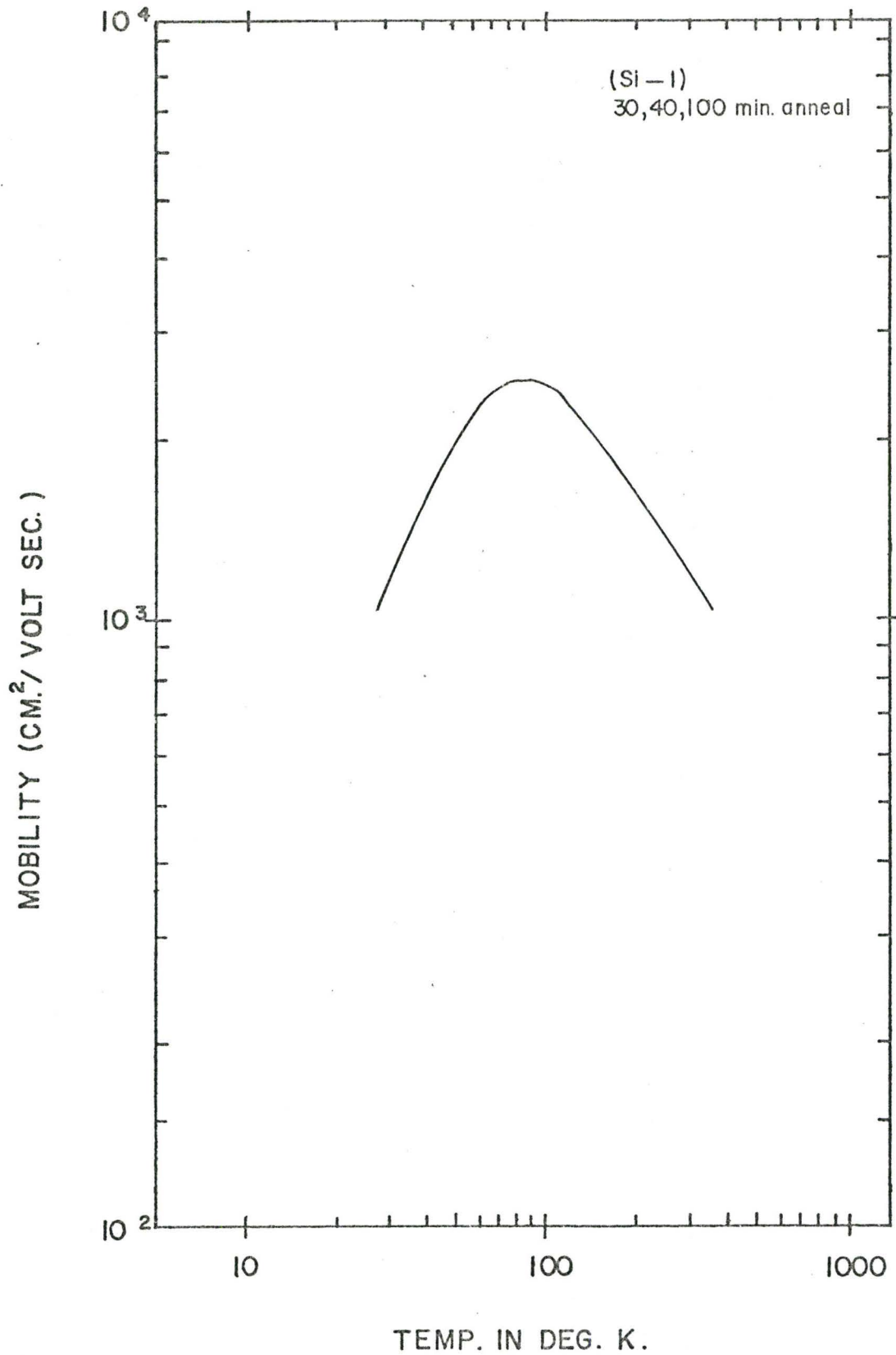
Figure (4-20 d). Mobility vs. (1/T) graph of silicon sample (Si-1) implanted at 300°K with 2.8×10^{14} $0^+/cm^2$, 80/40 keV.
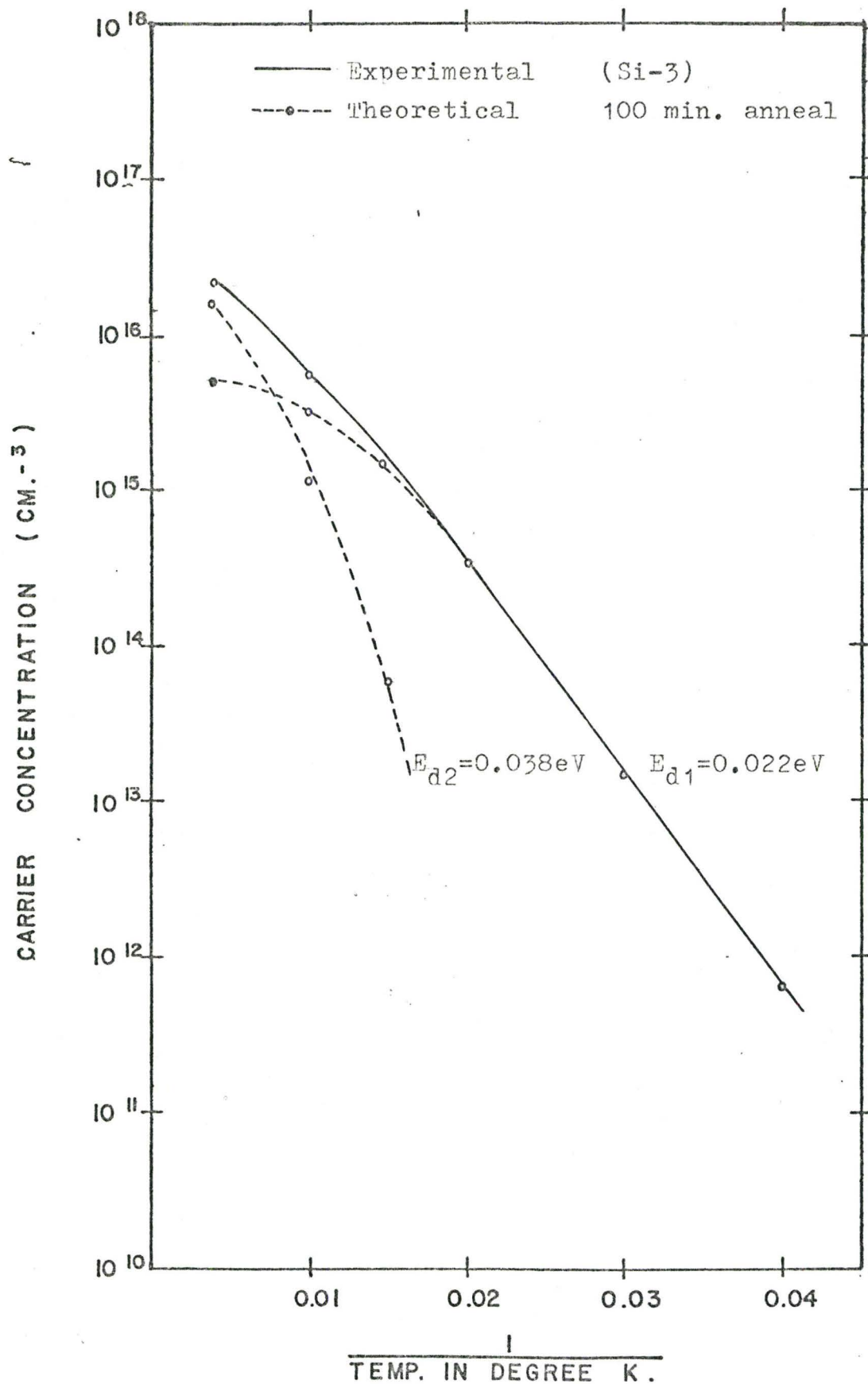
Figure (4-21 a). Carrier concentration vs. (1/T) graphs of silicon sample (Si-3) implanted at 300°K with 2.8 x 10¹⁴ 0⁺/cm², 80/40 keV.
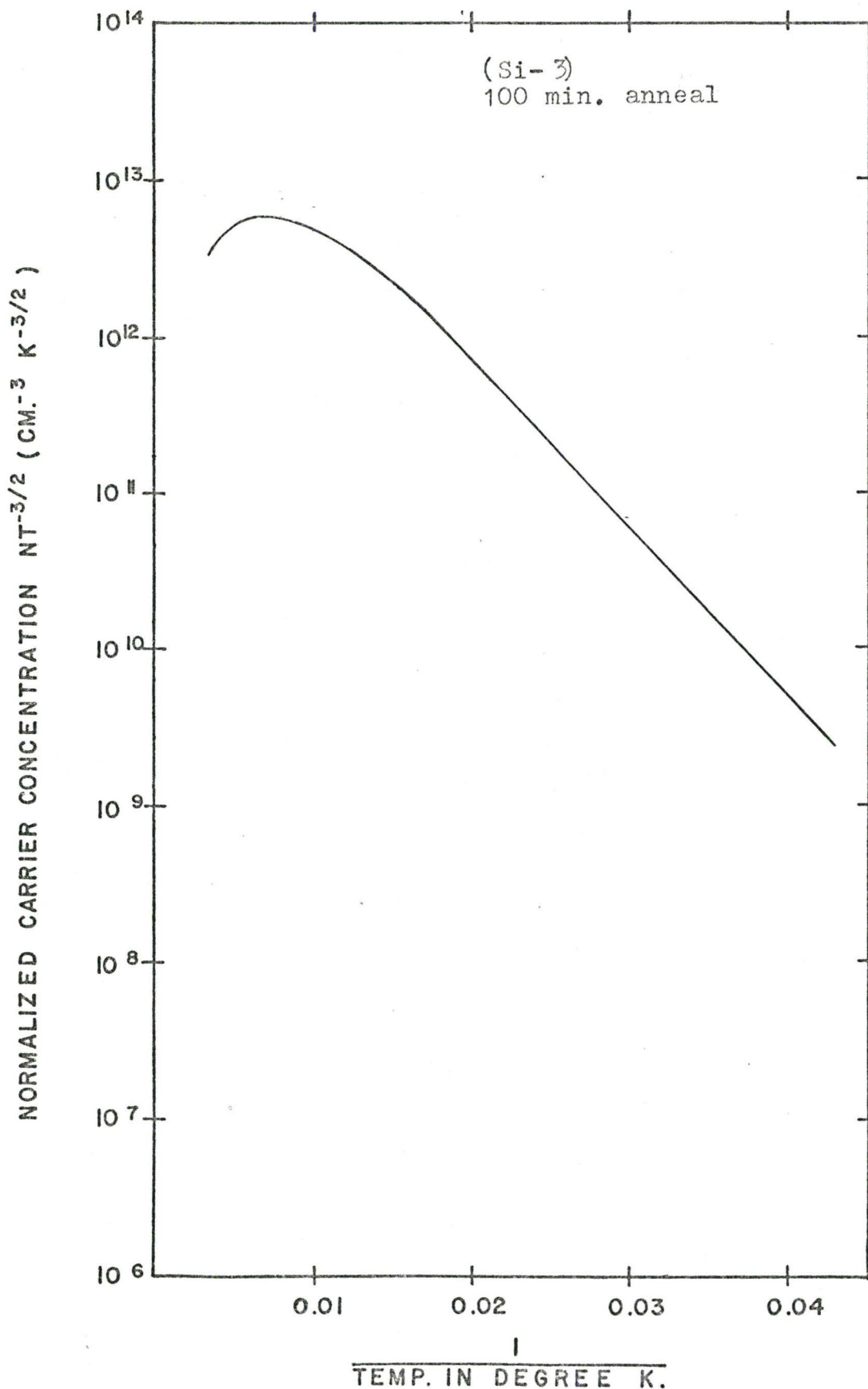
Figure (4-21b). Normalized carrier concentration vs. (1/T) graph of silicon sample (Si-3), implanted at 300°K with 2.8×10^{14} O^+/cm^2, 80/40 keV.
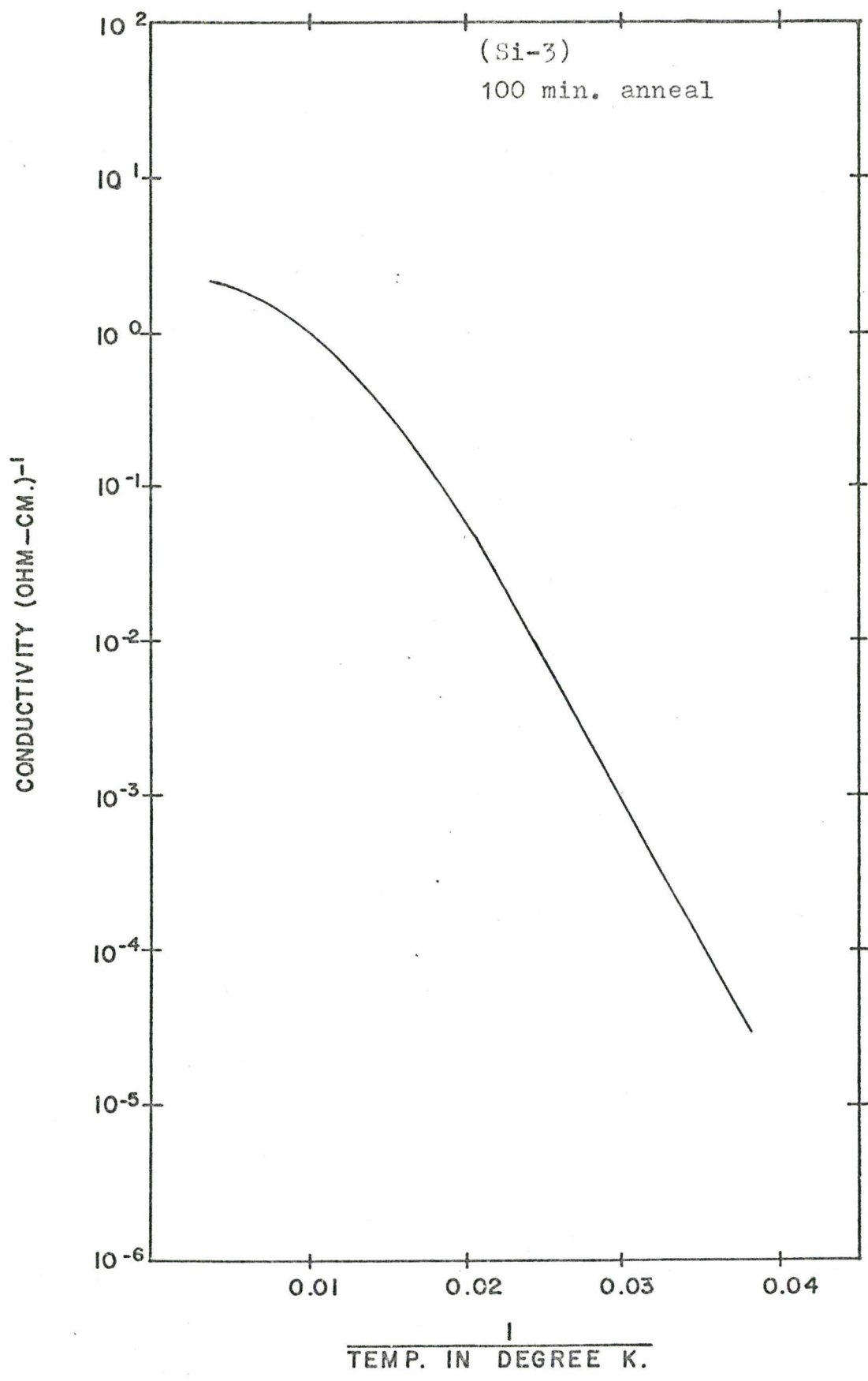
Figure (4-21 c). Conductivity vs. (1/T) graph of silicon sample (Si-3) implanted at 300°K with 2.8 x 10^{14} 0$^+$/cm^2, 80/40 keV.
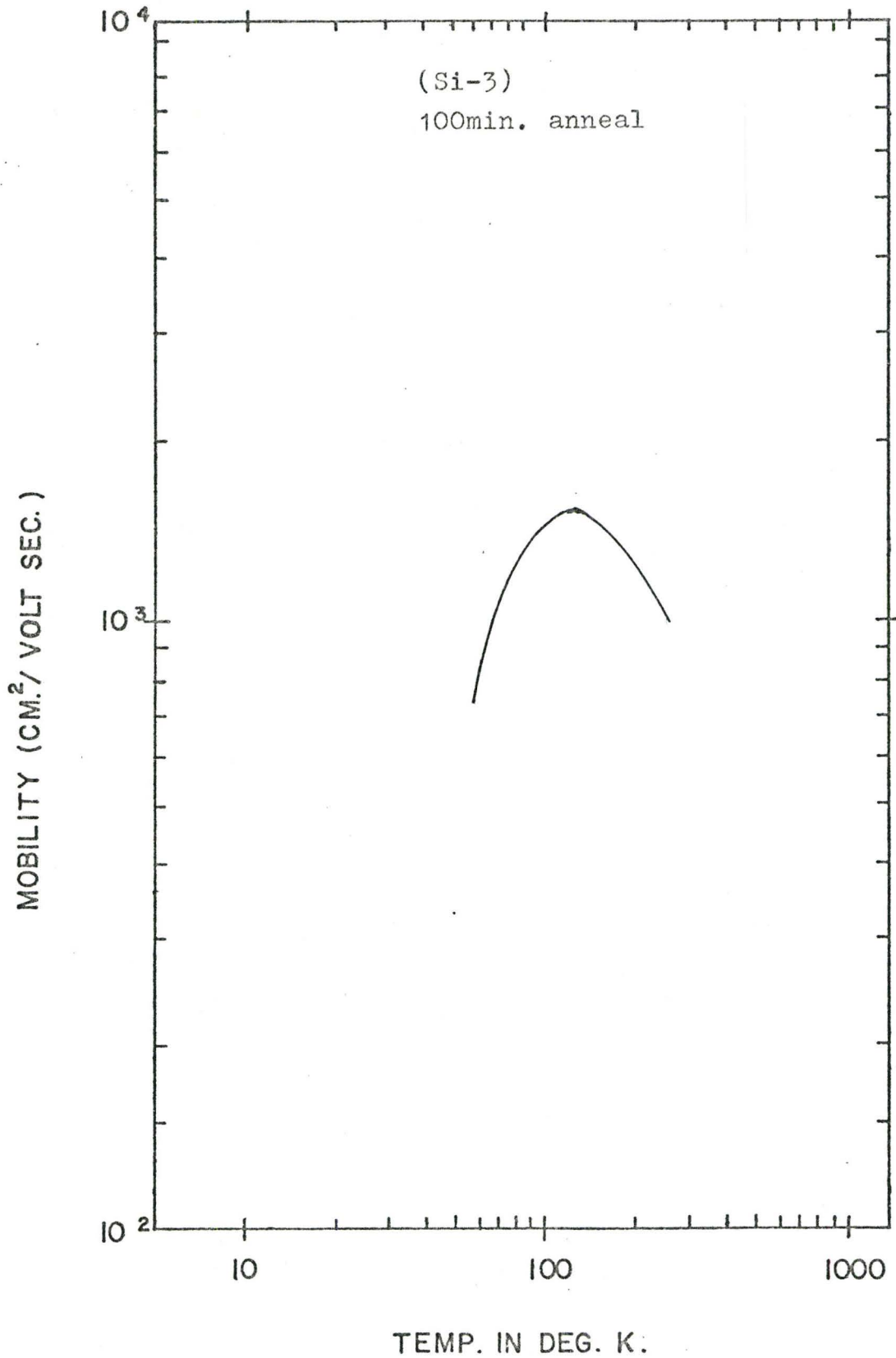
Figure (4-21 d). Mobility vs. (1/T) graph of silicon sample (Si-3) implanted at 300°K with 2.8×10^{14} 0^{+}/cm^{2}, 80/40 keV.
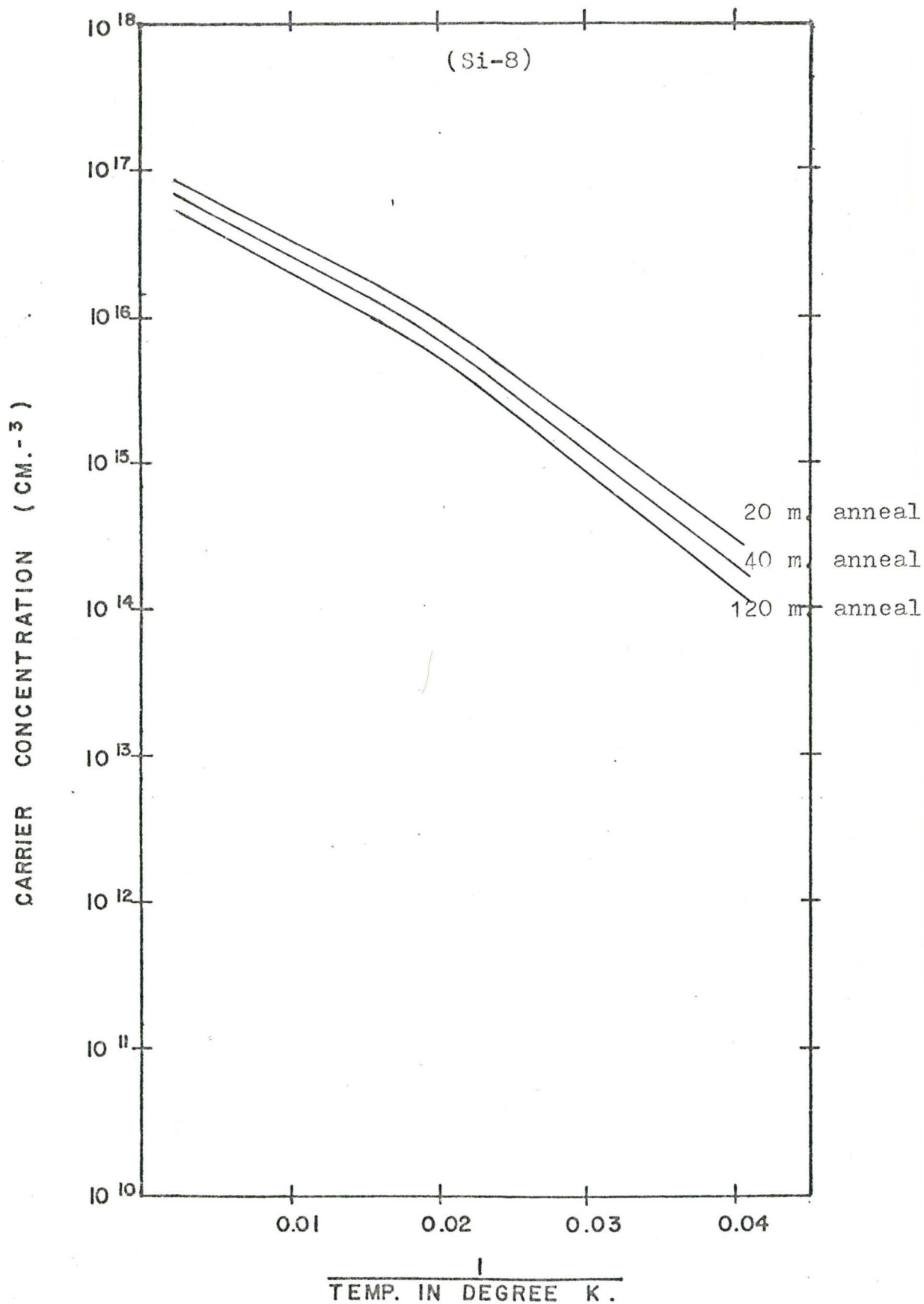
Figure (4-22 a). Carrier concentration vs. (1/T) graphs of silicon sample (Si-8) implanted at 300°K with 4.2 x 10^14 0^+/cm^2, 80/40 keV.
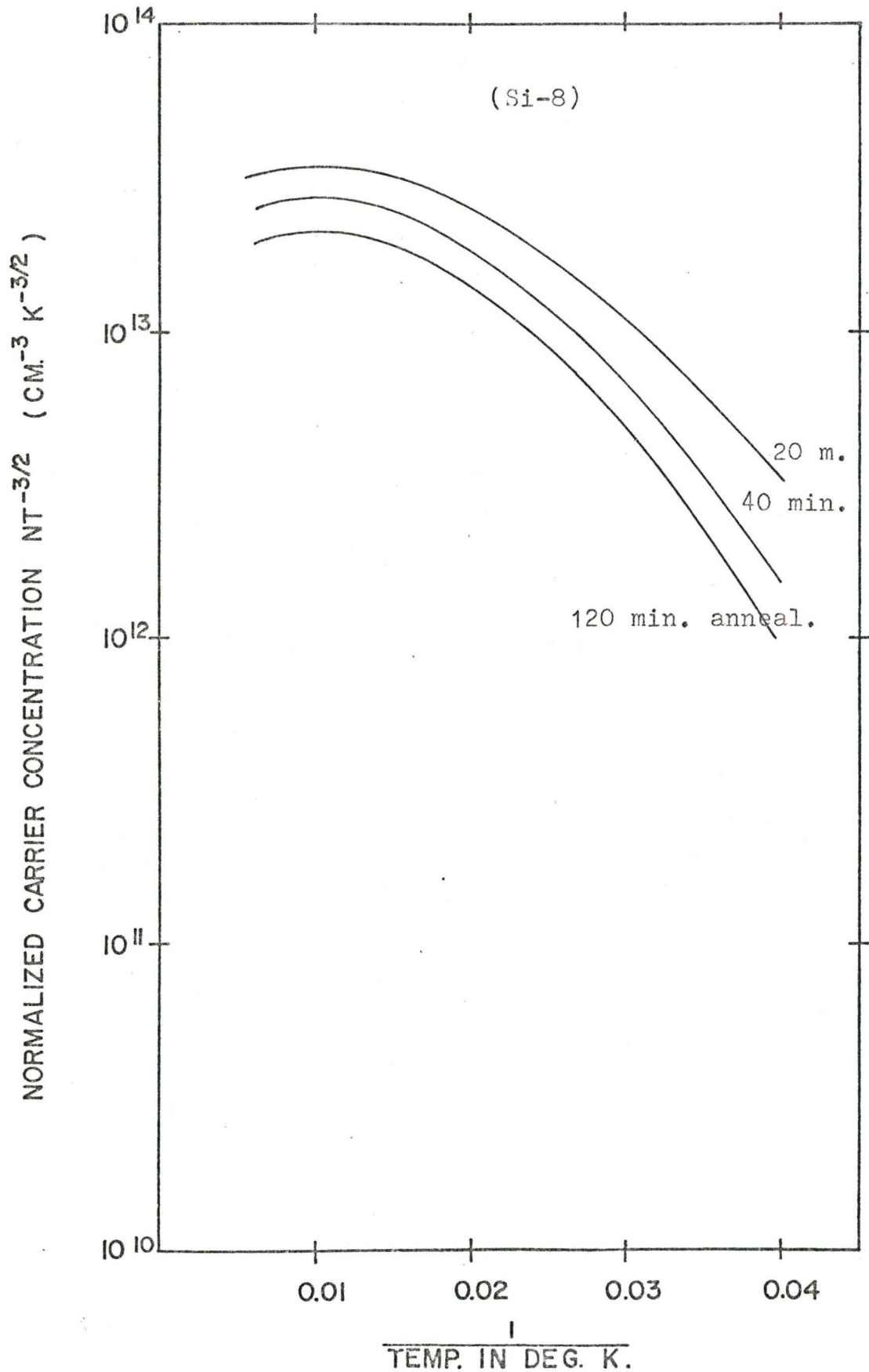
Figure (4-22 b). Normalized carrier concentration vs. (1/T) graphs of silicon sample (Si-8) implanted at 300°K with 4.2×10^{14} $0^{+}/cm^{2}$, 80/40 keV.
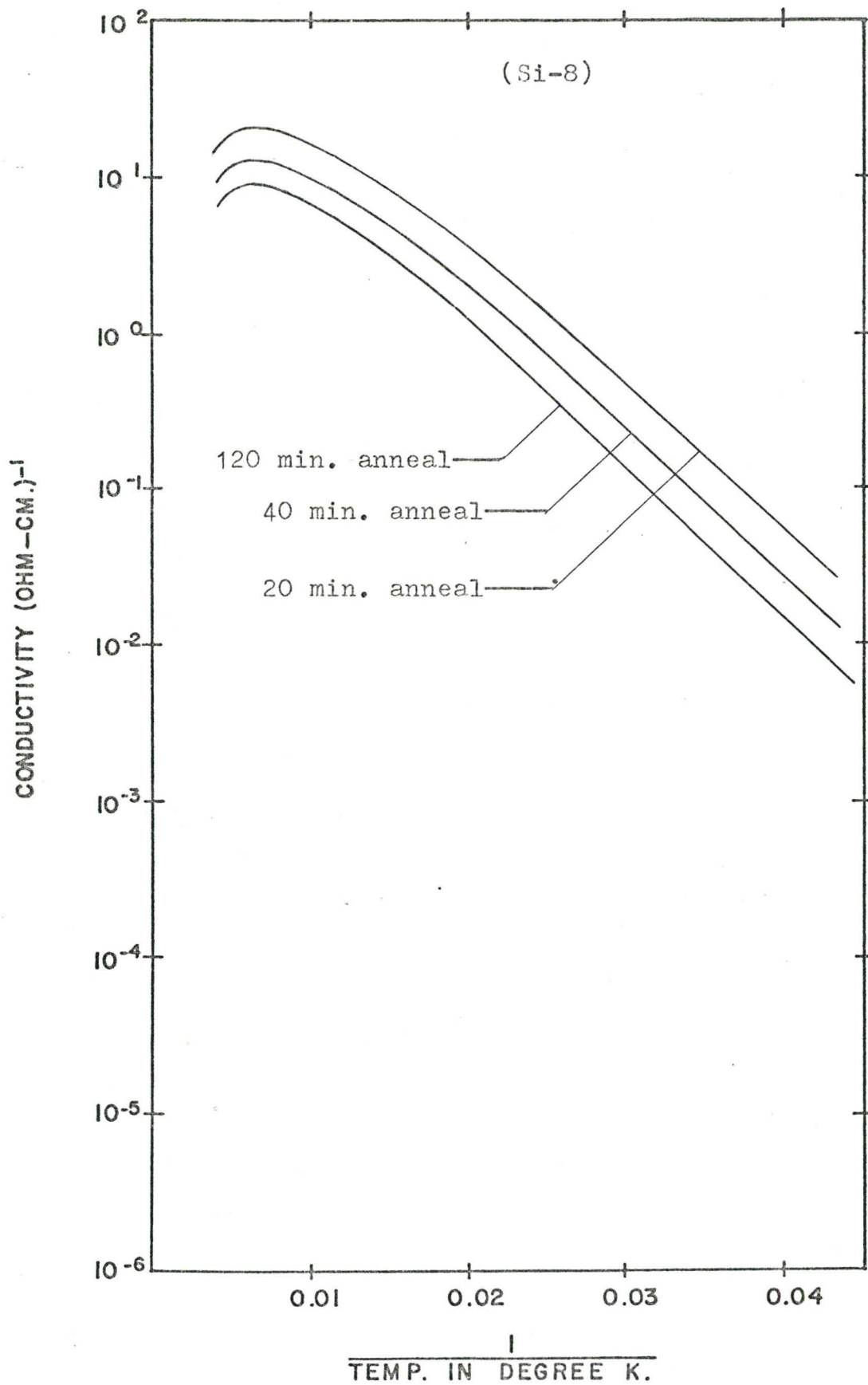
Figure (4-22 c). Conductivity vs. (1/T) graphs of silicon sample (Si-8) implanted at $300^{\circ}K$ with 4.2×10^{14} $0^{+}/cm^{2}$, 80/40 keV.
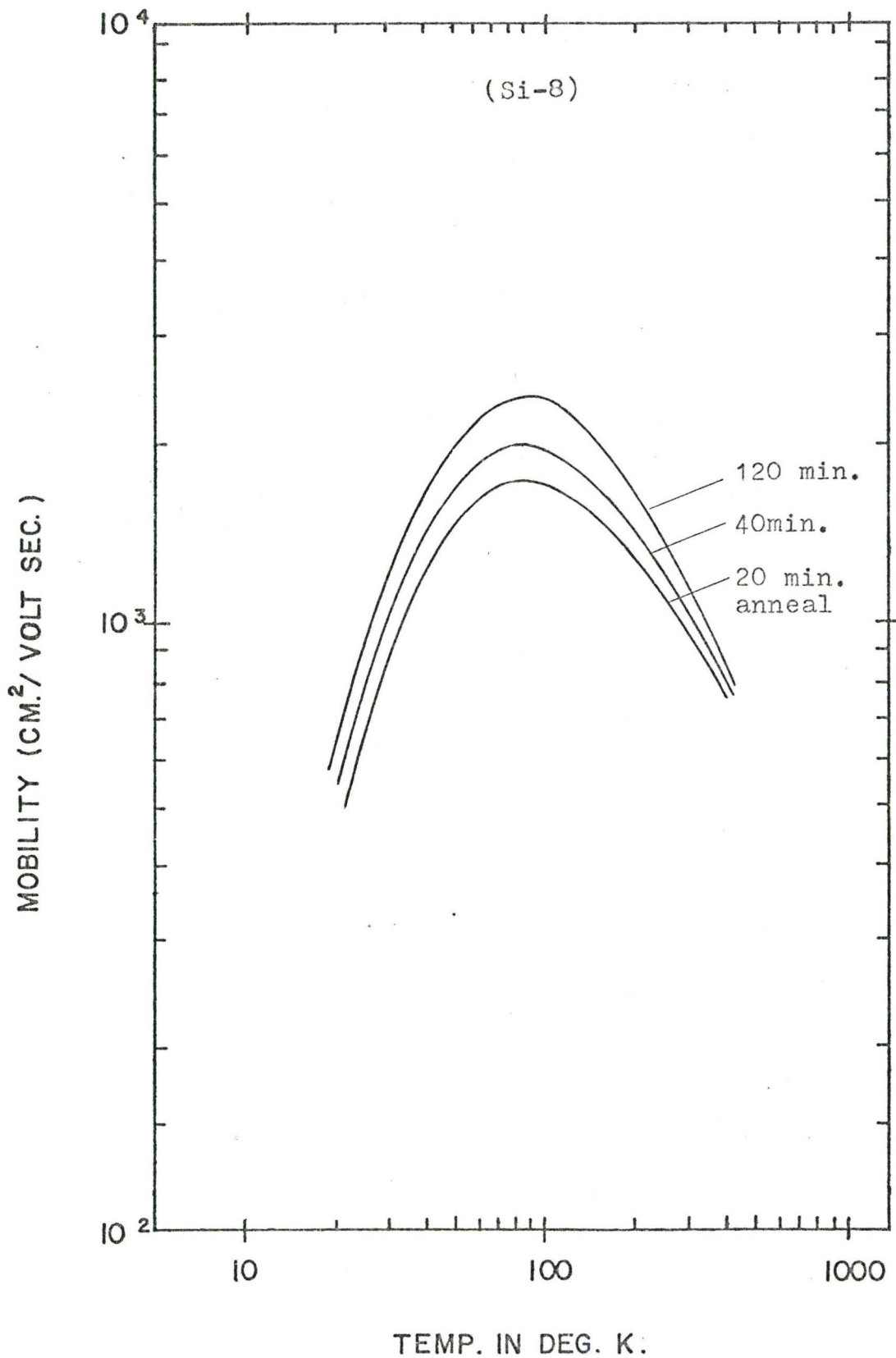
Figure (4-22 d). Mobility vs. (1/T) graphs of silicon sample
(Si-8) implanted at 300°K with 4.2 x 10^{14} $0^{+}/cm^2$,
80/40 keV.
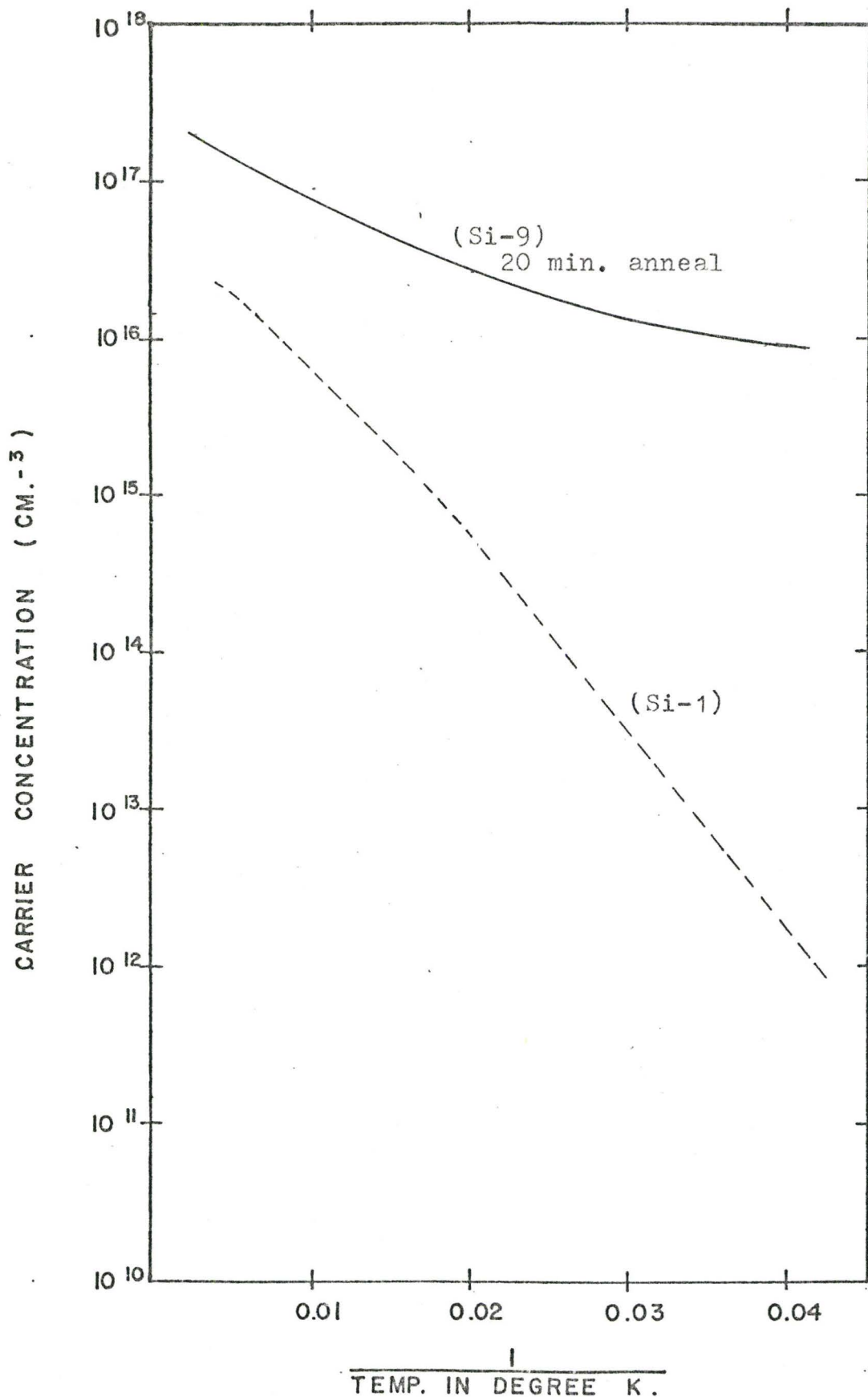
Figure (4-23 a).   Carrier concentration vs. (1/T) graphs of
silicon   sample (Si-9) implanted at 400°K
with 5.6 x 10^{14} 0^{+}/cm^2, 80/40 keV.
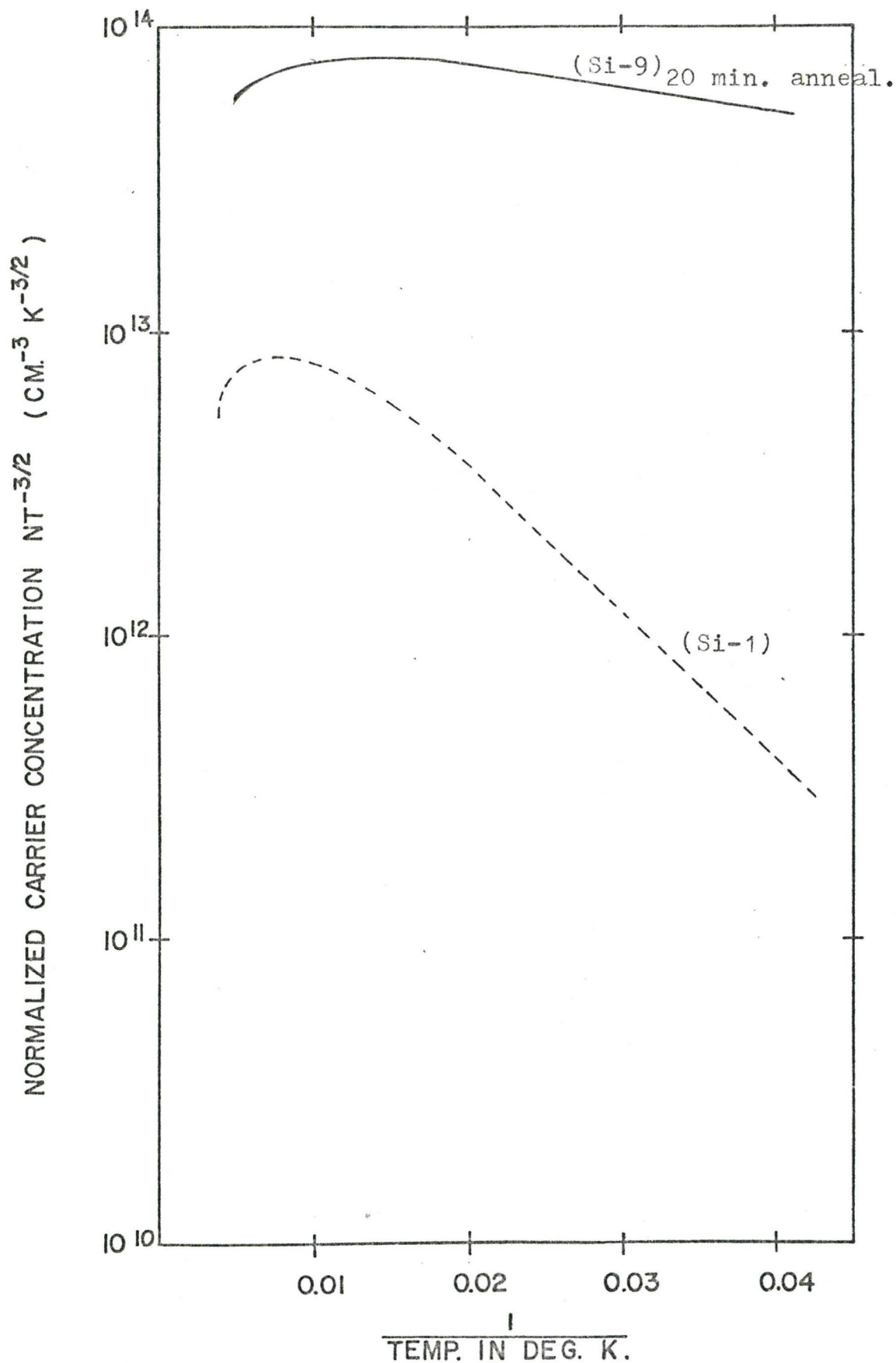
Figure (4-23 b). Normalized carrier concentration vs. (1/T) graph of silicon sample (Si-9) implanted at $400^\circ K$ with $5.6 \times 10^{14} \, 0^+/cm^2$, 80/40 keV.
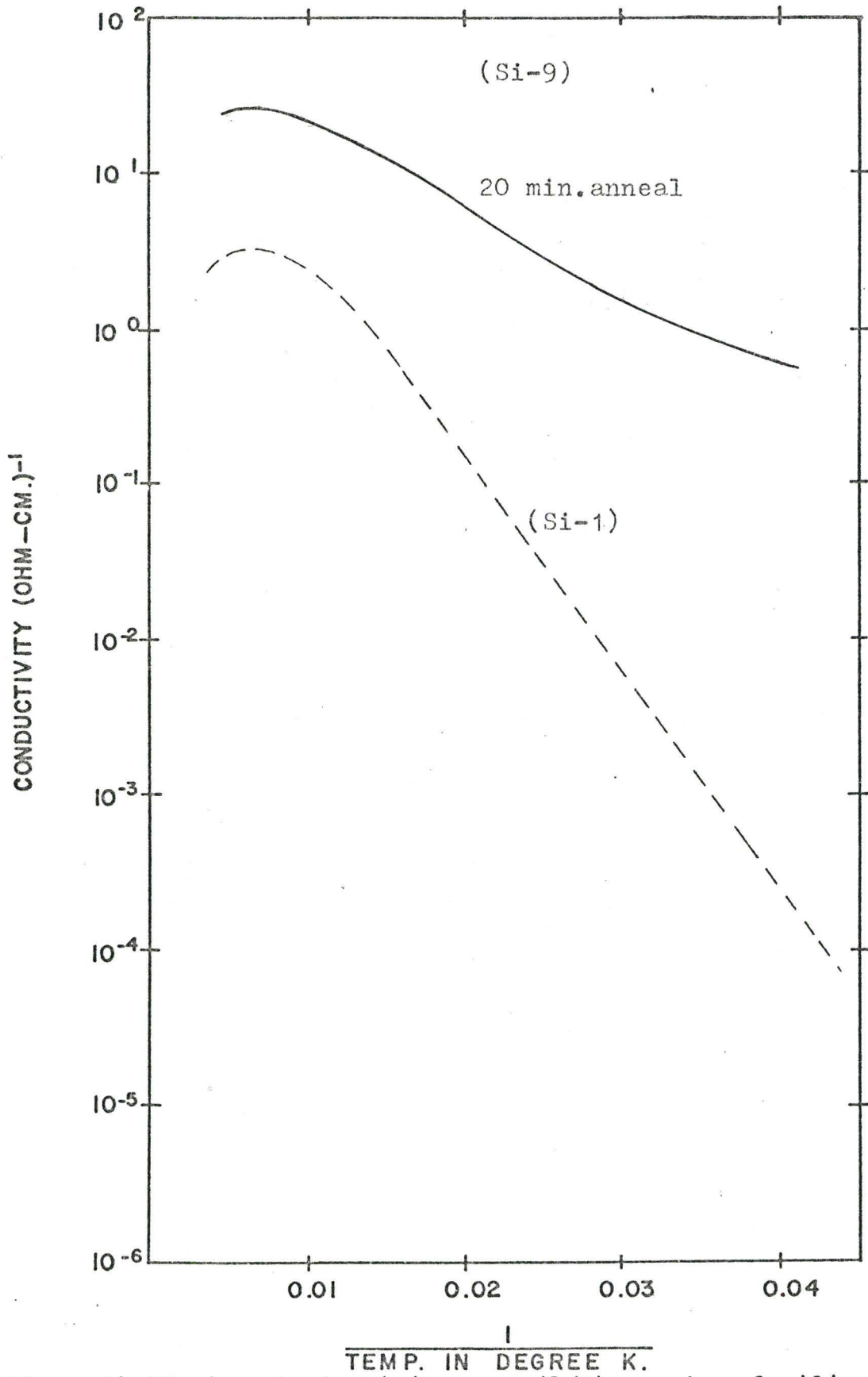
Figure (4-23 c). Conductivity vs. (1/T) graph of silicon sample (Si-9) implanted at $400^{\circ}K$ with 5.6×10^{14} $0^{+}/cm^2$, 80/40 keV.
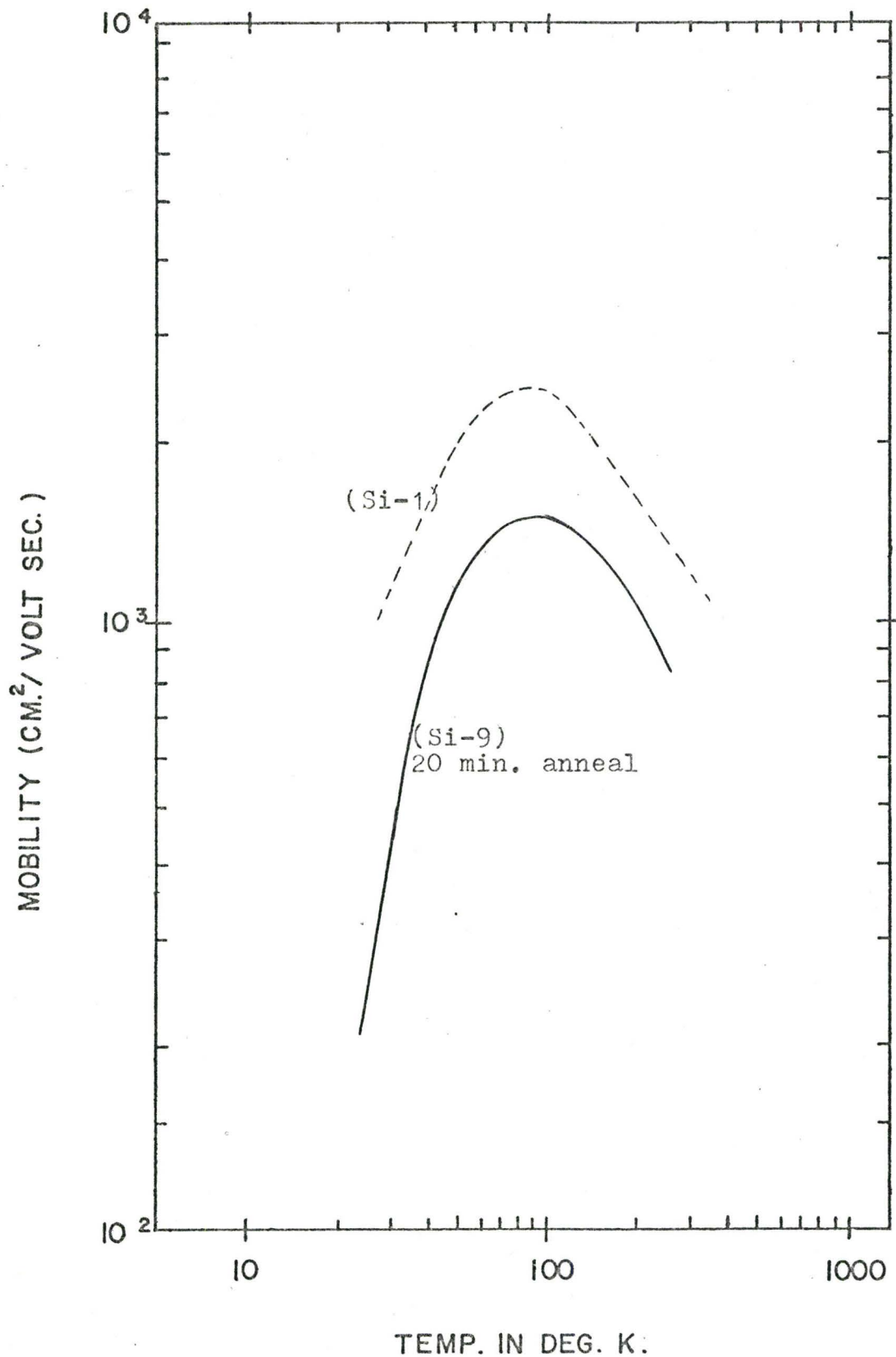
Figure (4-23 d). Mobility vs. (1/T) graph of silicon sample (Si-9) implanted at 400°K with 5.6 x 10^14 0^+/cm2. 80/40 keV.

4.3.3. Analysis

The carrier concentration versus reciprocal temperature graphs of the oxygen ion implanted silicon samples were analysed in order to characterize the electrical properties of the implanted layers. The objective was to determine the ionization energies of the dopants and the degree of compensation from the low temperature Hall effect and conductivity measurements, and to approximate the experimental carrier concentration curves with theoretical ones of an applicable model. Although the application of a partially compensated single donor level semiconductor model gave valid activation energy value of a donor level in the energy band structure of the oxygen implanted silicon, it failed to describe the n vs. 1/T graphs in the entire $20^{\circ}K - 300^{\circ}K$ temperature range, particularly at intermediate temperatures between $60^{\circ}K$ and $300^{\circ}K$.

It was possible to describe the course of the carrier concentration vs. 1/T experimental function with a theoretical expression obtained for a partially compensated n-type semiconductor model containing two kinds of donors at different energies and assorted compensating impurities at a lower acceptor energy level. This was the same model which had been used in the analysis of the experimental results of nitrogen implanted silicon.

The activation energies and the compensating acceptor densities were determined for each sample and collected for comparison in Table (4.4) .

4.3.4. Discussion

From earlier studies, it is well known that oxygen could become a donor in silicon. Previous oxygen implantations indicated the presence of both substitutional and interstitial oxygen, and divacancies (defects) which could anneal at low temperatures. The results also indicated that the number of substitutional and interstitial oxygen was approximately equal to the number of implanted ions. The above results were obtained from optical absorption measurements.

In this investigations, it has been observed that oxygen implantation into silicon does produce a layer with n-type characteristics after a relatively high 825 ^{o}C - 850 ^{o}C temperature anneal . The electrical behaviour of oxygen implanted silicon is found to be similar to that of the nitrogen implanted silicon.

The theoretical fit of the experimental carrier concentration data was not possible with a single donor level semiconductor model in the entire 15 ^{o}K to 300 ^{o}K temperature range. However, the experimental data could

SAMPLE	SI-1	SI-1	SI-3	SI-8	SI-9
TOTAL DOSE (1/cm^2)	1.4×10^{14}	2.8×10^{14}	2.8×10^{14}	4.2×10^{14}	5.6×10^{14}
TOTAL ANNEAL TIME (min.)	10	100	100	120	20
$N_{d1} + N_{d2}$ N_a (cm^{-3})	1.08×10^{16}	2.0×10^{16}	2.14×10^{16}	5.42×10^{16}	2.0×10^{17}
$N_{d1} - N_a$ (cm^{-3})	5.02×10^{15}	4.0×10^{15}	5.35×10^{15}	1.35×10^{16}	5.0×10^{16}
E_{d1} (eV)	–	0.02	0.022	0.0125	–
E_{d2} (eV)	–	0.037	0.038	0.027	–
Compensation (%)	–	48	48.8	46.8	–

Table 4.4 The electrical characteristics of the oxygen ion implanted silicon
samples obtained from low temperature conductivity and Hall effect
measurements.

be approximated by a theoretical expression of a semiconductor model dominated by several impurity levels.

Two donor ionization energy levels (0.021 ± 0.001 eV, and 0.037 ± 0.001 eV) were obtained from the analysis of the experimental data. These ionization energies were found to be independent of the implantation and annealing conditions listed in Table (4.3).

Refering to the literature for comparison, the generally accepted value for the donor ionization energy of oxygen in silicon is 0.03 eV. This value is given by S.M. Sze and J.C. Irwin [55]. However, the data or the technique used to obtain this ionization energy was not given. The above ionization energy is in relatively good agreement with the findings of this investigation.

W. Fahrner and A. Goetzberger [56] reported a new method using MOS technique for finding deep energy levels in silicon. They reported two deep-lying donor levels (0.51 eV and 0.41 eV) in oxygen implanted silicon samples. Although exact conditions are not given in their report, it is known that the implantation energies were between 15 keV and 130 keV. They could not find a reasonable explanation for the rather large discrepancy between the ionization energy found in their experiments and the one reported by S.M. Sze and J.C. Irwin, other than stating

that oxygen can be incorporated into silicon in different
configurations, depending on the heat treatment and the
previous hystory of the sample. However, considering the
accuracy of the surface - potential measurement in their
work (±0.03 eV) , it is obvious that this MOS technique
can not be used for determining shallow impurity levels
with any accuracy at .all.

From our experiments , it is not known that
the donor behaviour experienced in oxygen implanted sili-
con was due to substitutional oxygen, interstatial oxygen,
lattice defects created by the implantation process or
the possible combinations of the above effects. Therefore,
to emphasize the generality of the discussion the term of
multivalent flaw (defects) could have been used instead
of monovalent donors in the analysis. The equations
formulated for "divalent donors" would have given similar
results for the ionization energies.

4.3.5. Summary

Donor behaviour of the implanted oxygen ions
in silicon was observed on samples implanted at 300° K
temperature with 80/40 keV energy ion beams. The total
dose was increased from 1.4×10^{14} ions/cm^2 up to
5.6×10^{14} ions/cm^2 in equal steps implanting four
samples. (Fig. 4-24).
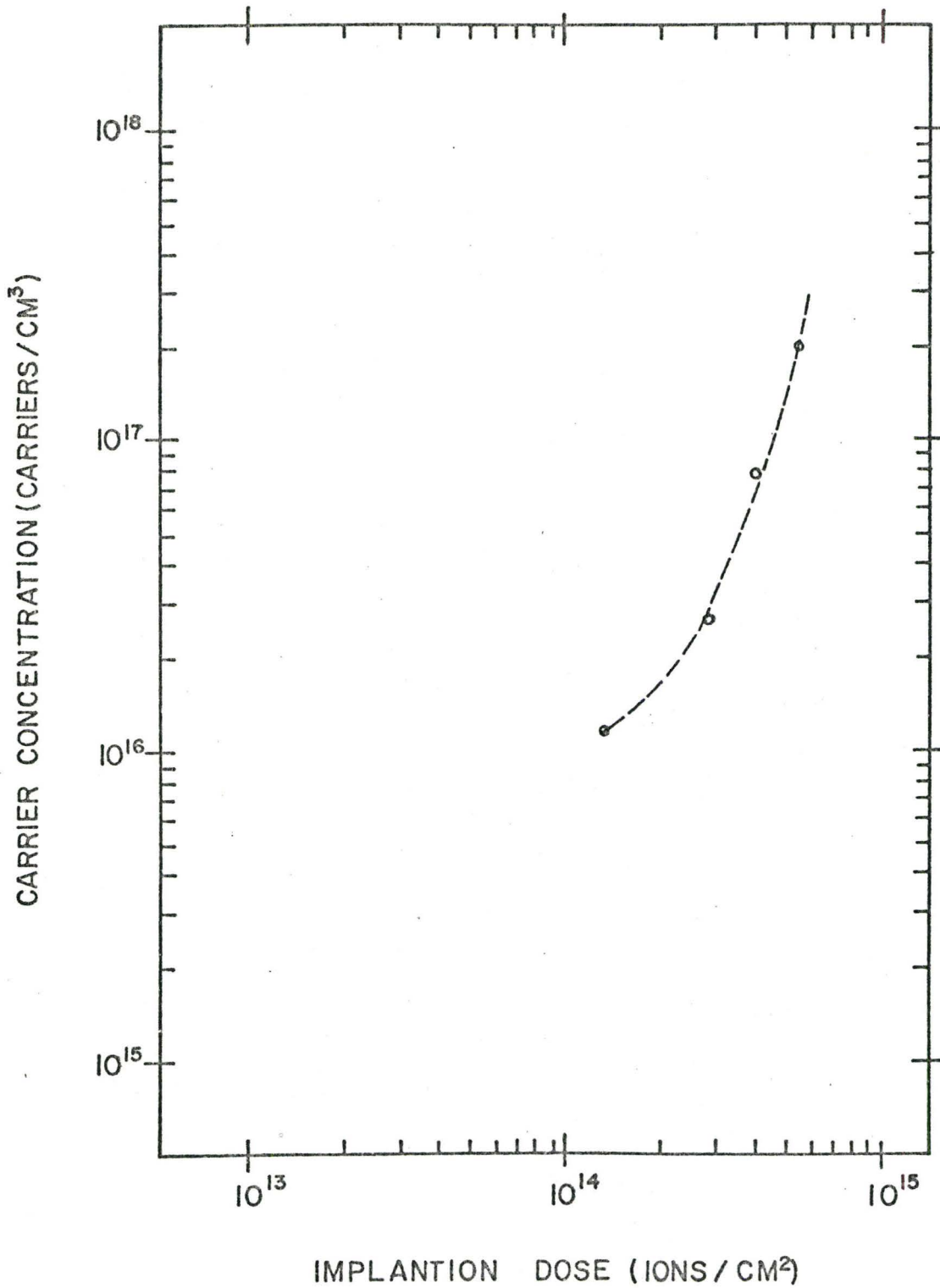
Figure (4 - 24). The number of carriers produced in oxygen
implanted silicon as a function of implan-
tation dose.

The reproducibility of the implantations was demonstrated on samples implanted and annealed under the same conditions. The conversion efficiency of the oxygen implantation was very low. Only 0.5% of the total number of implanted oxygen ions became active after anneal.

As it was in the nitrogen implantation study, a partially compensated n-type semiconductor model having two independent types of donors could be used to describe the electrical characteristics of the oxygen implanted layers. $E_{d1} = 0.021 \pm 0.001$ eV and $E_{d2} = 0.037 \pm 0.001$ eV activation energies were determined for the two donor levels. These ionization energies are not significantly different from the 0.03 eV value which is the generally accepted donor level for oxygen in silicon.

The conditions in the implanted layer approached degenerate when the total dose was increased to 5.6×10^{14} ions/ cm^2 in one sample (Si - 9). The electrical characteristics of this sample were similar to a very highly doped n-type semiconductor.

The ionization energy values were found to be significantly smaller in the heavily doped samples (i.e. Si-8, Si-9) compared to the values obtained for moderately doped samples. By increasing the temperature and/or the time of the anneal a considerable decrease
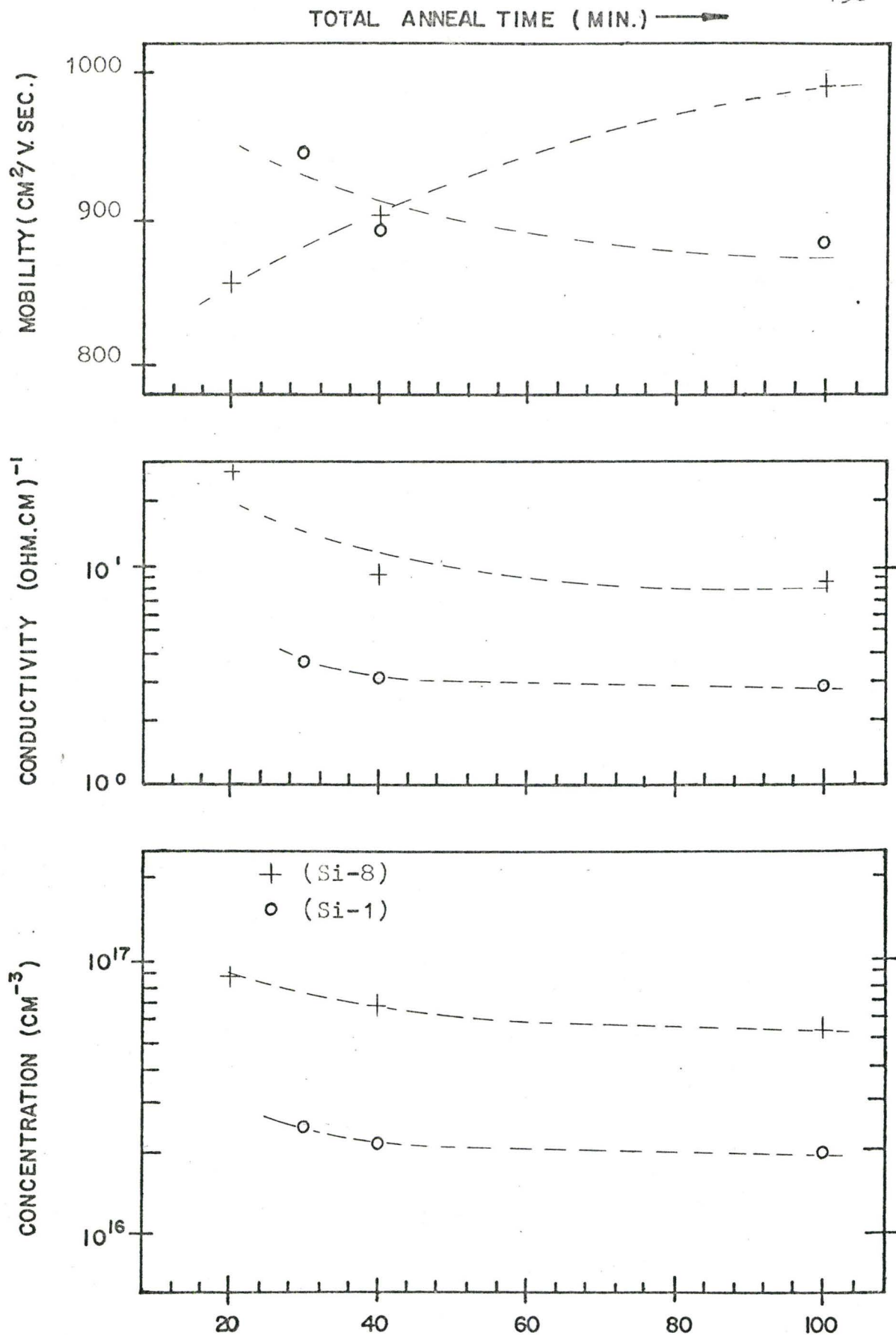
Figure (4 - 25). The effect of annealing time on the fundamen-
tal electrical parameters of oxygen ion
implanted silicon samples.
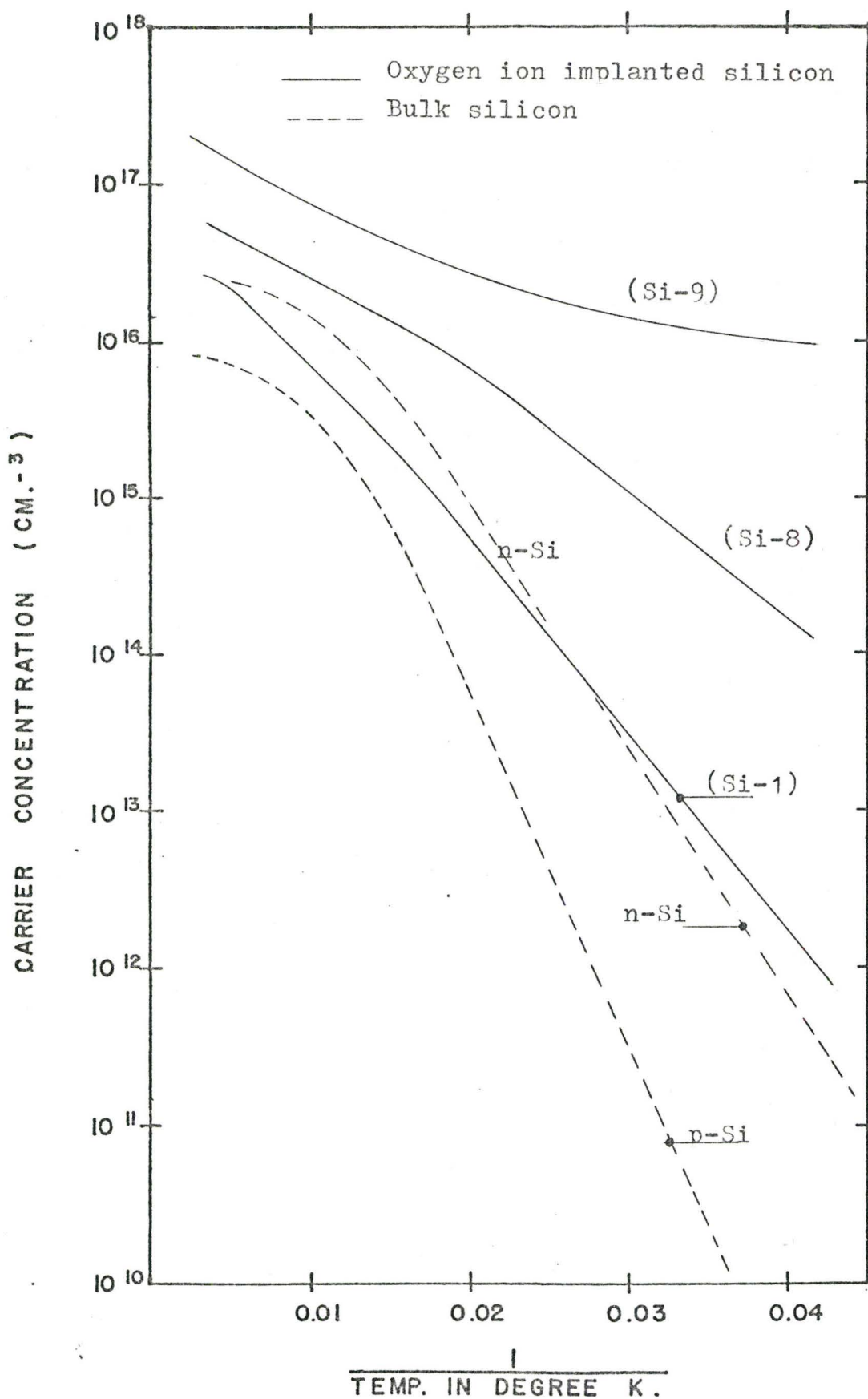
Figure (4 -26). Comparison between the n vs. (1/T) graphs
of oxygen ion implanted and bulk silicon
samples.

in the carrier concentration , and a slight increase in the activation energies were noticed, which may have been due to oxygen outdiffusion. Figures (4-22) and (4-25) are the corresponding figures showing the effects of various annealing.

The summarized results of the conductivity and Hall effect measurements performed on the series of oxygen implanted silicon samples are shown in Figure (4-26). The results obtained from the experiments carried out on bulk silicon samples are also presented for comparison in the same figure.

V

CONCLUSIONS

5.1. Summary

In this report an investigation of the fundamental electrical properties of nitrogen ion implanted silicon and oxygen ion implanted silicon is presented.

The most important properties of a semiconductor sample can be characterized by the temperature dependence of carrier concentration and mobility and by the number of compensating impurities in the semiconductor. Hall effect and sheet resistivity measurements in wide temperature range are useful tools to evaluate the electrical behaviour of ion implanted layers. In order to establish good electrical isolation between the implanted layer and the substrate, the concentration of active impurities in the implanted layer must be much greater than the dopant concentration of the substrate. The use of high resistivity substrates ensures that the depletion layer does not extend considerably into the thin implanted layer. In these experiments 7.66-13.33 ohm-cm resistivity substrates were used. The application of a 10 ohm-cm substrate is practically sufficiently high to measure 10^{11} carriers/cm^2 in the implanted layer.

161

Bulk boron doped p-type and phosphorus doped n-type silicon samples were measured in the automatic Hall effect measuring equipment to check its calibration accuracy. The ionization energies of the boron and phosphorus impurities were obtained from the analysis of the normalized carrier concentrations vs. 1/T graphs and the results were in good agreement with the generally accepted values.

The electrical properties of nitrogen and oxygen implanted silicon were studied as a function of implantation and anneal conditions. N-type behaviour of the implanted layers was observed in all the cases and it was found that the results of the experiments were reproducible at implantation doses less than 8×10^{14} ions/cm^2. Many similarities were found between the electrical properties of nitrogen and oxygen implanted silicon. The conversion efficiency was very low (less than 1%) in both cases. Both the nitrogen and oxygen implants showed considerable decrease in the concentration of active carriers after high temperature long duration anneal. The effect might have been due to the outdiffusion of implanted ions from the system, however the validity of this assumption should be checked experimentally.

The temperature dependence of the carrier concentration of nitrogen implanted silicon was very similar to oxygen implanted silicon, but it was significantly

different compared with the bulk silicon samples. It was
possible to describe the electrical properties of the
bulk silicon samples with partially compensated semi-
conductor models containing only a single donor or acceptor
level and a compensating impurity level of the opposite
type. However, the tests of using the same model for the
analysis of the results of electrical measurements of
implanted layers have failed. It was assumed that the different
behaviour experienced in the nitrogen and oxygen implanted
layers could be due to the presence of a second deeper
donor energy level. The attempts to approximate theoreti-
cally the carrier concentration vs. 1/T experimental
graphs of the implanted samples were successful with a
partially compensated n-type semiconductor model containing
two independent types of monovalent donors at different
energies. $E_{d1} = 0.016 \pm 0.001$ (eV), $E_{d2} = 0.034 \pm 0.003$ (eV)
activation energies of the donor like impurities of the
nitrogen implanted silicon and $E_{d1} = 0.021 \pm 0.001$ (eV),
$E_{d2} = 0.037 \pm 0.01$ (eV) activation energies of the donor
dopants in the oxygen implanted silicon were obtained
from the analysis. The above energies were found to be
consistent and independent of the implantation and
anneal conditions. In Figure (5-1) the n(1/T)
carrier concentration functions of a typical nitrogen
implanted, oxygen implanted and bulk silicon samples
are plotted. The significant differences among the
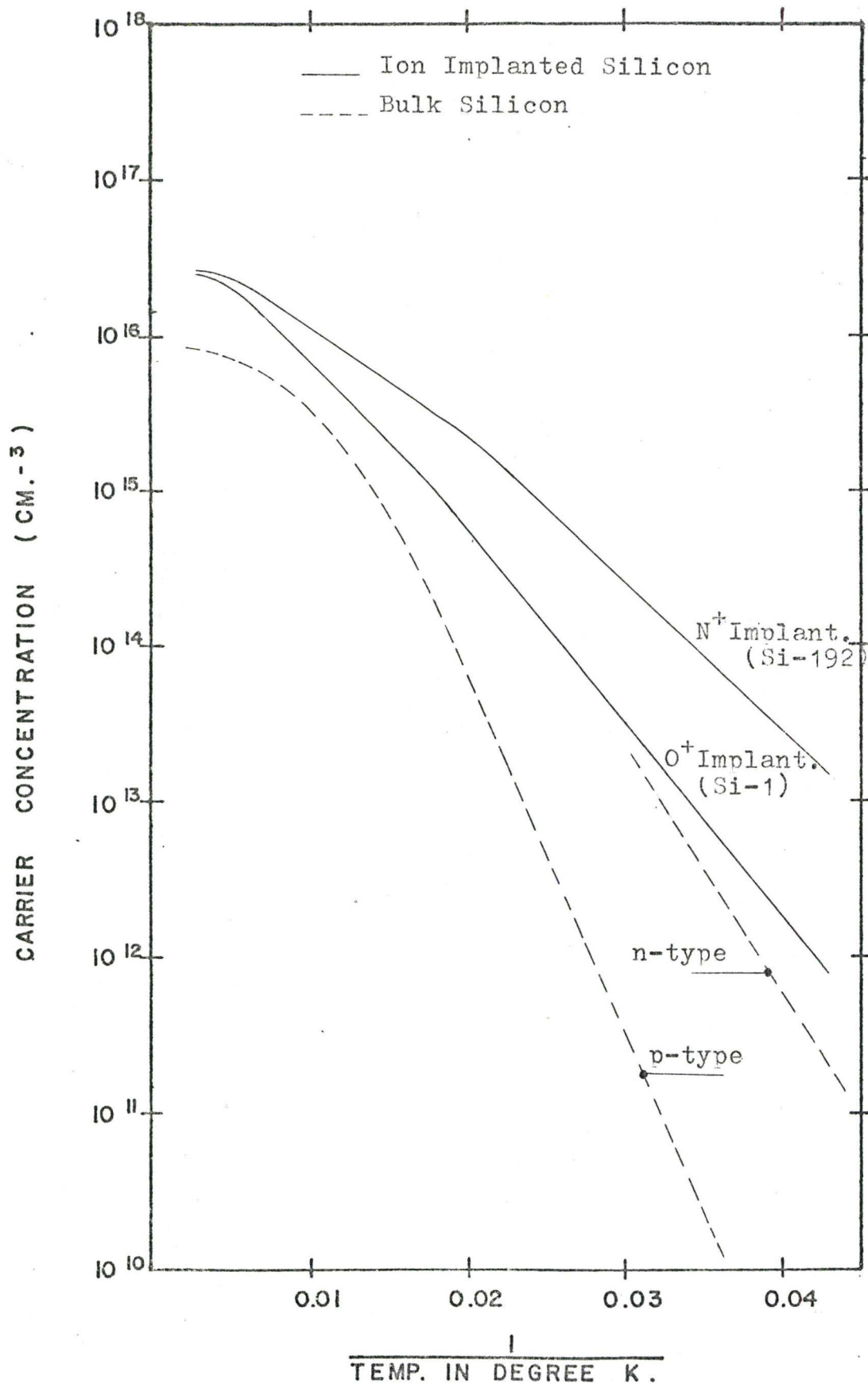
Figure (5 - 1). Carrier concentration vs. (1/T) curves obtained
for typical bulk, nitrogen and oxygen ion implanted
silicon.

ionization energies of the various impurities in silicon are quite visible in this graph.

It should also be noted that the kind of impurity behaviour which was experienced in both the nitrogen and oxygen ion implanted silicon samples is not unique in the properties of doped semiconductor materials. Similar behaviour of the zinc - doped germanium is well known from the experimental data of Tyler and Woodbury [32]. They used a model containing two discrete acceptor ionization levels and a compensating donor level with their corresponding impurity concentrations to describe the multivalent acceptor behaviour of zinc impurities in germanium.

It has been recognized that there are other semiconductor models which could have been used in the analysis of the experimental data of both the nitrogen and oxygen implanted silicon samples. The equations formulated for "divalent donors" as a particular case of a semiconductor model dominated by a set of multivalent defects would give similar results for the electrical parameters of these ion implanted layers. In order to decide which model should be selected for the analysis of the experimental results, one would have to determine what happens to the implanted nitrogen or oxygen in the silicon substrate. In other words, it has to be

determined whether substitutional impurities or multivalent defect centers are responsible for the particular n-type behaviour.

More experiments are suggested, particularly in the study of oxygen ion implanted silicon. The damage study carried out in detail in the case of nitrogen implanted silicon[16] could be extended to the area of oxygen implantations too. Optical absorption techniques could be used for determining the lattice locations of the implanted atoms. The cause of the decreasing donor activities after high temperature, long duration anneal may be found by using optical absorption measurement after each anneal cycle. A detailed analytical treatment of the temperature dependence of the carrier mobility in the implanted layers could also bring some additional results.

APPENDIX

A PROGRAM FOR THE ANALYSIS OF THE HALL EFFECT DATA

A.1. Information Necessary for Calculations

Card #1   Title [Format (13A6)]
Card #2   Width Length Thickness ICHK*
               [Format (3F 10.3, 50A1)]
Card #3   EFMASP, EFMASN, MOBRAT, RMAX, DELTA
               [Format (5E 10.3)]
Card #4   DATA

DATA is entered in nonstandard format from the tape.
*ICHK if plots are desired write PLOT
    if punched cards are desired write PUNCH

A subrutine exists to calculate the scattering parameter
(r) at all temperatures. At present this subroutine assigns
the value $3\pi/8$ to r at all temperatures. If a more complex
dependence is required, a new subroutine must be written by
the user.
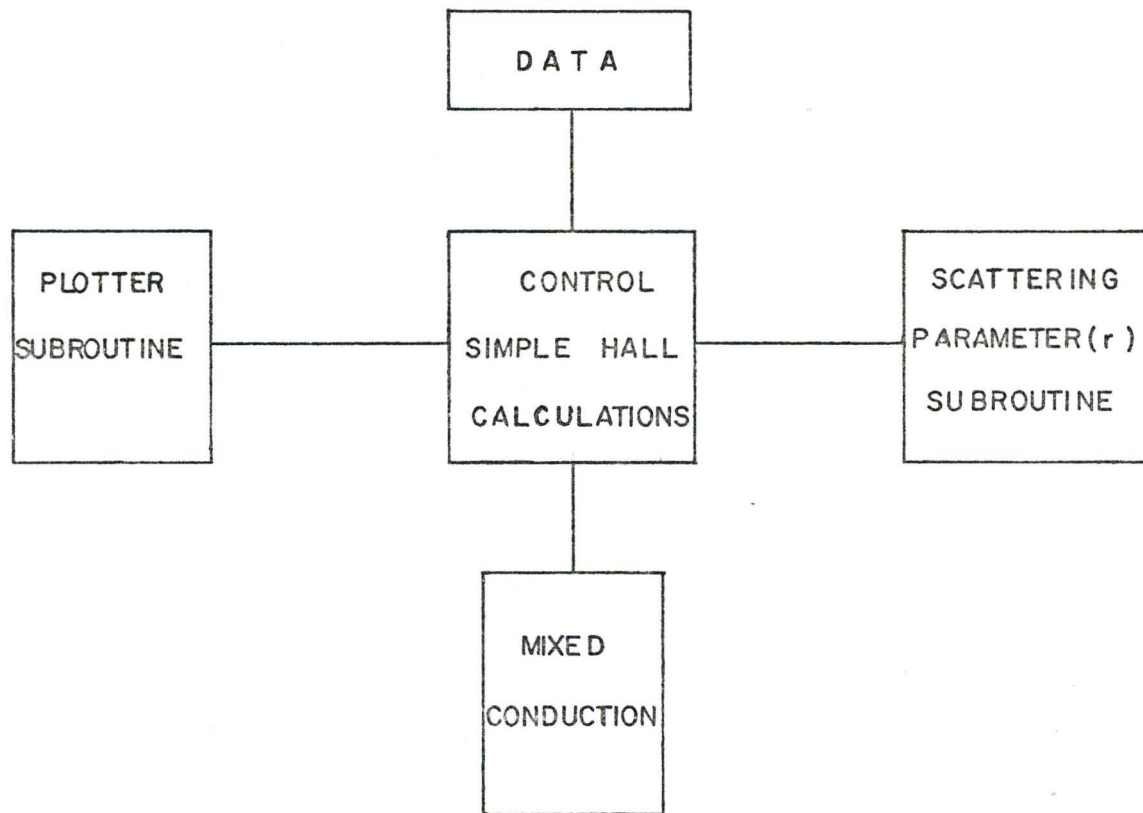
FIGURE (A-I) MASTER BLOCK DIAGRAM

A.2. Programme Parameter Definitions

AAA   array used in LESQ programme

AJIM   used in degeneracy check

ALHI   data point near RECLEE

ALLO   data point near RECLEE

ALNLEE   natural log of absolute value of compensation

ALNN   natural log of absolute value of carrier concentration

ALNX $\ln |N_D - N_A|$

AMOBCN   conductivity mobility of electrons in mixed cond.

AMOBCP   conductivity mobility of holes in mixed conduction

AN   electron concentration in mixed conduction

AP   hole concentration in mixed conduction

APETER   ln of normalized concentration

APNT   same as ALNN

AP1

      parameters defined in Lee's paper

AP3

AT   average temperature

AVC   average conductivity voltage

AVH   average hall voltage

B   magnetic field

BBB(1)

      parameter of LESQ fit for ionization energy

BBB(2)

COMPEN   compensated inpurity density

CONC   concentration

CONCN	same as AN
CONCP	same as AP
COND	conductivity
DELTA	range in $1/T$ where ionization energy is determined
EFMASN	$\dfrac{m_e{}^*}{m_o}$ density of states effective mass
EFMASP	$\dfrac{m_h{}^*}{m_o}$ density of states effective mass
EGO	E_{go}
ENERGY	ionization energy in electron volts
ERLE	used in check in magnetic field
FLIM	ratio of two conductivity voltages
GAMMA	constant in intrinsic concentration
GEOM	(width x length) $\div$ (thickness)
I	current
IEXP	current expressed in exponential form
IVEX	same as VEX in integer form
LENGTH	conductivity length
MASS	either $\dfrac{m_e{}^*}{m_o}$ or $\dfrac{m_p{}^*}{m_o}$
MOBC	conductivity mobility
MOBH	Hall mobility
MOBRAT	$\mu H/\mu C$
MB	mobility
NP	number of data points used in LESQ for ionization energy

OVS	number of data points used in LESQ for determining E_{go}
R	scattering parameter (r)
RECHI	data point near RECLEE
RECIP	$1/T$
RECLEE	$(1/TLEE)$
RECLO	data point near RECLEE
RECMAX	temperature range over which E_A or E_D is determined
RECMIN	
RH	Hall coefficient
RHO	resistivity
RMAX	maximum resistance that the Hall system can handle
RHOMAX	resistivity which corresponds to R_{max}
RRECIP	same as RECIP
SLOPE	slope of ALNN with respect to RECIP
SS	see section on mixed conduction
T	temperature before averaging
THICK	thickness of the sample
TLEE	temperature where LESQ staight line has a value ALNX
TMAX	$1/RECMAX$
TMIN	temperature that corresponds to RMAX
TRANS	array used for LESQ for E_{go}
TUK(1)	parameters of LESQ for E_{go}
TUK(2)	

VC   conductivity voltage

VEX   voltage read proportional to sample current

VGE   germanium thermometer voltage

VH   Hall voltage

WIDTH width of sample

A.3. Program Flow Chart

```
┌─────────────────────────────────┐
│          Read Title             │
└─────────────────────────────────┘
                 │
┌─────────────────────────────────┐
│          Read Width             │
│        Length Thickness         │
│             ICHK                │
└─────────────────────────────────┘
                 │
┌─────────────────────────────────┐
│         Read Material           │
│          Parameter              │
└─────────────────────────────────┘
                 │
┌─────────────────────────────────┐
│          Read Data              │
└─────────────────────────────────┘
                 │
┌─────────────────────────────────┐
│         Check Format            │
│             and                 │
│            Signs                │
└─────────────────────────────────┘
                 │
┌─────────────────────────────────┐
│      Calculate Average          │
│        Temperature              │
└─────────────────────────────────┘
                 │
┌─────────────────────────────────┐     ┌──────────────┐
│         Calculate r             │─────│  Subroutine  │
│      at each Temperature        │     │   supplied   │
└─────────────────────────────────┘     └──────────────┘
                 │
┌─────────────────────────────────┐
│      Calculate Average          │
│     Conductivity voltage        │
│       and Hall voltage          │
└─────────────────────────────────┘
                 │
┌─────────────────────────────────┐
│   Calculate Hall Coefficient    │
│                                 │
│         (avg V_H) thick         │
│   R_H = ─────────────────────   │
│         I x B x 1.0 x 10^8      │
└─────────────────────────────────┘
```

$$R_H = \frac{(\text{avg } V_H) \text{ thick}}{I \times B \times 1.0 \times 10^8}$$

Calculate Resistivity

$$\rho = \frac{\text{average } V_c \times \text{geom}}{I}$$

Calculate Conductivity

$$\sigma = 1/\rho$$

Calculate Hall Mobility

$$\mu_H = |R_H| x$$

Calculate Conductivity

Mobility $\mu_c = \mu_H/r$

Check Magnetic field — if high flagged by * in table

Calculate Carrier Concentration

$$n = \left| \frac{r}{R_H e} \right|$$

Check for Degeneracy — if degenerate flagged by **

Calculate max ρ below which readings are accurate

Find T_{min} corresponding to max ρ and only consider temp. above these

Calculate T_{max}

Least squares fit to determine slope of log n vs. 1/T between T_{min} and T_{max}

```
┌─────────────────────────────┐
│      Ionization Energy       │
│         from slope           │
└─────────────────────────────┘
              │
┌─────────────────────────────┐      ┌──────────────────┐
│      Check for Mixed         │──────│ flag go to mixed │
│        Conduction            │      │   conduction     │
└─────────────────────────────┘      └──────────────────┘
              │
┌─────────────────────────────┐
│        find  $N_D$-$N_A$     │
└─────────────────────────────┘
              │
┌─────────────────────────────┐
│    evaluate Compensation     │
└─────────────────────────────┘
              │
┌─────────────────────────────┐
│        Write  Title          │
└─────────────────────────────┘
              │
┌─────────────────────────────┐
│     Write out data with      │
│   more than 10% variation    │
│  in conductivity voltages    │
└─────────────────────────────┘
              │
┌─────────────────────────────┐
│     Write out data with      │
│    ambiguity in sign of      │
│        Hall voltages         │
└─────────────────────────────┘
              │
┌─────────────────────────────┐
│        Set data with         │
│      incorrect formats       │
│          to zero             │
└─────────────────────────────┘
              │
┌─────────────────────────────┐
│        Write table of        │
│ T, $\frac{1}{T}$, I, $V_c$, B, $V_H$, $R_H$, r │
│  $\rho$, $\sigma$, $\mu_c$, $\mu_H$, conc,  │
└─────────────────────────────┘
              │
┌─────────────────────────────┐
│        Write  either         │
│  $E_A$, $N_D$, $N_A$, $N_A - N_D$   │
│  $E_D$, $N_A$, $N_D$, $N_D - N_A$   │
└─────────────────────────────┘
              │                       ┌──────────────────┐
              │───────────────────────│ Mixed Conduction │
              │                       └──────────────────┘
┌─────────────────────────────┐
│            Plot              │
│   $\mu_H$; $\mu_c$, $R_H$, $\rho$    │
│    and concentration         │
└─────────────────────────────┘
              │
┌─────────────────────────────┐
│            End               │
└─────────────────────────────┘
```

REFERENCES

1. J. Shewchun, K.M. Ghanekar, R. Yager, H.D. Barber and D.A. Thompson, The Rev. Sci. Instrum. 42, 1797 (1971)

2. W.R. Hardy, Ph. D. Thesis, McMaster University, Nov. 1971.

3. N.G.E. Johansson + and J.W. Mayer, Solid-State Electronics, 13, 317 (1970)

4. Marshall, Samuel Luis, Microelectronic Technology, Boston Tech. Publishers Inc. 1967.

5. L. Holland, Thin Film Microelectronics, J. Wiley & Sons Inc. 1965.

6. S.K. Gandhi, The Theory and Practice of Microelectronics, J. Wiley & Sons Inc. 1968.

7. W.A. Pliskin, and R.P. Gnall, J. Electrochem. Soc. 111, 872 (1964)

8. "Techniques for Photolitography" Eastman Kodak Co., Rochester, New York, 1966.

9. B.E. Deal and S.A. Grove, J. Appl. Phys. 36,(12), 3370 (1968)

10. B.E. Deal, J. Electrochem. Soc. 110 (6), 527 (1963)

11. P.A. Lee, British Journal of Applied Physics, 8, 340 (1957)

12. J.S. Blakemore, Semiconductor Statistics, Pergamon Press, 1962.

13. F.J. Morin and J.P. Maita, Phys. Rev. 96, 28 (1954).

14. H.F. Wolf, Semiconductors, John Wiley & Sons Inc. 1971.

15. H.F. Wolf, Silicon Semiconductor Data, Pergamon Press, 1969.

16. J.B. Mitchell, Ph. D. Thesis, McMaster University, Hamilton, Sept. 1973.

17. W. Kaiser, H.L. Frisch and H. Reiss, Phys. Rev., 112, 1546 (1958).

18. H.J. Stein, Wendland Breezhold, Appl. Phys., Letters 17, 442 (1970)

19. H.J. Hrostowski and R.H. Kaiser, Phys. Rev. 107, 966 (1957), H.J. Hrowstowski and B.J. Adler, J. Chem. Phys, 33, 980 (1960).

20. J.W. Corbett, G.D. Watkins, R.M. Chrenko and R.S. McDonald, Phys. Rev. 121, 1015, (1961).

21. E.H. Putley, Hall effect and Related Phenomena (Butterworth's, London, 1960).

22. R.H.A Carter, D.J. Howarth and E.H. Putley, J. Sci. Instr. 35, 115 (1958). E.H. Putley, ibid. 33, 164 (1965).

23. S.M. Sze, Physics at Semiconductor Devices, J. Wiley and Sons, New York (1969).

24. A.S. Grove, Physics and Technology of Semiconductor Devices, J. Wiley, New York, 1967.

25. O. Meyer, IEEE. Trans. Nucl. Sci. NS-15 (3), 232, (1968)

26. J.W. Mayer, L. Eriksson and J.A. Davies, Ion Implantation in Semiconductors, Academic Press, New York, (1970).

27. R.R. Haberecht, E.L. Kern, Semicond. Silicon, The Electrochem. Soc. Inc., New York, p. 433 (1969).

28. E.M. Conwell, Phys. Rev. 99, 1195 (1955)

29. R.D. Pashley, Radiation Effects, (1971) Vol. II, pp. 1-8.

30. C.M. Hurd, The Hall effect in metals and alloys, Plenum Press, New York - London (1972).

31. J.F. Gibbons, Semiconductor Electronics,
    McGraw Hill, New York, 1967

32. Tyler, Woodbury, Phys. Rev. 102, 647 (1956)

33. J. Lyndhard, M. Scharff and H.E. Shiott, Kgl. Danske
    Videnskab. Selskab. Mat. Fys. Medd. 33, No.14 (1963)

34. J. Lindhard and M. Scharff, Phys. Rev. 124, 128, 1961.

35. J. Lindhard, Kgl Danske Videnskab. Selskab. Mat. Fys.
    Medd. 34, No.14 (1963)

36. N. Large and R.W. Bicknell, J. Mater. Sci. 2, 589(1967)

37. J.O. McCaldin, Prg. Solid State Chem. 2, 9 (1965)

38. J.F. Gibbons, Proc. IEEE 56, 295 (1968)

39. W.S. Johnson, W.J. Kleinfelder, and J.F. Gibbons,
    Record of the IEEE Ninth Annual Symposium on Electron,
    Ion, and Laser Beam Technology, 1967.

40. W. Shockley and J.T. Last, Phys. Rev. 107, 392 (1957)

41. P.T. Landsberg, proc. Phys. Soc. London, B69, 1056
    (1957)

42. P.T. Landsberg, Solid State Theory, Wiley-Interscience
    (1969)

43. C.H. Champness, Proc. Phys. Soc. London, B69, 1335
    (1956)

44. J.W. Corbett and G.D. Watkins, Radiation Effects in
    Semiconductors, Gordon and Breach Science Publishers,
    London, New York, Paris (1971)

45. W. Kaiser, P.H.Keck, and Lange, Phys. Rev. 101, 1264 (1956)

46. H,J. Hrostowski and R.H. Kaiser, Bull. Am. Phys. Soc.
    Ser. II, 1, 294 (1956)

47. Fuller, Dietzenberger, Hannay and Buehler, Phys. Rev.
    96, 883 (1954)

48. W. Kaiser and P.H. Keck, J. Appl. Phys. 28, 882 (1957)

49. J.W. Corbett, G.D. Watkins, R.M. Chrenko, and
    R.S. McDonald, Phys. Rev. 121, 1015 (1961)

50. L.J. Cheng, J.C.Corelli, J.W. Corbett, and G.D. Watkins, Phys. Rev. <u>152</u>, 761 (1966)

51. L.J. Cheng and J. Lori, Phys. Rev. <u>171</u>, 856 (1968)

52. R.E. Whan, J. Appl. Phys. <u>37</u>, 3378 (1966)

53. H.J. Stein, F.L. Vook, and J.A. Borders, Appl. Phys. Lett. <u>14</u>, 328 (1969)

54. H.J. Stein and Wendland Beezhold, Appl. Phys. Lett. <u>17</u>, 442 (1970)

55. S.M. Sze and J.C. Irwin, Solid-State Electronics, <u>11</u>, 599 (1968)

56. W. Fahrner and A. Goetzberger, Appl. Phys. Lett. <u>21</u>, 329 (1972)